Photon diffractive scattering off proton at high t with the H1 detector

Université Libre De Bruxelles
Faculté des Sciences

Academic year 2003-2004

Tomáš HREUS

Abstract

The diffractive photon scattering at high t is studied using the H1 detector at HERA in the photoproduction regime ($Q^2 \sim 0$). The process $\gamma p \longrightarrow \gamma Y$ has the final photon of large transverse momentum implying the presence of the hard scale t, allowing predictions of the perturbative QCD to be applied. The measurement is based on 36.9 pb^{-1} of data collected in the 1999–2000 running period. The cross–section is measured differentially in the squared four momentum transfer t and in $x_{I\!P}$ in the kinematic domain $y_{I\!P} < 0.018,\ 0.0001 < x_{I\!P} < 0.0007,\ 175 < W < 247$ GeV, $|t| > 4$ GeV^2. Results are compared to the perturbative QCD model prediction of LLA BFKL and the recent preliminary results of the H1 Collaboration.

Contents

Chapter 1

Introduction

The Standard Model is a very successful theory to describe a wide spectrum of phenomena in particle physics. As a conjunction of two well tested theories – the Quantum Chromodynamics and the electroweak theory, the Standard Model includes all three forces that play a dominant role in the high energy physics. The elecroweak theory introduced by Glashow, Weinberg and Salam is the unified theory of the electromagnetic and weak interaction and is based on SU(2)×U(1) group. The Quantum Chromodynamics based on the SU(3) group is a quantum field theory of the strong interaction successfully describing the hadron reactions on the basis of quarks and gluons. The parton structure was proved by early experiments observing the so–called scaling invariance of the proton structure function $F_2(x, Q^2)$. The renormalization procedure leads to the running meaning of the strong coupling constant which is small only at small distances and the perturbative approach of QCD calculations can be applied. The lowest boundary of the energy region of this perturbative applicability is set by the normalization parameter Λ^2_{QCD}.

Diffractive phenomena studied in hadron–hadron interactions in the 60'–70' find an equivalent in the photon–proton interactions at HERA. Thanks to the possible presence of a hard scale, large Q^2, large masses or large transverse momentum, HERA offers the opportunity to study the diffraction in terms of a fundamental theory, QCD.

In this thesis, the diffractive process $\gamma p \longrightarrow \gamma Y$ is considered, where the final photon of high transverse momentum p_T is separated from the dissociative Y system by the rapidity gap. The hard scale is present by the four momentum transfer at the proton vertex $-t \gg \Lambda^2_{QCD}$ that propagates from the proton side resulting into high transverse momentum of the final photon $(p^\gamma_T)^2 = -t$, whereas the $Q^2 \ll \Lambda^2_{QCD}$. Unlike in the diffractive vector meson production, where the products of the vector meson subsequent decay give additional multiplicity to be detected, the considered process consists of the single photon leading to enlargement of the spatial acceptance. The advantages to the

experimental observation is also the large and clean rapidity gap since the subsequent strong interaction between the proton dissociative system and the final real photon is suppressed and together with the clear signature of the process, the diffractive photoproduction of photon at large t allows precise measurement of the cross–section and comparison to the theoretical prediction of BFKL approach of the perturbative QCD.

This particular process has been measured for the first time by H1 and preliminary results were shown in summer 2003 at the HEP conference [2]. The work presented in this thesis reports an independent measurement of its cross–section and a comparison to the H1 preliminary results.

Chapter 2

The Theoretical Basis

This chapter presents the basics of the deep inelastic scattering and diffraction. The kinematic variables are defined and the parametrisation of the proton structure in terms of structure functions is introduced. Furthermore the dynamical aspects are presented in the two assymptotical approaches DGLAP and BFKL. Finally the case of diffraction is discussed with a particular insight on exclusive reactions leading to the process studied in this thesis, i.e. the photon diffraction off proton at large t.

2.1 Deep Inelastic Scattering

The *deep inelastic scattering* (DIS) can be written in the general way as

$$l(k) + \mathrm{p}(p) \longrightarrow l'(k') + X(p'), \tag{2.1}$$

where k, p and k' represent the 4–momentum of the incoming lepton, proton and the scattered lepton, respectively, as seen at Fig. 2.1. X represents the final hadronic state particles. In the electroweak theory, such a reaction proceeds via the exchange of a photon or one of the intermediate bosons between the electron line and a the proton line. The DIS can be recognized as

- **Neutral current processes** (NC), corresponding to photon or Z^0 gauge boson exchange,
- **Charged current processes** (CC), corresponding to a $W^{\pm}$ gauge boson exchange; in this case the final lepton is a neutrino.

They differ by the charge conversion between the initial and scattered lepton, but the kinematics is rather similar.

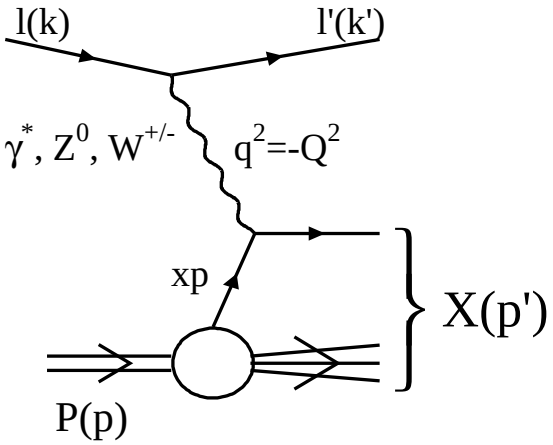

Figure 2.1: The deep inelastic scattering. In the case of charged current DIS, mediated by $W^{\pm}$ boson, $l \neq l'$ but conserves the leptonic quantum number (e.g. $l = e$, $l' = \nu_e$). In the case of neutral current (γ and Z^0 exchange) $l = l'$.

Due to the role of the exchange boson mass in the propagator term[1], the total cross–section is largely dominated by the photon exchange. In the following, we will only consider the NC case and will concentrate on the γ exchange.

2.1.1 DIS Kinematics

In the inelastic scattering, two independent relativistic invariants raise in the description of the reaction kinematics [4, 5]. They could be chosen out of these:

- The *negative 4–momentum transfer Q^2 of gauge boson* is given by

$$Q^2 = -q^2 \equiv -(k - k')^2, \tag{2.2}$$

  where q is the 4–momentum transfer of the intermediate boson. If the photon is almost real ($Q^2 \simeq 0$), the process is referred as *photoproduction* (see section 2.1.5). The values of $Q^2 \gtrsim 4$ GeV^2 correspond to the regime of DIS. The Q^2 is also called the *virtuality* of the boson and in the photoproduction where $Q^2 \to 0$, this boson is real.

- The dimensionless *Bjorken scale variable x*

$$x \equiv \frac{-q^2}{2p \cdot q}. \tag{2.3}$$

[1] the propagator term of the single boson exchange is $\frac{1}{(q^2+m^2)}$, where m is the mass of the boson and q is the momentum transfer

In the Quark Parton Model (section 2.1.2) where the particle rest masses are neglected, the Bjorken x represents the 4–momentum fraction of the proton carried by the struck parton.

- The dimensionless *inelasticity* y defined as

$$y \equiv \frac{p \cdot q}{p \cdot k}. \tag{2.4}$$

The inelasticity corresponds to the energy fraction of the incident electron carried by the exchanged boson in the proton rest frame transferred to the hadronic final state (the system labeled X at Fig. 2.1). Both x and y are defined in the range $0 < x, y \leq 1$.

- The *electron–proton centre–of–mass* (CMS) *energy squared* s is given by the equation

$$s \equiv (k + p)^2 \simeq 4E_p E_e, \tag{2.5}$$

where E_p and E_e is the colliding energy of the proton and the electron, respectively. Still neglecting the electron and proton masses, the four variables above (2.2, 2.3, 2.4, 2.5) are connected by the relation

$$Q^2 = xys. \tag{2.6}$$

The CMS *energy* W *of the exchanged boson and the incoming proton* is given by

$$W^2 \equiv (q + p)^2 = \frac{Q^2(1 - x)}{x}\ , \tag{2.7}$$

which corresponds to $W^2 = ys - Q^2$ neglecting the proton mass.

A Probe to Proton

The momentum transfer Q^2 can be interpreted as the resolution power and used as a probe to reveal the structure of a particle.

The linear size d is bound by the *De Broglie* wave length $\lambda = \hbar c/Q$ with $\lambda \leq d$, telling that the wavelength must be smaller or equal to the linear size to be revealed. The size d then becomes smaller for large boson virtuality Q as

$$d \sim \frac{\hbar c}{Q} \simeq 0.2 \frac{\text{GeV } fm}{Q}. \tag{2.8}$$

For example, $Q^2 = 4$ GeV^2 leads to the distance of $d \simeq 10^{-14}$ cm, while $Q^2 = 40.000$ GeV^2 increases the resolution to $d \simeq 10^{-16}$ cm. The schematic sketch is depicted at Fig. 2.2.

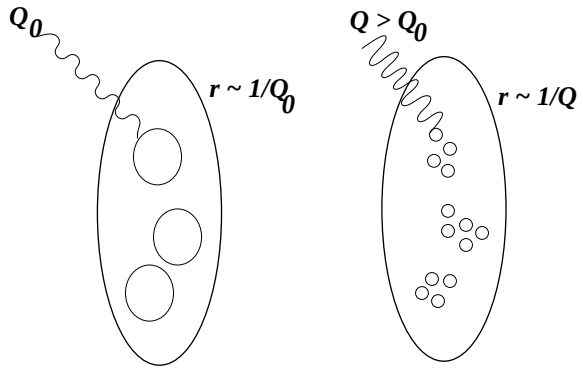

Figure 2.2: Imaginary view of photon probing the proton. Two different virtualities of the photon Q_0 and $Q > Q_0$ deliver different resolution. For a higher virtuality the smaller structure reveals – a quark appearing as pointlike at Q_0 may appear to have radiated gluons at higher Q.

2.1.2 Structure of the Proton

In the *Thompson model*, the proton is a particle consisting of a continuous charge distribution. As for large Q^2, the photon probes smaller distances, being sensitive to the smaller fractions of the electric charge of proton, the dimensionless proton structure function $F_2(x, Q^2)$ is expected to fall by increasing the values of Q^2 for all x.

The Quark Parton Model

However, the SLAC-MIT Collaboration in the late '60s performing the deep[2] inelastic cross–section measurements, observed that $F_2(x, Q^2)$ structure function shows only a little Q^2–dependence (Fig. 2.3) and is dependent on x. This behaviour was named the *scaling invariance* and suggested the existence of the scattering centers within the proton[3]. Based on such observations, Feynman and Bjorken proposed idea that the proton structure consists of so–called *partons*, a pointlike particles carrying the fractions of charge in the proton. Within this *Quark Parton Model* (QPM), a proton consists out of three such partons identified later as the valence quarks, which are 1/2 spin fermions.

The QPM approximation is based on the choice of a specific coordinate frame. This frame holds very high longitudinal momenta of the proton (so-called *infinite momentum frame*), while the transverse momenta and the rest masses of the proton components are neglected. The proton is then almost flat due to Lorentz contraction and the interaction

[2] *deep* means that $Q^2 \gg M_p^2$ and $p \cdot q \gg M_p^2$ [4]

[3] the existence of the proton's substructure was known since 1930s from the measurements of the anomalous magnetic moment of the proton

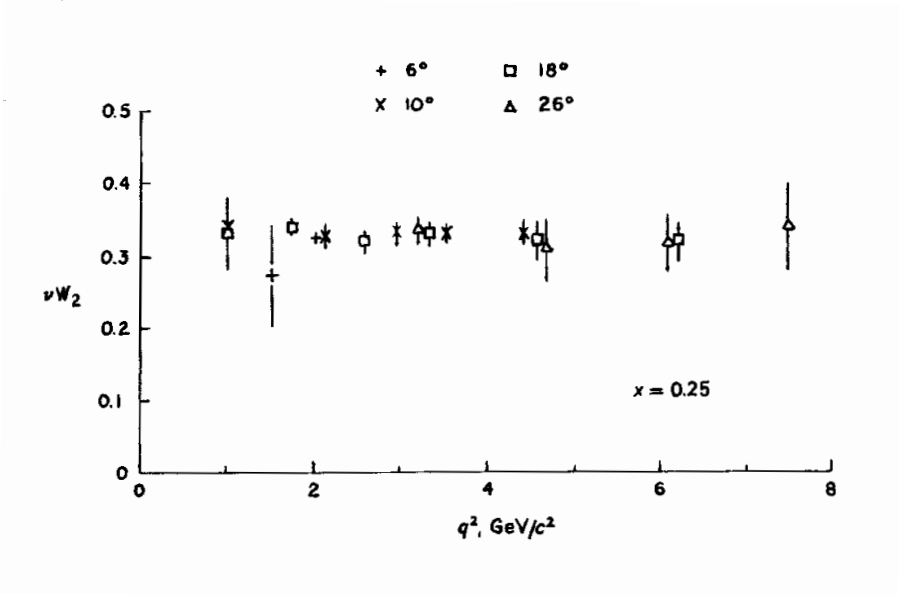

Figure 2.3: Scaling observation of the structure function $F_2(x, Q^2) = \nu W_2(x, Q^2)$ by the SLAC-MIT Collaboration in 1969. The Bjorken x is kept at $x = 0.25$.

time is very small due to time dilatation. Holding this approximation, the quarks of the proton are far from each–other and have no time to interact between themselves. Thus, at large Q^2, quarks interact with the photon as free particles inside the hadron.

The DIS Cross–section

For a NC lepton–nucleon scattering the DIS cross–section is given in the terms of structure functions F_2, F_L and F_3 by

$$\frac{\mathrm{d}^2\sigma^{\pm}_{ep\to eX}}{\mathrm{d}x\mathrm{d}Q^2} = \frac{4\pi\alpha^2_{em}}{xQ^4}\left[\left(1-y+\frac{y^2}{2[1+R]}\right)F_2(x,Q^2) - \frac{y^2}{2}F_L(x,Q^2) \mp \left(y-\frac{y^2}{2}\right)F_3(x,Q^2)\right] \tag{2.9}$$

where α_{em} is the QED coupling constant and $R(x, Q^2)$ is the ratio of cross–sections for the absorption of transversely and longitudinally polarized virtual photons [14]

$$R(x,Q^2) \equiv \frac{F_L(x,Q^2)}{F_2(x,Q^2) - F_L(x,Q^2)} = \frac{\sigma_L(x,Q^2)}{\sigma_T(x,Q^2)}. \tag{2.10}$$

For the Q^2 values below the Z^0 scale ($Q^2 < M^2_{Z^0}$), the parity violating effects related to F_3 are negligible [14] and the process is dominated by γ^* exchange. The longitudinal structure function F_L is defined by the F_1 and F_2 structure functions as

$$F_L(x,Q^2) = F_2(x,Q^2)\left(1+\frac{4M_p^2x^2}{Q^2}\right) - 2xF_1(x,Q^2). \tag{2.11}$$

In the naive Quark Parton Model ($M_p = 0,\ Q^2 \longrightarrow \infty$) *Callan–Gross* relation

$$2xF_1(x) = F_2(x) \tag{2.12}$$

implies that $F_L(x, Q^2) = 0$. Thus for this limit, the longitudinal cross–section $\sigma_L$vanishes and the $R(x, Q^2)$ is obviously zero either. Finally, in the QPM model the NC lepton–nucleon scattering cross–section holds for

$$\frac{\mathrm{d}^2\sigma_{ep\to eX}}{\mathrm{d}x\mathrm{d}Q^2} = \frac{4\pi\alpha_{em}^2}{xQ^4}\left(1 - y + \frac{y^2}{2}\right)F_2(x, Q^2). \tag{2.13}$$

Considering the infinite momentum frame, where the transverse momenta of quarks and their rest masses are neglected, the inelastic *ep* scattering can be described by the electron that scatters elastically off one of the quasi–free partons forming the proton. The deep inelastic scattering cross–section $\sigma_{ep\to eX}$ is then given by the parton momentum distribution function with the elastic electron–parton cross–sections $\sigma_{eq_i\to eq_i}$ (calculable in QED) weighted by the electric charge e_i of the parton and summed over all charged parton flavours i:

$$\frac{\mathrm{d}^2\sigma_{ep\to eX}}{\mathrm{d}x\mathrm{d}Q^2} = \sum_i \int \mathrm{d}x\ e_i^2 f_i(x)\Big(\frac{\mathrm{d}^2\sigma_{eq_i\to eq_i}}{\mathrm{d}x\mathrm{d}Q^2}\Big), \tag{2.14}$$

where the parton distribution (or density) function $f_i(x)\mathrm{d}x = [q_i(x) + \overline{q}_i(x)]\mathrm{d}x$ is interpreted as the probability to find a quark of the flavour i with the momentum fraction in the interval $[x, x + \mathrm{d}x]$ in the proton. The structure function $F_2(x, Q^2)$ is then expressed as

$$F_2(x, Q^2) \longrightarrow F_2(x) = \sum_i e_i^2 x[q(x) + \overline{q}(x)], \tag{2.15}$$

where the $q(x)$ and $\overline{q}(x)$ are the quark and antiquark distribution functions, respectively. The F_2 is thus independent of Q^2 and related to the parton distribution functions of the proton. According to the Callan–Gross relation (2.12), the proton's structure function $F_1(x, Q^2)$ holds for

$$F_1(x) = \frac{1}{2}\sum_i e_i^2[q(x) + \overline{q}(x)]. \tag{2.16}$$

If the $q\overline{q}$ pairs were the only constituents of the proton, their momentum sum over the whole kinematic range of x should satisfy unity

$$\int_0^1 \mathrm{d}x \sum_i x f_i(x) = 1. \tag{2.17}$$

However, measurements show that the distribution integration turns to be $\simeq 0.5$ — and interpreted as the missing momentum is carried by the gluons.

2.1.3 The Quantum Chromodynamics

According to the success of the electro–weak theory of the Standard Model in describing the electroweak interactions at high energies, the 'similar' quantum field theory seemed to be the right to describe the strong interactions as well. The QCD theory is based on the gauge group $SU_C(3)$ and each quark flavour corresponds to a color triplet in the fundamental representation of $SU(3)$.

Within QCD, the proton is built up by the quarks, the 1/2 spin fermions bound together by strong interaction via gluon exchange (the 1 spin bosons). The charge of the strong interaction is represented by the *colour*, a quantum number corresponding to a new degree of freedom, similar to the electric charge in QED, but in contrast, the colour charge has three possible values (e.g. *r*ed, *g*reen, *b*lue) resulting to six types of charge, compared to two in QED. This colour or anticolour is carrying by both, the quarks and the gluons, in contrast to the QED and the chargeless photons. The massless gauge bosons of the theory are the eight bi–coloured gluons

$$r\overline{b},\ r\overline{g},\ b\overline{g},\ b\overline{r},\ g\overline{r},\ g\overline{b},\ \frac{1}{\sqrt{2}}(r\overline{r}-b\overline{b}),\ \frac{1}{\sqrt{6}}(r\overline{r}+b\overline{b}-2g\overline{g}). \tag{2.18}$$

With three colours and three anticolours, 9 combinations of gluons are expected, however, one of them is a colour singlet $\frac{1}{\sqrt{3}}(r\overline{r}+b\overline{b}+g\overline{g})$ carrying no net colour and is to be excluded. Gluons being coloured, they interact with quarks as well as with themselves (*gluon self–coupling*).

With more precise structure function measurements, *scaling violations* were observed, showing again dependence of F_2 with Q^2 within the x values different of those accessed by the first SLAC results. Fig. 2.4 shows the $F_2(x, Q^2)$ measurement in a large (x, Q^2) phase space covered by the experiments so far, showing the dependence on the resolution power of the photon probe. The scaling violation can be explained within the Quantum Chromodynamics (QCD) as quarks inside the proton radiating gluons, which themselves may split into the $q\overline{q}$ pairs.

The Strong Coupling Constant

In the calculation of the QCD cross–sections, integrals turn out to be divergent as a consequence of using pointlike objects [4]. These infinities are called *ultraviolet divergencies* and come from the higher orders of the theory, where the fermion loop diagrams (see Fig. 2.5) arise in which the momenta of the fermions in the loops are no more fixed by the energy conservation[4]. To avoid these infinities, a scheme called the *regularization* is used, leaving the computed cross–sections depending on the energy scale

[4]the Heisenberg's uncertainty relation $\Delta E \cdot \Delta t \geq \hbar$ allows to break the energy conservation within the time scale of Δt

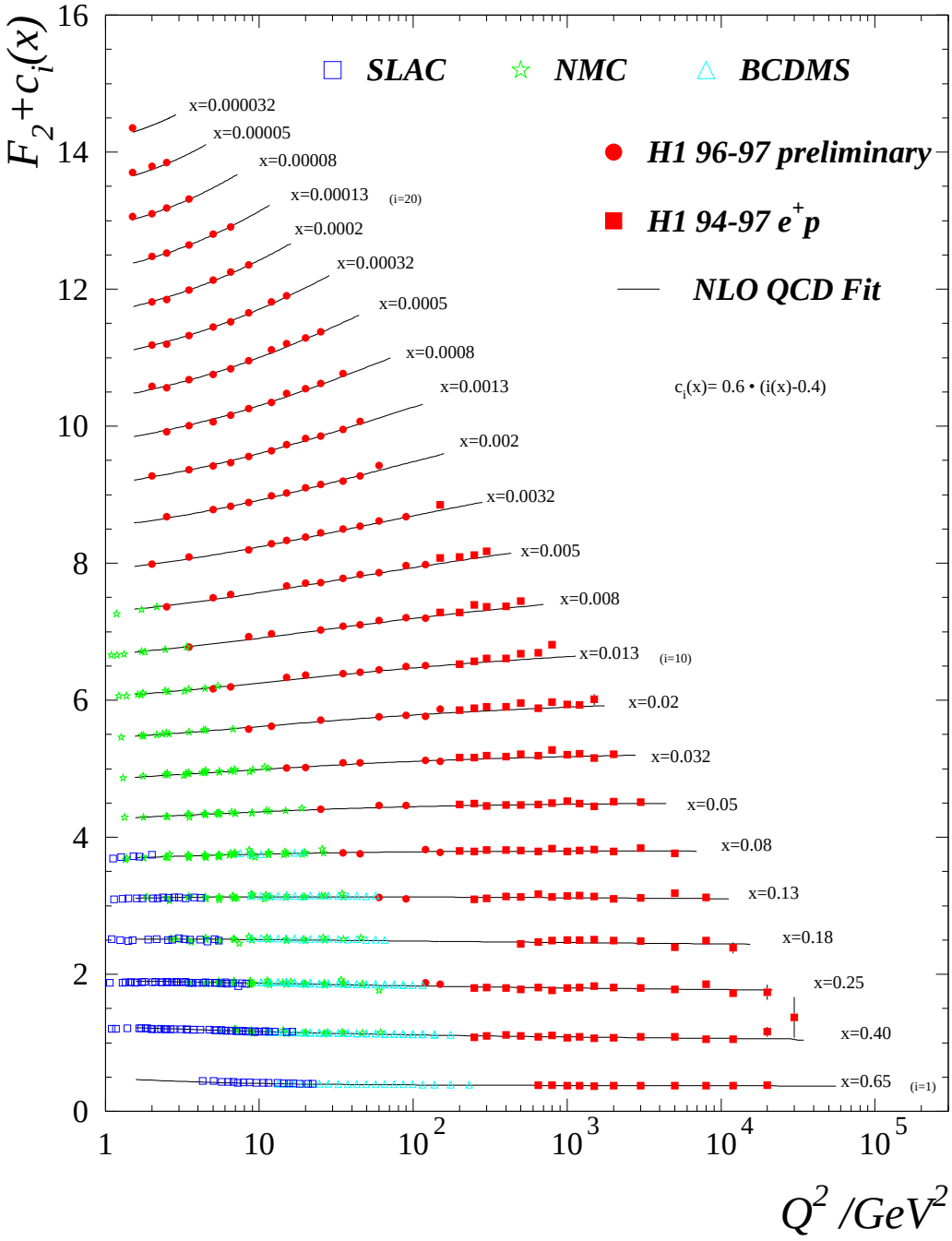

Figure 2.4: Several experiments show data on the proton structure function $F_2(x, Q^2)$, shown here as a function of Q^2 for different values of x. For display purposes, a factor $c_i(x) = 0.6[i(x) - 0.4]$ is added to all F_2 values, where $i(x)$ is the integer bin number in x. This plot gives a good idea of the phase space accessed by the SLAC experiment in which the F_2 exhibits almost no Q^2–dependence, compared to later measurements, mainly at very low x.

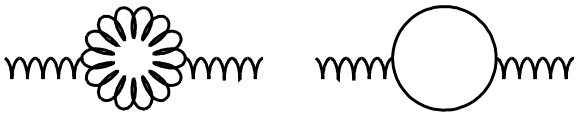

Figure 2.5: Feynman diagrams showing the loops responsible for the ultraviolet divergencies in calculations of QCD cross–sections.

μ_r. This dependence appears in the definition of an *effective coupling constant* α_s, thus $\alpha_s = \alpha_s(\mu_r^2)$. As a consequence, the perturbative coefficients of any observable R would depend on μ_r. This process of removing the divergencies is called *renormalization* and the μ_r is the *renormalization scale*.

However, the physical quantities cannot depend on such an arbitrary parameter (that the μ_r in fact is), if calculated to all orders. This is expressed by the *renormalization group equation* (RGE)

$$\mu_r^2 \frac{\mathrm{d}R(\mu_r, \alpha_s)}{\mathrm{d}\mu_r^2} \equiv \mu_r^2 \frac{\partial R}{\partial \mu_r^2} + \mu_r^2 \frac{\partial R}{\partial \alpha_s} \frac{\partial \alpha_s}{\partial \mu_r^2} = 0. \tag{2.19}$$

By the fact that only a few first terms of variables are calculable, the resulting sum depends on the renormalization scale. It can be shown that this effective QCD coupling constant is well approximated[5] [4, 5, 11] by

$$\alpha_s(\mu_r^2, \Lambda_{QCD}) = \frac{12\pi}{(33 - 2N_f)\,\ln(\mu_r^2/\Lambda_{QCD}^2)}, \qquad \mu_r^2 \gg \Lambda_{QCD}, \tag{2.20}$$

where N_f is the number of quark flavours with mass squared $m_q^2 < \mu_r^2$ and Λ_{QCD}^2 is a scale parameter determined by experiments and represents the lowest limit of μ_r for which perturbative QCD calculations are expected to be predictive. Due to the μ_r^2–dependence, the $\alpha_s(\mu_r^2, \Lambda_{QCD}^2)$ is referred to as the *running* coupling constant[6] with the running fashion depicted at Fig. 2.6.

According to the lowest and highest threshold of μ_r^2, the consequences are

- **Assymptotic freedom:** For large μ_r^2, the α_s is small, going to zero logarithmically and quarks can be treated as free particles over the reduced space and cross–sections are possible to calculate within the perturbative QCD. This is in

[5] when calculating up to the order of α_s, $\mathcal{O}(\alpha_s)$

[6] α_s is not truly a constant, the variable describes the strong interaction and its value depends on the amount of energy transferred between the related objects

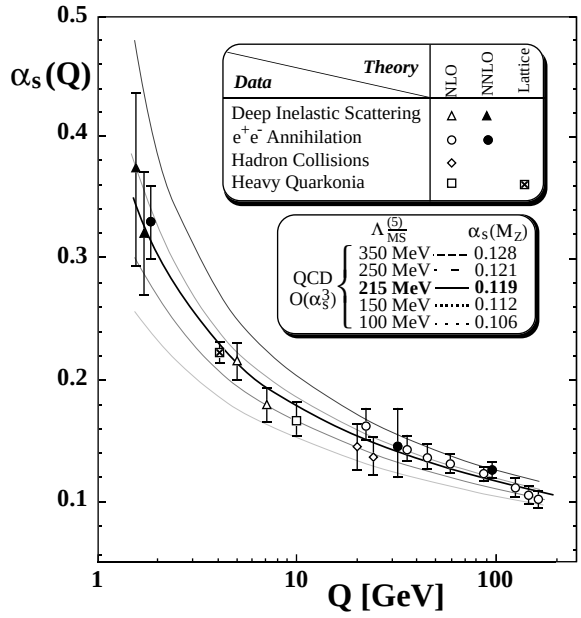

Figure 2.6: QCD running coupling constant α_s as a function of Q.

contrast with the QED, where the α_{em} is larger at high energy[7] due to the *screening* at larger distances, where the loop diagrams lead to vacuum polarization due to virtual e^+e^- pairs, screening the bare e_0 of a particle.

- **Infrared slavery:** At small values of μ_r^2 corresponding to only large distances to be achieved, the coupling constant is large, binding quarks into hadrons; a non–perturbative QCD has to be applied, since the perturbative deviations are too large.

However, for a large μ_r^2 the variation in $\alpha_s(\mu_r^2, \Lambda^2_{QCD})$ is small, thus the 'running' meaning can be neglected.

The Factorization

The theorem of *hard scattering factorization in QCD* states that the short range, perturbatively calculable physical processes, can be separated from the long range processes for which the perturbative theory is not applicable.

[7] $\alpha_{em} = \frac{1}{137}$ at energies ~ 0 and rise at the energy transfer near to the mass M_{Z^0} of the Z^0 boson to the value $\frac{1}{128}$

In QCD, additional infinities connected to the behaviour of strong α_s arise. These so–called *infrared divergencies* arise from a gluon radiation off the quark and are connected to the soft, i.e. long range regime of non–perturbative QCD [6]. They are renormalized in analogy to the ultraviolet divergencies described above, introducing additional *factorization scale* μ_f^2.

According to the factorization theorem, for momentum transfers $Q^2 > \mu_f^2$, α_s is small and perturbative QCD is applicable. This is the short range regime, the high momentum transfer (hard) interactions. The part of the process where $Q^2 < \mu_f^2$ is of the 'soft' origin and is absorbed by the renormalized parton distribution functions $f_i(..., \mu_f^2, ...)$.

As a consequence of this theorem, the proton structure function $F_2(x, Q^2)$ can be divided into the 'hard' and 'soft' region and expressed as

$$F_2(x, Q^2) = \sum_{i=q,\overline{q},g} \int_x^1 \mathrm{d}\xi \; f_i(\xi, \mu_r^2, \mu_f^2, \alpha_s) \cdot C_i^V \Big(\frac{x}{\xi}, \frac{Q^2}{\mu_r^2}, \mu_f^2, \alpha_s \Big). \tag{2.21}$$

The μ_f^2 equals to the energy scale above which additional parton emissions from the quark are included in the perturbative QCD. Long range effects (as the parton emission with $k_T^2 < \mu_f^2$) are absorbed into the parton distribution functions f_i which then become dependent on the factorization scale μ_f^2.[8] The C_i^V are the *coefficient functions* describing the interaction of the exchange boson V with a quark i (see Fig. 2.7), which is calculable in perturbative QCD. In the leading order the $C_g^V = 0$ and since C_i^V coefficients depend on Q^2, they are process dependent, while the f_i distributions depend only on hadron type thus are process independent variables.

2.1.4 Evolution of Parton Distribution Functions

For sufficiently large values of Q^2 (small α_s) it is possible to predict the evolution of the parton distribution functions $f_i(x, Q^2)$, where $\mu_f^2 = Q^2$, using perturbative QCD once the parton distribution is known for a certain starting point $f_i(x, Q_0^2)$. This process is known as the *evolution* and in this perturbative expansion, terms containing powers of

$$\alpha_s \ln(Q^2/Q_0^2), \quad \alpha_s \ln(1/x) \quad \text{and mixed } \alpha_s \ln(Q^2/Q_0^2) \ln(1/x)$$

appear. Two main approximations are made by the DGLAP and BFKL approaches. Both of them need a hard scale to be present.

[8] parton distributions, coefficient functions as well as calculated cross–sections are computed up to a given order in α_s and thus scale dependent

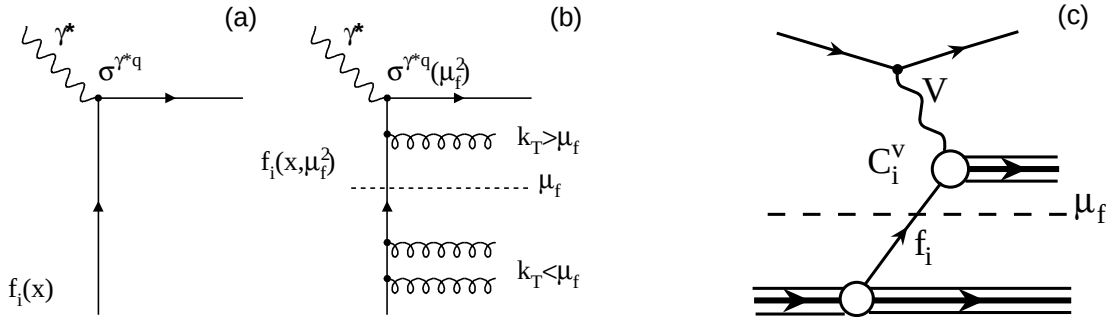

Figure 2.7: Factorization of hard and soft contributions. *(a)* Leading (lowest) order in α_s for the photon–quark scattering and *(b)* next–to–leading (higher) order in α_s. By the redefinition of the quark distribution function f_i all soft gluon emissions with transverse momentum (w.r.t. proton) $k_T < \mu_f$ are absorbed into the quark distribution function. This introduces the μ_f dependence for both, the quark distribution $f_i(x, \mu_f^2)$ and the partonic cross–section $\sigma^{\gamma^* q}(\mu_f^2)$. *(c)* shows the schematical layout of factorization dividing the whole interaction into two parts.

The DGLAP evolution

The DGLAP mechanism done by the Dokshitzer, Gribov, Lipatov, Altarelli and Parisi, predicts the parton distribution functions in dependence of Q^2. However, since it is based on the summation of only the terms of the order of $(\alpha_s \ln Q^2)^n$ and thus neglects the terms proportional of $\alpha_s \ln(1/x)$, it is a good approximation for a high Q^2, but not too small values of x ($x \geq 10^{-2}$). The evolutions of quark and gluon distributions $q_i(x, Q^2)$ and $g(x, Q^2)$ given by the DGLAP equations are:

$$\frac{\partial q_i(x,Q^2)}{\partial \ln Q^2} = \frac{\alpha_s(Q^2)}{2\pi} \int_x^1 \frac{\mathrm{d}z}{z} \left[\sum_j q_j(z,Q^2) P_{ij}\left(\frac{x}{z}\right) + g(z,Q^2) P_{ig}\left(\frac{x}{z}\right) \right], \quad (2.22)$$

$$\frac{\partial g(x,Q^2)}{\partial \ln Q^2} = \frac{\alpha_s(Q^2)}{2\pi} \int_x^1 \frac{\mathrm{d}z}{z} \left[\sum_j q_j(z,Q^2) P_{gj}\left(\frac{x}{z}\right) + g(z,Q^2) P_{gg}\left(\frac{x}{z}\right) \right]. \quad (2.23)$$

The index i and j run over the quark and anti–quark flavours. The $P_{ij}(z)$ are the *splitting functions* (see Fig. 2.8), perturbatively calculable functions describing the parton emission. They give the probability for parton branchings $q \to q'g$, $g \to q\overline{q}$ and $g \to gg$ of a initial parton, where the radiated parton is emitted having a fractional momentum $(1 - z)$ leaving the initial parton holding the fraction z of its momentum. The splitting functions $P_{ij}(z)$ are calculated as a power of series of $\alpha_s(Q^2)$ up to a given order in α_s

$$P_{ij}(z, \alpha_s) = \delta_{ij} P_{ij}^0(z) + \frac{\alpha_s}{2\pi} P_{ij}^1(z) + \cdots. \quad (2.24)$$

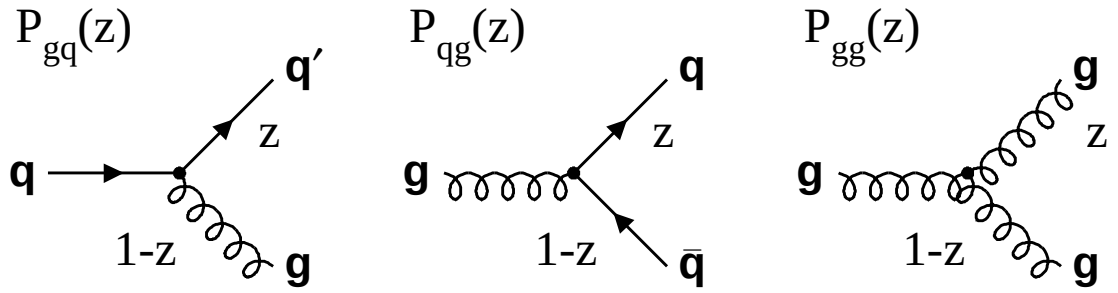

Figure 2.8: Feynman diagrams for the different splitting functions $P_{ij}(z)$; $i, j \in q, g$. Processes $q \to q'g$, $g \to q\overline{q}$ and $g \to gg$ are shown.

The leading order $P_{ij}^0(z) \equiv P_{ij}(z)$ are then given by

$$P_{qq}(z) = \frac{4}{3}\frac{1+z^2}{1-z}, \qquad P_{gq}(z) = \frac{4}{3}\frac{1+(1-z)^2}{z},$$
$$P_{qg}(z) = \frac{z^2+(1-z)^2}{2}, \qquad P_{gg}(z) = 6\Big(\frac{z}{1-z} + \frac{1-z}{z} + z(1-z)\Big). \tag{2.25}$$

The evolution equations (2.22, 2.23) can be solved by inserting a certain starting scale Q_0^2 and evolving them to higher Q^2. In a 'DGLAP QCD fit' as the H1 fit shown in Fig. 2.4, parton distributions can be extracted from measured structure function $F_2(x, Q^2)$ by parameterizing the parton distributions as

$$f_i(x, Q_0^2) \longrightarrow f_i^{\{a_j\}}(x, Q_0^2)$$

at Q_0^2. The free parameters $\{a_j\}$ are determined from a fit in which these parton distributions evolve according to the DGLAP equations [10]. In the top of the quark distribution, the gluon density can be accessed through the role it plays in the scaling violation (see equations (2.22, 2.23)). Fig. 2.9 shows the global increase of the gluon distributions with increasing the momentum transfer, i.e. the resolution power Q^2 as extracted by the H1 collaboration.

The phase space in DGLAP is approximated by a fraction where the emitted partons are ordered according to their transverse momenta[9] (see Fig. 2.10) — the imminent parton that bounds to photon has the highest transverse momentum k_T while its longitudinal momentum x stays lowest. Thus, only those configurations are summed which

[9] transverse momentum of the parton is taken relative to the motion of the initial parton before the gluon radiation

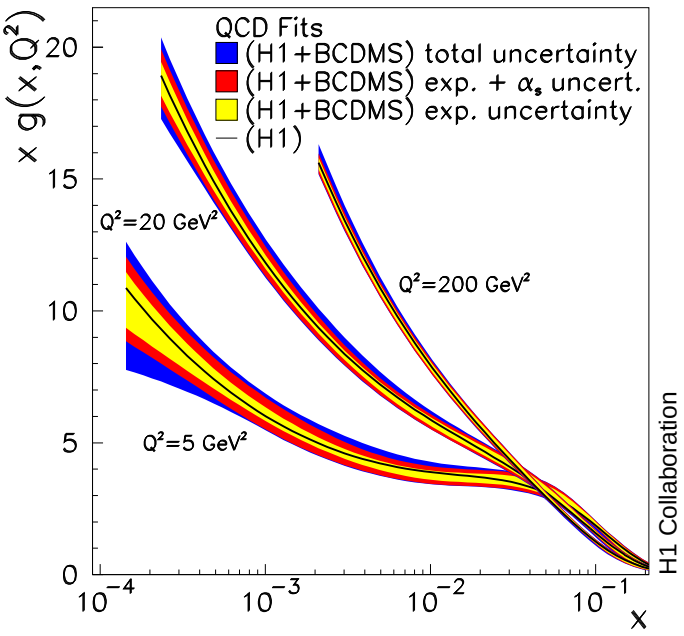

Figure 2.9: The gluon distribution $xg(x, Q^2)$ in the proton obtained from the DGLAP fit to $F_2(x, Q^2)$ data from H1 and BCDMS shown for a different values of $Q^2 = 5,\ 20,\ 200$ GeV^2. The $\alpha_s(M_{Z^0}) = 0.115$ and $Q_0^2 = 4$ GeV^2.

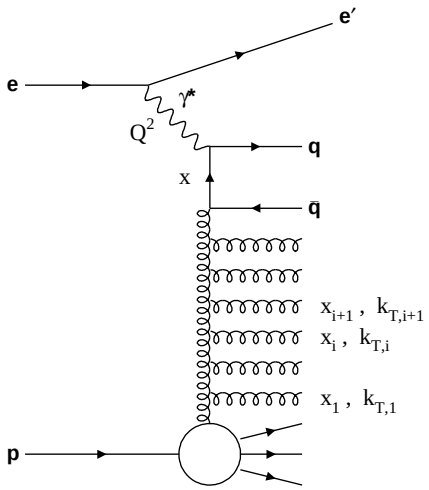

Figure 2.10: The 'ladder' diagram of the QCD parton evolution of the structure function F_2. The DGLAP approach corresponds to ordered parton emissions strongly in k_T ($k_{T,1} \ll k_{T,2} \ll \ldots \ll Q^2$) and weakly in x ($x_1 > x_2 > \ldots > x$).

fulfill the request of

- Strong ordering of transverse momenta $k_{T,i}$: $k^2_{T,i} \ll k^2_{T,i+1} \ll \ldots \ll Q^2$;
- Ordering of longitudinal momenta x_i : $x_i > x_{i+1} > \ldots > x$.

The summing of the terms of the order of $(\alpha_s \ln Q^2)^n$ holds in the kinematic region where [4]

$$\begin{aligned} \alpha_s(Q^2)\ln(Q^2/Q_0^2)) &\sim 1, \\ \alpha_s(Q^2)\ln(1/x) &\ll 1, \\ \alpha_s(Q^2) &\ll 1. \end{aligned}$$

Therefore to access the regions of lower x, where the terms of $\alpha_s \ln(1/x)$ are larger and become important, a second approach comes out.

The BFKL evolution

In the Balitzky, Fadin, Kuraev, Lipatov (BFKL) approximation the summing over the terms of $(\alpha_s \ln(1/x))^n$ takes place. These terms become significant at very low x and this approach is more precise in this region. The gluon ladder doesn't need to be ordered in k_T, therefore the gluon distribution is not integrated over k_T but, instead,

an *unintegrated gluon distribution* $\mathcal{F}(x, k_T^2)$ is defined and related to the conventional gluon distribution $g(x, Q^2)$ as

$$xg(x, Q^2) = \int^{Q^2} \frac{\mathrm{d}k_T^2}{k_T^2} \mathcal{F}(x, k_T^2).$$

The BFKL then predicts the gluon distribution evolution at leading order in $\ln(1/x)$ and fixed α_s to be [4]:

$$xg \sim x^{-0.5} \tag{2.26}$$

taking only those gluon ladder diagrams fulfilling

- No ordering of transverse momenta $k_{T,i}$ — a so–called *random walk*
- Strong ordering of longitudinal momenta x_i: $x_i \gg x_{i+1} \gg \ldots \gg x$

and lay in the kinematic region of

$$\begin{aligned} \alpha_s(Q^2)\ln(Q^2/Q_0^2)) &\ll 1, \\ \alpha_s(Q^2)\ln(1/x) &\sim 1, \\ \alpha_s(Q^2) &\ll 1. \end{aligned}$$

2.1.5 Photoproduction

In the region of $Q^2 \to 0$ the photon is nearly real. As the *ep* differential cross–section (2.9) contains a propagator of the form $1/Q^4$, collisions at HERA are dominated by such photoproduction interactions. The total photoproduction cross–section arises mainly from soft processes, resulting in the production of low p_T final states.

However, the high p_T interactions are also observed in photoproduction and could be subdivided into two classes. In *direct* processes the photon interacts directly with the parton from the proton, while *resolved* processes involve the interaction between the hadronic structure of a photon and that of the proton. An example of the direct processes is the *QCD-Compton interaction* leading to a final state containing the proton remnant and two jets in the final state. These jets arise from the hadronization of the quark and gluon. Another direct process is *photon–gluon fusion* where the photon interacts with a gluon from the proton via the fluctuated $q\overline{q}$ pair which is also visible by two jets after the hadronization.

2.2 Diffraction

Unlike in the deep inelastic scattering, the diffractive processes do not lead to the proton break up due to the parton being struck off the proton, but to the elastic proton scattering or to subsequent proton decay into hadronic final state due to its excitation (called

proton dissociation). Depending on the momentum transfer squared Q^2 the diffractive processes can be divided into

- **Diffractive photoproduction** (low Q^2)
- **Diffractive electroproduction** (high Q^2)

Such diffractive interactions have been studied by the hadron–hadron reactions at high energies, as well as in the lepton–hadron reactions. In the interaction the *pomeron* – a colourless pseudo particle with the quantum numbers of the vacuum (zero charge, isospin and baryon number, $C = P = +1$) – is exchanged between the photon and the proton. Measurements of diffractive events with jet production was the first hint of the partonic structure of the pomeron. In a QCD model for the pomeron exchange, diffractive events were proposed to be described by two gluon exchange. This can be tested at HERA studying e.g. vector meson production.

In the following, the brief explanation of the diffractive meaning is given and after the photon–proton (γp) diffractive processes observed at HERA are described.

2.2.1 Diffraction in Elastic Hadron–Hadron Reactions

In Fig. 2.11 the elastic proton–proton cross–section is plotted for different CMS energies as a function of $|t|$ where t is the squared momentum transfer between the two hadrons. All curves demonstrate an exponential increase in the cross–section for $|t| \to 0$. As can be seen, moving into the area of higher CMS energies, an obvious *local minimum and maximum* appears in addition. This shape is similar to the one created by diffraction of the light passed a hole with the shape of a circular disc. Beyond, the shape of the $\frac{d\sigma}{dt}$ cross–section down to the first minimum can be described by

$$\frac{\frac{d\sigma}{dt}}{(\frac{d\sigma}{dt})|_{t=0}} = e^{bt} \approx 1 - b(p\theta)^2, \tag{2.27}$$

where the θ is the scattering angle of the proton and b is defined as the *slope parameter*, while the optical diffraction for $kR \gg 1$ is described as

$$\frac{I}{I_0} \approx 1 - \frac{R^2}{4}(k\theta)^2, \tag{2.28}$$

which describes the fraction of observed intensity I with respect to the initial intensity I_0 as a function of the diffraction angle θ, where R is the radius of the disc hole and k is the wave number of the incident light wave. After further relations between these two equations, i.e. association of R with b as $b = R^2/4$ and let R be the typical strong interaction radius, $R \approx 1/m_\pi$, the t–slope would be of $b = 12.5$ GeV^{-2}, the right order of magnitude as already measured [9]. Because of this formal similarity, this elastic scattering and related processes are named as *diffractive*.

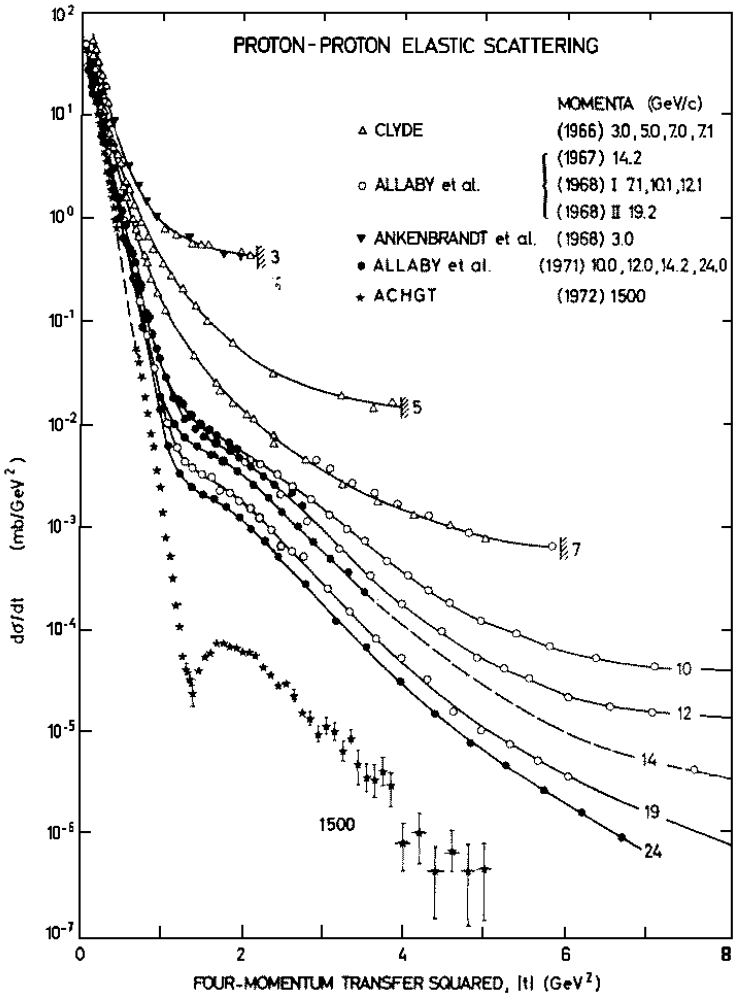

Figure 2.11: The proton–proton elastic scattering cross–section differential in the four momentum square t for different CMS energies. The diffractive behaviour of the slope and second maximum at high CMS energies is observed.

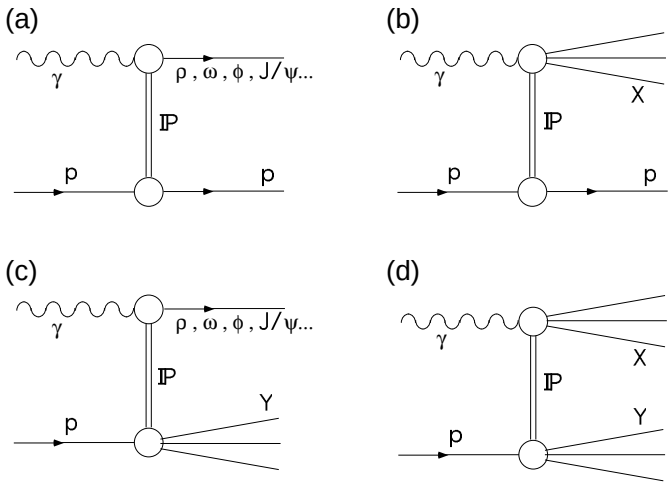

Figure 2.12: The four possible γp diffractive processes: *(a)* Quasi–elastic vector meson production, *(b)* proton elastic photon dissociation, *(c)* proton dissociative vector meson production and *(d)* double dissociation.

2.2.2 γp Diffraction

However, diffraction is not familiar only to the proton–proton cross–sections, but takes place also in the photon–proton processes, where one or both particles *dissociate* into an unbound number of final states.

The γp diffractive processes include several possibilities for the photon and proton final behaviour. According to the Fig. 2.12 they are:

a) **Quasi–elastic vector meson production** $\gamma p \longrightarrow Vp$
The photon can fluctuate into a vector meson V with the quantum numbers of the photon ($J^{PC} = 1^{--}$) and the proton stays intact;

b) **Proton elastic photon dissociation** $\gamma p \longrightarrow Xp$
The photon dissociates into a system X with the mass of M_X, proton still holds intact;

c) **proton dissociative vector meson production** $\gamma p \longrightarrow VY$
Photon fluctuates into a vector meson V and the proton dissociates into hadronic system Y of the mass M_Y and the proton quantum numbers $J^P = \frac{1}{2}^+$;

d) **Double dissociation** $\gamma p \longrightarrow XY$
Both, the photon and the proton dissociate into systems X and Y, respectively.

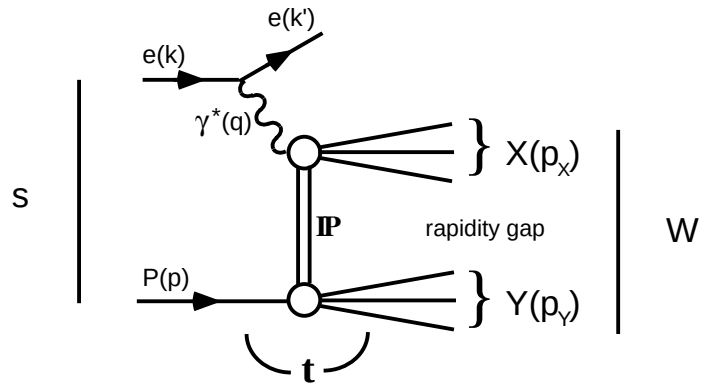

Figure 2.13: The kinematics of diffractive processes. Due to the pomeron exchange, the process lacks the hadrons created in DIS breaking the colour string between the proton and the struck quark. A large rapidity gap between X and Y system can be seen – a proof that the exchange between the photon and the proton was colourless.

Diffractive Kinematics

Due to splitting the final state particles into two systems (see Fig. 2.13), additional variables can be specified in the diffractive kinematics. Because of the colourless pomeron, only energy and momentum are exchanged. If the 4–vectors of the X and Y systems are p_X and p_Y, respectively, then their masses are given by

$$M_X^2 = p_X^2, \qquad M_Y^2 = p_Y^2 = (p - p_X + q)^2. \tag{2.29}$$

The absence of exchanged colour creates a large rapidity gap between the X and the Y system.

Among the standard DIS variables (2.2, 2.3, 2.4, 2.5, 2.7) which remain valid, several new ones can be introduced. They are:

- the dimensionless variable $x_{I\!P}$ defined as

$$x_{I\!P} \equiv \frac{q \cdot (p - p_Y)}{q \cdot p} = \frac{Q^2 + M_X^2 - t}{Q^2 + W^2 - M_p^2} \ , \tag{2.30}$$

  which can be interpreted as the *momentum fraction of the proton carried by a pomeron*;

- the dimensionless variable $y_{I\!P}$ defined as

$$y_{I\!P} \equiv \frac{p \cdot (q - p_X)}{q \cdot p} = \frac{M_Y^2 - M_p^2 - t}{Q^2 + W^2 - M_p^2} \ , \tag{2.31}$$

interpreted as the *fraction of the photon momentum seen by the pomeron*;

- the *momentum transfer t at the proton vertex* given by

$$t \equiv (p - p_Y)^2 = (q - p_X)^2 \ ; \tag{2.32}$$

- and the dimensionless variable β defined as

$$\beta \equiv \frac{-q^2}{q \cdot (p - p_Y)} = \frac{Q^2}{Q^2 + M_X^2 - t} \ ; \tag{2.33}$$

which can be interpreted as the *momentum fraction of the pomeron carried by the interacting quark*. Taking into account the Bjorken x as defined in (2.3), β can be also defined as

$$\beta = \frac{x}{x_{I\!P}}, \tag{2.34}$$

showing the analogy between β and x in a standard deep inelastic scattering.

The Diffractive Structure Function

In a similar way to inclusive measurement a structure function of the exchange object (the pomeron) can be defined. In the elastic case, the diffractive structure function $F_2^{D(4)}$ depends on four variables – β, $Q^2, x_{I\!P}$ and t. According to the DIS cross–section (2.9), the diffractive cross–section can be written as

$$\frac{\mathrm{d}\sigma_{ep\to eXY}}{\mathrm{d}\beta \mathrm{d}Q^2 \mathrm{d}x_{I\!P} \mathrm{d}t} = \frac{4\pi\alpha_{em}^2}{\beta Q^4}\Big(1 - y + \frac{y^2}{2[1 + R^{D(4)}(\beta, Q^2, x_{I\!P}, t)]}\Big) F_2^{D(4)}(\beta, Q^2, x_{I\!P}, t), \tag{2.35}$$

where $R^{D(4)}(\beta, Q^2, x_{I\!P}, t)$ is (similary to R in (2.10)) the ratio of the diffractive longitudinal to transverse photon cross–sections σ_L^D and σ_T^D, respectively

$$R^{D(4)}(\beta, Q^2, x_{I\!P}, t) \equiv \frac{\sigma_L^D(\beta, Q^2, x_{I\!P}, t)}{\sigma_T^D(\beta, Q^2, x_{I\!P}, t)} \tag{2.36}$$

and since, for not too large y, the contribution from the longitudinal photon can be neglected, $R^{D(4)} = 0$.

If the detector is not equipped of proton spectrometer, the scattered proton (or the Y system in the dissociative case) escape detection through the beam pipe, leading p_Y unmeasurable. In the inclusive case, the X system cannot be measured with enough precision to determine in an accurate way the t variable from the p_X measurement. Therefore, the triple–differential diffractive cross–section is introduced

$$\frac{\mathrm{d}\sigma_{ep\to eXY}}{\mathrm{d}\beta \mathrm{d}Q^2 \mathrm{d}x_{I\!P}} = \frac{4\pi\alpha_{em}^2}{\beta Q^4}\Big(1 - y + \frac{y^2}{2}\Big) F_2^{D(3)}(\beta, Q^2, x_{I\!P}), \tag{2.37}$$

where

$$F_2^{D(3)}(\beta, Q^2, x_{I\!P}) = \int \mathrm{d}t \; F_2^{D(4)}(\beta, Q^2, x_{I\!P}, t) \tag{2.38}$$

and t is integrated over the whole t range. Note that only in case of measured scattered proton and in case of exclusive final state the t dependence can be measured.

If the diffractive vertex factorizes, then the structure function can be separated in terms involving variables describing the lower end of the pomeron exchange and terms involving variables describing the upper end,

$$F_2^{D(3)}(\beta, Q^2, x_{I\!P}) = f_{I\!P/p}(x_{I\!P}) F_2^{I\!P}(\beta, Q^2) \ , \tag{2.39}$$

where $f_{I\!P/p}$ is the flux factor of the pomeron in the proton.

Rapidity Gap

It was predicted by Bjorken that the most evident signal for diffractive processes at high energy is the presence of large spatial gaps between the emerging angles of the outgoing systems X and Y. These angles are defined by the variable $\mathcal{Y}$ called *rapidity* which is defined as

$$\mathcal{Y} \equiv \ln \frac{E_A + k_{A,l}}{E - k_{A,l}}, \tag{2.40}$$

where the $k_{A,l}$ is the longitudinal momentum of the particle A. Its assymptotic equivalent for the zero mass of the particle, *pseudorapidity* η, is given as

$$\eta \equiv -\ln \tan \frac{\theta_A}{2}. \tag{2.41}$$

In a typical DIS event the struck parton from the proton emerges at the angle θ_A, with respect to the proton remnant direction ($0 < \theta_A \leq 180°$) as shown at Fig. 2.14. This emerging angle can be expressed in terms of the difference in total pseudorapidity η between the direction of the proton remnant and the particle A as

$$\Delta\eta = \eta_{remnant} - \eta_A \ , \tag{2.42}$$

which can be linked to the kinematics by the relation

$$\Delta\eta \sim \ln \frac{W}{M_p} - \ln \frac{xW}{M_p} = \ln \frac{1}{x}. \tag{2.43}$$

The $\ln(W/M_p)$ covers the pseudorapidity of $\gamma^* p$ system while $\ln(xW/M_p)$ represents the pseudorapidity of the $\gamma^* q$ system.

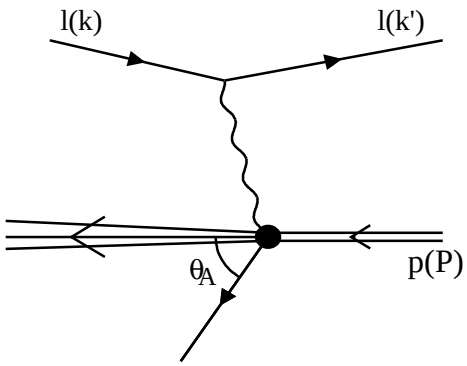

Figure 2.14: The schema of DIS event with the outgoing particle A at the angle θ_A.

In the DIS process, the struck quark and the proton remnant are connected with each-other by the so–called *colour string* and if, by the momentum transfer from the photon, this string breaks, the rapidity gap seen in diffraction fills up with colourless hadrons. This does not happen in the diffractive processes, where the photon interacts with the colourless pomeron. This means that no colour string is expected to break and thus no hadronization occurs in a large space.

2.2.3 Photon and Vector Meson Production

A real photon or vector meson (either light or heavy) alone can be produced in diffractive process as the X system (see Fig. 2.15). From the proton rest frame it can be viewed as if the photon emitted by the incoming electron would fluctuate into a vector meson which then scatters diffractively on the proton. Only vector mesons having the same quantum numbers as the photon can be produced, since the interaction involves the pomeron with quantum numbers of vacuum. This is described within the *Colour Dipole Model*.

The measured cross–section for vector meson production in photoproduction ($Q^2 \simeq 0$) is shown at Fig. 2.16. as a fuction of W – the photon–proton centre–of–mass energy. Production of light vector mesons ρ, ϕ and ω is characterized by a weak dependence in W typical of 'soft interactions'. On the other hand, in the case of heavy vector mesons like J/ψ ($c\overline{c}$) or Υ ($b\overline{b}$), the charm or the beauty mass m_c or m_b provides the hard scale by $\mu_r^2 = m_{c,b}^2$, a stronger W dependence is observed, called 'hard interactions'.

The Two Gluon Exchange Model was invented as a model for the pomeron applied to the diffractive production of vector mesons. The virtual photon emitted by the

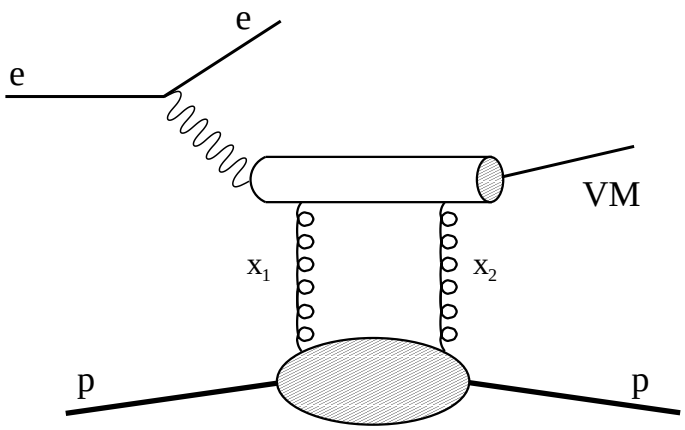

Figure 2.15: The vector meson production. The incoming electron emits the photon which then fluctuates into a vector meson and interacts with proton by pomeron exchange. The meson is diffractively scattered.

incoming electron fluctuates into a $q\overline{q}$ system which then interacts with the proton by exchange of two gluons. The $q\overline{q}$ then recombines to the vector meson if these two quarks are close in the phase space.

2.2.4 Diffractive Photoproduction at high t

The hard scale of diffractive processes can occur either due to high momentum square transfer Q^2, to the high mass square M_X^2 of the X system or to the large four momentum transfer at the proton vertex t.

The high mass system X becomes important for diffractive production of heavy vector mesons such as the J/ψ and Υ. Concerning the momentum square transfer t, in case that its value is higher than that of the scale parameter Λ_{QCD} ($-t \gg \Lambda_{QCD}$), the hard scale that is present in the process propagates from the proton side instead of the photon side, while assuming low Q^2. The high t photoproduction process is depicted at Fig. 2.17 for the γ scattering.

Many measurements have been made so far of processes at high t such as the double dissociation, rapidity gaps between jets or diffractive vector meson production. However, in the double dissociations or large rapidity gaps between jets could raise the uncertainty in the final cross–sections due to possibility of subsequent spontaneous strong interactions between the hadronic systems destroying the rapidity gap. Also, computing the vector mesons requires the transition from the $q\overline{q}$ pair to the final vector meson to be

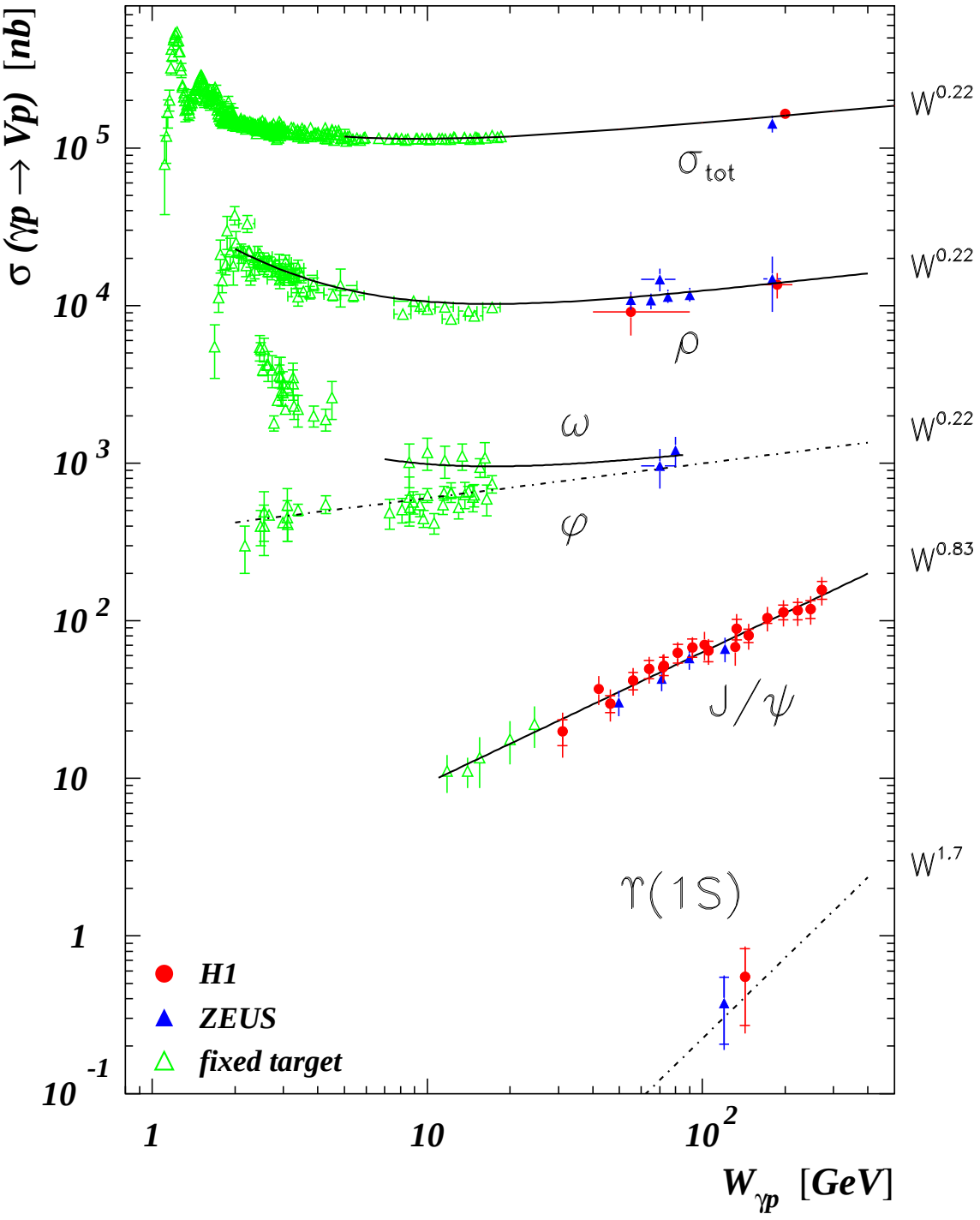

Figure 2.16: Vector meson production cross–sections as a function of the photon–proton CMS energy W. For light vectors the cross–section is described by a soft energy dependence. For the heavy vector production the W dependence of the cross–sections is significantly steeper, than that for the light vector mesons.

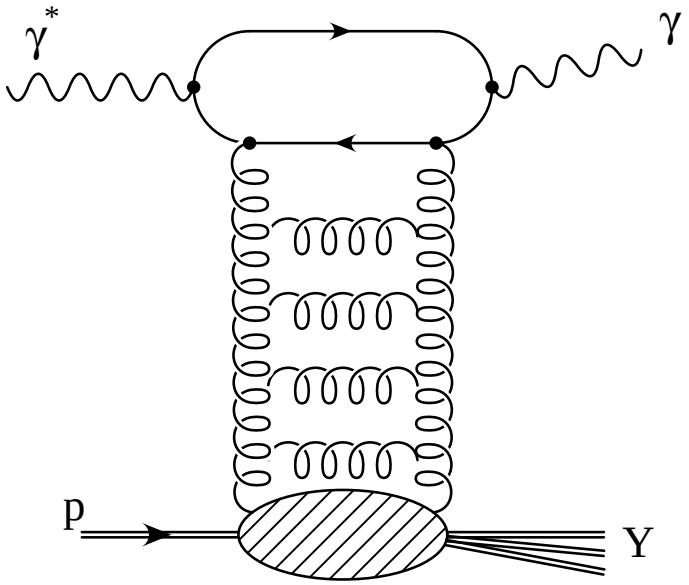

Figure 2.17: The diffractive photoproduction at high t described by introducing the BFKL ladder.

modelled since it is not calculable within perturbative QCD.

On the other hand, the case of diffractive photon scattering $\gamma p \longrightarrow \gamma Y$ avoids both the problems, since the X system reduces into a single real photon, thus the strong interaction with the proton remnant is suppressed; also any further knowledge of vector mesons is obviously not needed.

Furthermore, having only one final photon in the main H1 detector, the spatial acceptance is larger compared to the vector meson production where the subsequent decays of the particles increase final multiplicity to be detected. The extension of angular acceptance corresponds to smaller x, i.e. in the optimal region to the BFKL predictions. Together with the clean signature of this process, the diffractive photoproduction of photon at large t gives a high possibility to precise measurement of the cross–section.

Chapter 3

HERA and the H1 Detector

In this chapter, the HERA[1] accelerator located at the DESY[2] laboratory and the H1 experiment are introduced, followed by the description of particular subdetectors used in this analysis — according to their setup at 1999/2000 running period. The trigger system is also described.

3.1 HERA, the Electron—Proton Collider

HERA, as a first electron[3]– proton collider ever built, is situated in Hamburg, Germany. From year 1992, when the first running period started, it continues producing a huge amount of physical information.

Concerning the 1999/2000 running period, electrons with the energy of $E_e = 27.6$ GeV are collided with protons of $E_p = 920$ GeV, that leads to an energy in the centre–of–mass system $\sqrt{s} \simeq 318$ GeV. HERA consists of two separate accelerators for electrons and protons, the *HERA-e ring* and the *HERA-p ring*, as seen in Fig. 3.1. These beam lines, located in the same underground tunnel, have a circumference of 6.3 km. Each of them is equipped with adequate magnets and accelerating cavities. In the HERA-e ring lay conventional dipole bending magnets at the magnetic field strength of $B \approx 0.17$ T, while in the HERA-p ring, there are superconducting magnets cooled with the liquid helium that can provide a field strength of $B \approx 5.3$ T. The energy loss of protons concerning synchrotron radiation can be neglected due to their relative high mass. Therefore, the proton energy is limited only by the field strength of the bending magnets, while the maximum energy of electrons is limited by the cavities that accelerate electrons and

[1] ***H****adron—****E****lektron* ***R****ing****A****nlage*

[2] ***D****eutches* ***E****lektronen****S****ynchrotron*

[3] in certain periods, *electrons* were replaced by *positrons* that – as far as for this analysis – could be treated as the same particle

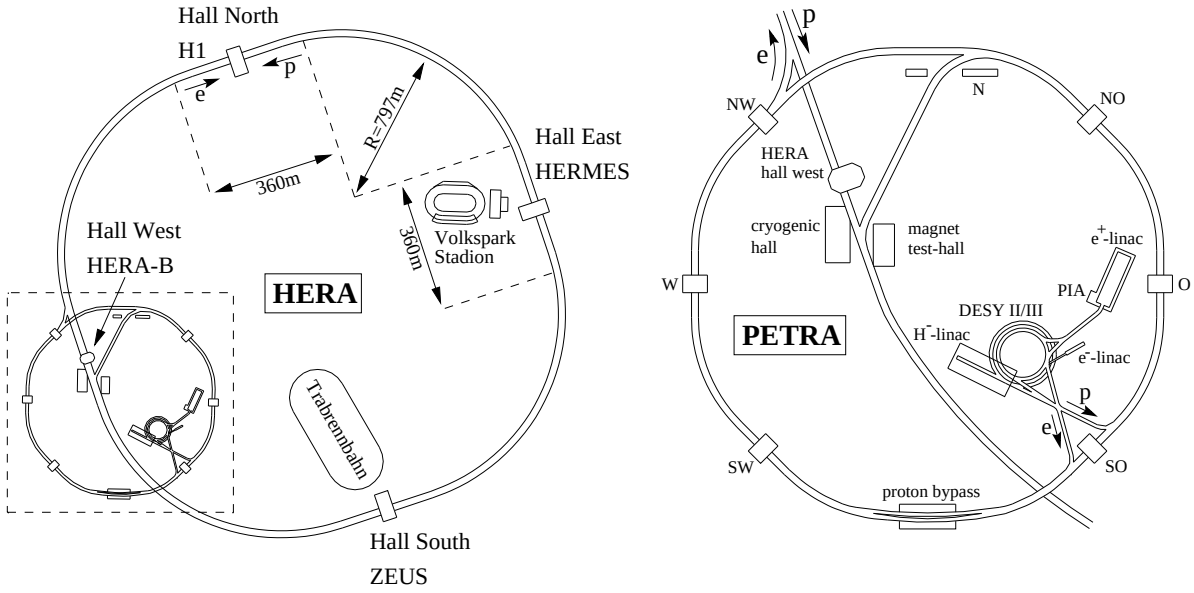

Figure 3.1: The HERA facility – accelerator chains.

compensate their energy loss due to synchrotron radiation.

To achieve the final energy of colliding particles, a set of pre–accelerators is needed; separately for electrons and protons.

Electrons Electrons (and positrons) are provided by one of the 500 MeV linear accelerators named LINAC[4] and then ramped up in DESY-II machine and accelerated to 7.5 GeV. Up to 60 bunches are then filled and stored in PETRA-II facility and further accelerated to 12 GeV. Four such fillings are injected straight into the HERA-e ring and accelerated again up to their colliding energy $E_e = 27.6$ GeV. Since the middle of the year 1994 HERA has accelerated positrons rather than electrons. This change was made because of an effect of the distributed getter pump which maintains a high vacuum in the electron ring.

Protons Free protons are produced by passing negatively charged hydrogen atoms H^-, accelerated to an energy of 50 MeV in H-LINAC, through a stripping foil, where the ions loose their two electrons and continue to accelerate up to an energy of 7.5 GeV in DESY-III and injected into the PETRA-II storage ring afterwards. Here, maximum of 70 proton bunches are accumulated and then accelerated to 40 GeV. Again, four PETRA-II fillings of these are injected into the final HERA-p ring and accelerated to

[4]simply from ***LIN****ear* ***AC****celerator*

the final colliding energy of $E_p = 920$ GeV.

Each of the electron and proton fill contains up to 220 bunches containing 10^{10} to 10^{11} particles crossing with a frequency ν_{cross} and time crossing interval t_{cross} of

$$\nu_{cross} \;=\; 10.4 \text{ MHz}, \qquad t_{cross} \;=\; 96 \text{ ns}.$$

The lifetime of the beams is about 100 hours for protons and around 10 hours for electrons. By the year 2000, an electron current of 40 mA and a proton current of 90 mA was achieved leading to peak luminosity $\mathcal{L}$ of

$$\mathcal{L} \;=\; 1.5 \times 10^{31} \text{cm}^{-2}\text{s}^{-1} \;=\; 15\ \mu\text{b}^{-1}\text{s}^{-1}$$

and reached the designed value. The integrated luminosity L, is a measure of the amount of data collected at the collider during a certain period:

$$L \;=\; \int \mathcal{L}(t)dt$$

The integrated luminosity collected along years can be seen at Fig. 3.2.

HERA Physics Programme

Two interaction points of colliding bunches are designed at the northern and the southern point of HERA. Around these points, two multipurpose detectors for H1 (Hall North) and ZEUS (Hall South) experiments are constructed taking data from 1992. The main topics concerning these colliders are

- Precision measurements of the proton structure functions $F_2(x,\ Q^2)$
- The search for substructures of quarks and leptons
- The investigation of heavy flavour production mechanisms
- The analysis of the structure of the photon
- The investigation of diffractive phenomena
- Measurements of α_s
- The search for a new physics beyond the standard model

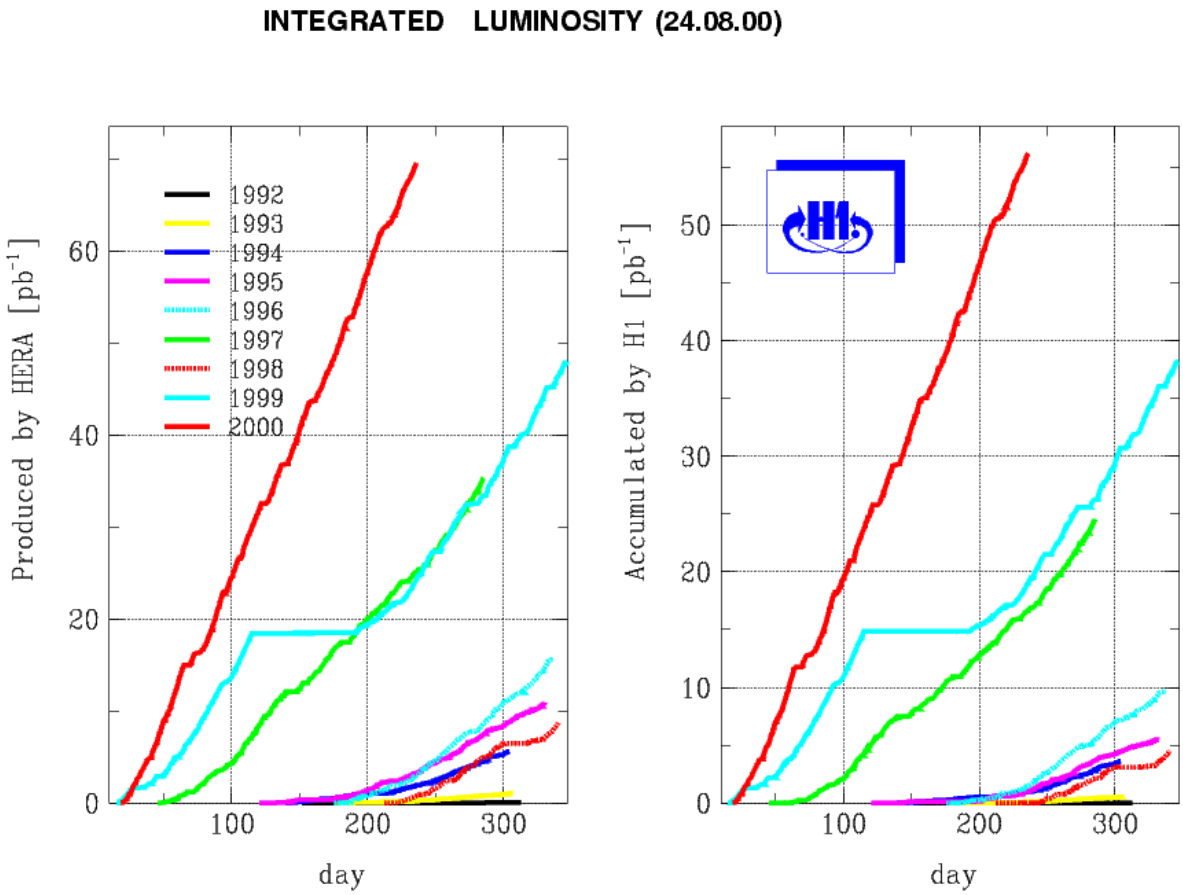

Figure 3.2: The integrated luminosity produced by HERA and collected by H1 detector over the 1992 — 2000 period.

Among these colliders, experiments with fixed targets are built. One of them, the HERMES detector is in the Hall East is a spectrometer taking data since the year 1995 and studies interactions of polarized electrons from the electron beam in the main collider with a polarized gas target (H_2, He, D) and the aim is to study the spin structure of proton. The other one situated in Hall West, HERA-B, was producing data until year 2003. This forward spectrometer used internal wire target to produce interactions between protons from the halo of the proton beam and nucleons of the target wire. Aim here was to study CP–violation in a decay of neutral B-mesons.

3.2 The H1 Detector

The H1 Detector is a multi-purpose apparatus designed to study the final state particles from the electron–proton scattering. It has a mass of 2800 tons and a volume approximately of $12 \times 10 \times 15$ m^3. Due to the type of interactions taking place in this experiment, the detector has to satisfy some basic requirements like precise calorimetric measurement for all scattering angles of the electron in a forward[5], central and backward direction. This is crucial in neutral current events, where the kinematic variables are reconstructed from the properties of scattered electron. In the way of charged current interactions, detector has to be hermetic in order to measure all final state particles to determine the missing momentum needed when neutrino leaves the detector unseen.

The schematic view of the central part of the H1 detector is shown in Fig. 3.3. Electrons enter from the left side through the beam pipe 1 and protons from the right side. The positive z-axis of the H1 coordinate system is defined by the direction of the outgoing proton beam, x points towards the centre of the HERA ring and y-axis vertically upwards — so that a right–handed coordinate system is used. At the polar coordinate system, the z-axis and the x-axis correspond to polar $\theta = 0$ and azimuthal $\phi = 0$, respectively. Because of quite different beam energies of the colliding particles, the electron–proton centre–of–mass system is boosted in the forward direction. The H1 detector is therefore strongly asymmetric with respect to the interaction point, with the finer granularity in its forward region and, therefore, obtaining better spatial resolution there.

The interaction point is located at the centre of the detector, as indicated at the bottom right corner of a mark 2 . It is covered by central and 3 forward tracking detectors measuring the transverse momenta of charged particles in a magnetic field. On the top of these, a large calorimeter system is placed, consisting of LAr[6] calorimeter

[5] *forward* direction is defined by the proton's incoming direction, whereas *backward* is the direction of the incoming electron

[6] ***L**iquid **Ar**gon*

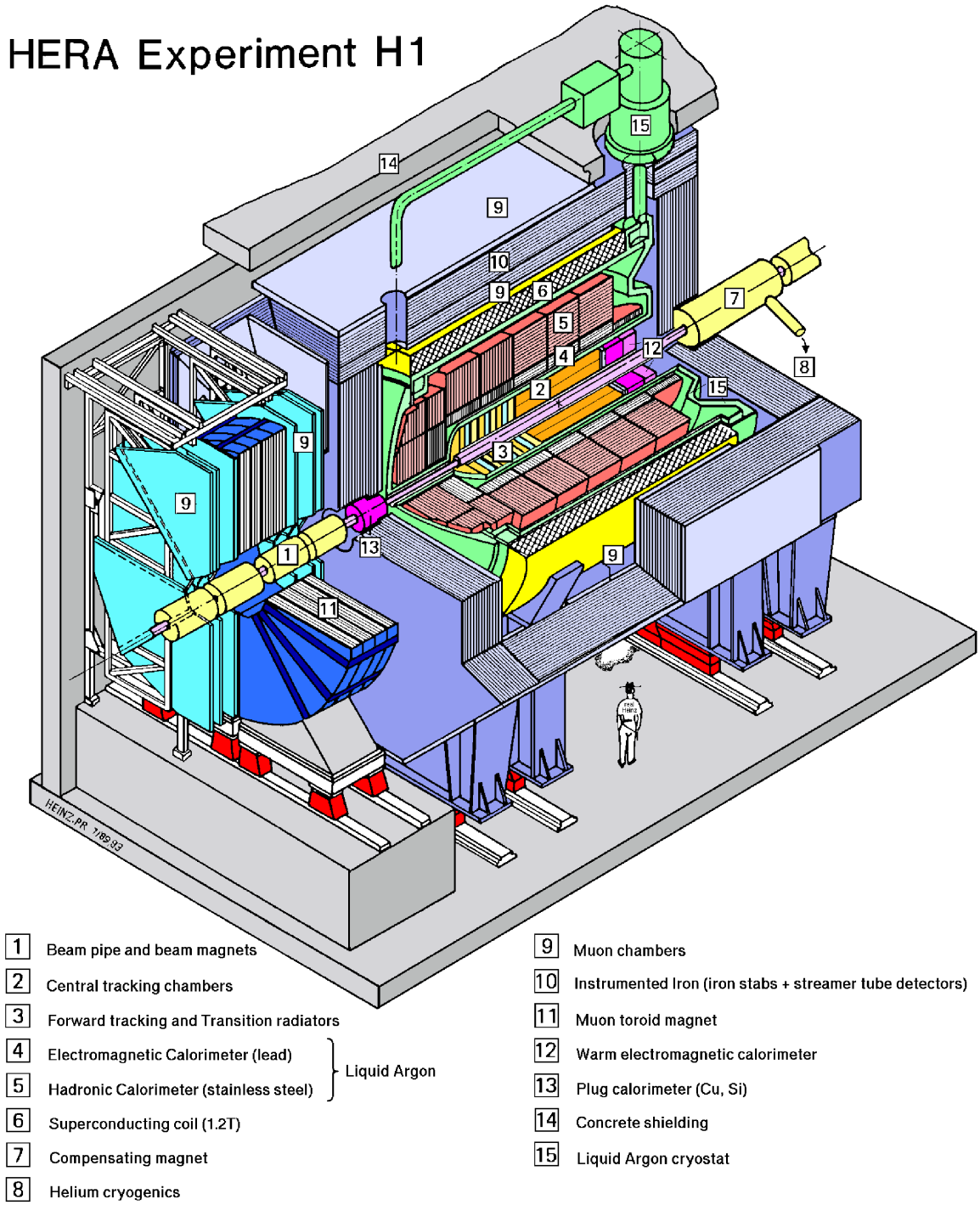

Figure 3.3: The H1 detector.

4 , 5 in the forward and central region, followed by the SpaCal[7] 12 in the backward region. Both of them are divided into electromagnetic and hadronic part to measure the energy depositions from the showers of different particles. The LAr is covered by a superconducting coil 6 providing almost a homogeneous magnetic field with only a few percent variation over the region of the tracking chambers. Within that region, 3600 mm in length and 1600 mm in diameter, the field has an average value of 1.15 T over the tracking region. An additional Plug calorimeter 13 is installed in the most forward direction very close to the beam pipe. For the particles that escaped from the inner parts of the detector, an iron return yoke 10 is used. Mainly muons and also the energy deposits of hadrons are detected here. The forward muon detector 11 identifies and measures the momentum of muons using the drift chambers and a toroidal magnet. Except of this central part, an additional detectors along the z-axis in the HERA tunnel are placed, either to determine the luminosity of the beam and detecting the low–angle scattered electrons (the electron tagger at $\approx$ –33 m, photon detector at $\approx$ –103 m) or to measure the energy and angle of produced neutrons in reaction $ep \longrightarrow enX$ (FNC[8] at $\approx$ +107 m) and to detect remnants of the proton (PRT[9] at $\approx$ +26 m) or the protons itself (FPS[10], with the most forward station at 90 m).

Now, detectors used in this analysis and the data acquisition are described more in detail.

3.2.1 The H1 Tracking System

Besides the momentum measurement, the extrapolation of the particle tracks allows the reconstruction of the event vertex. Because of the superconducting coil, a solenoidal magnetic field of strength 1.16 T is produced parallel to the beam axis, forcing charged particles to *Lorentz force* giving a curvature to their tracks if travelling perpendicular to the z-axis. The tracking system of H1 (see Fig. 3.4) has been designed to reconstruct jets with high particle densities and to measure the momentum and angles of charged particles with a precision $\sigma(\theta) \approx 1$ *mrad*. Because of the asymmetry between the electron and proton beam energies, many charged particles are produced in the forward direction. To maintain good efficiency for triggering and reconstruction over the whole angle, the tracking system is divided into the central (CTD) and forward (FTD) tracking devices together covering the angular range

$$15 < \theta < 165^\circ$$

[7] ***Spa****ghetti* ***Cal****orimeter*
[8] ***F****orward* ***N****eutron* ***C****alorimeter*
[9] ***P****roton* ***R****emnant* ***T****agger*
[10] ***F****orward* ***P****roton* ***S****pectrometer*

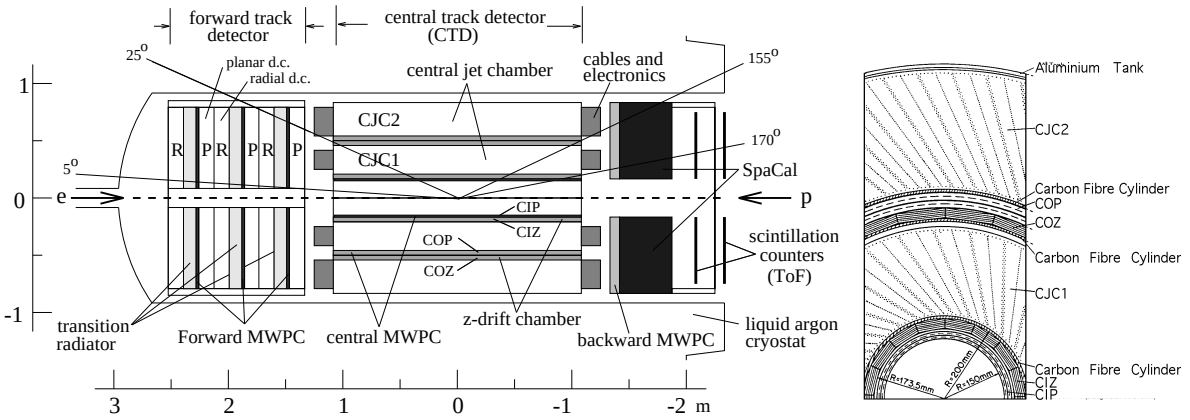

Figure 3.4: The H1 Tracking System. *left)* the longitudinal schematic view. *right)* the transverse view.

with full azimuthal acceptance.

The central tracking detector covers the angular range $25° < \theta < 155°$ and consists of two large concentric drift chambers CJC1[11] having 30 cells with 24 sense wires and CJC2 with its 60 cells and 32 wires, both having their wires mounted concurrently to the z-axis. CJC1 has the inner radius of 20.3 cm and outer radius of 45.1 cm, whereas CJC2 has the inner one of 53.0 cm and the outer one of 84.4 cm. Both have the length of 2.2 m and the space point resolution achieved in $(r,\ \phi)$ plane is 170 μm and 2.2 cm in the z-axis. From the signals from these chambers, the transverse track momentum is determined and the specific energy loss dE/dx is used to improve particle identification.

The z resolution is improved by two additional drift chambers CIZ[12] and COZ[13], with the sense wires mounted perpendicular to the beam axis and the drift direction occurs parallel to it. Obtained z resolution is 260 μm and the combination of all drift chambers leads to the momentum resolution σ for the track measurement of

$$\frac{\sigma(p_T)}{p_T} \ < \ 0.01\ p_T \text{ GeV}$$

The detector walls are thin to reduce photon conversion and the effect on identification of primary electrons. The complete system of the central tracking detectors is housed in a single aluminium cylinder of 4 mm wall thickness.

A fast tracking signal needed for the L1 level of the trigger system is obtained

[11] ***C**entral **J**et **C**hamber*
[12] ***C**entral **I**nner **Z** chamber*
[13] ***C**entral **O**uter **Z** chamber*

using the multi–wire proportional chambers CIP[14] and COP[15]. With these, the signal is delivered as fast as 21 ns, that is small enough for a time between two bunch crossings which is $t_{cross} = 96$ ns.

The track reconstruction is based on the track parametrization. The tracks of charged particles are characterized by the five helix parameters:

- *the signed curvature* $\kappa = \pm r^{-1}$; (r being the curvature radius)
- *the signed closest distance* d_{ca}, between the z-axis and the $(x,\ y)$ plane
- *azimuthal angle* ϕ
- *polar angle* θ
- *the z position* z_0 at the point of closest approach

The first three parameters are determined by a circle fit in the $(x,\ y)$ projection where the circle is expressed in a polar coordinates $(r,\ \varphi)$ as

$$\frac{1}{2}\kappa\Big(r^2\ +\ d_{ca}^2\Big) + (1 - \kappa d_{ca}) r \sin(\phi - \varphi) - d_{ca} = 0$$

In the stage of track fitting to the primary and secondary vertices, the parameters κ, ϕ, θ and the $x,\ y$ and z coordinates of the vertex are used.

The Backward Silicon Tracker

The Backward Silicon Tracker (BST) of the H1 experiment is designed to reconstruct the tracks of backward scattered electrons, i.e. close to the electron beam direction in deep inelastic electron-proton interactions (see Fig. 3.5).

In a fraction of DIS events where the final hadronic state is so close to the beam pipe that leaves the detector unseen, the electron track alone determines the vertex position. The H1 backward silicon tracker consists of eight planes of silicon detector discs with 16 wafers per disc. It has a polar angle acceptance of

$$162 < \theta < 176^\circ$$

covering an approximate range of $2 < Q^2 < 100$ GeV^2 for the nominal vertex position. The BST has a strip detector part with the circular strips of 48 micron pitch at constant radii and a pad detector part with pads of about 1 cm^2 size. The strip detector

[14] ***C**entral **I**nner **P**roportional chamber*
[15] ***C**entral **O**uter **P**roportional chamber*

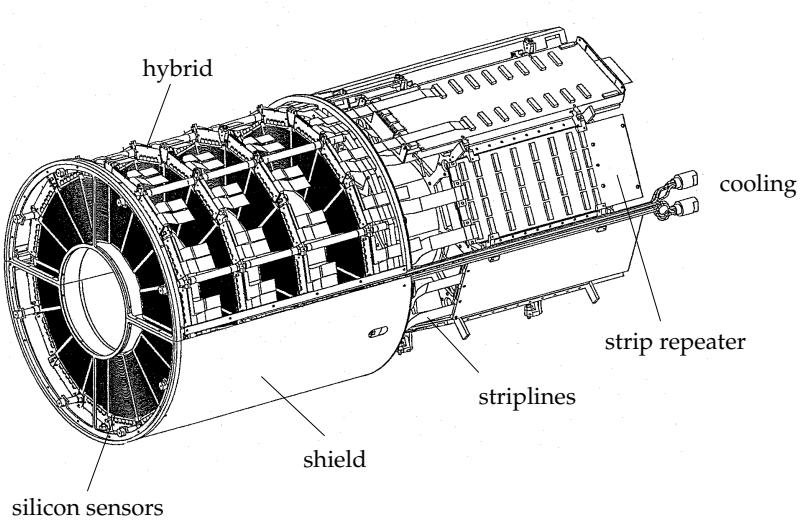

Figure 3.5: Schematic view of the 4 plane BST detector and associated repeater electronics.

measures the polar angle of backward scattered particles. The pad detector triggers on the backward deep inelastic electrons down to 1 GeV electron energy.

After leaving the tracking system, the particle energy is measured by one of the calorimeters installed around the trackers.

3.2.2 The Liquid Argon Calorimeter

A calorimeter measures the energy deposited by the incoming particles. If a particle is absorbed completely, the deposited energy corresponds to its total kinetic energy. The LAr calorimeter covers the angular range

$$3 < \theta < 153^{\circ}$$

with full azimuthal coverage. The schematic view of LAr is in Fig. 3.6. It is a sandwich type calorimeter composed of absorber plates supplemented with a high voltage. Between the plates, gaps are filled up by liquid argon, used as the active detection material, so the LAr is kept in a cryostat. The 8 wheels in the z-direction consist of 8 octants in ϕ each. The six central wheels are divided into the closer *electromagnetic part* and more remote *hadronic part*, with respect to the beam pipe. The remaining forward wheel consists of two hadronic sections whereas the most backward wheel has only one electromagnetic section.

The shower particles created by the incident particle ionize the argon and the number of created ion–electron pairs is proportional to the energy of the incident particle.

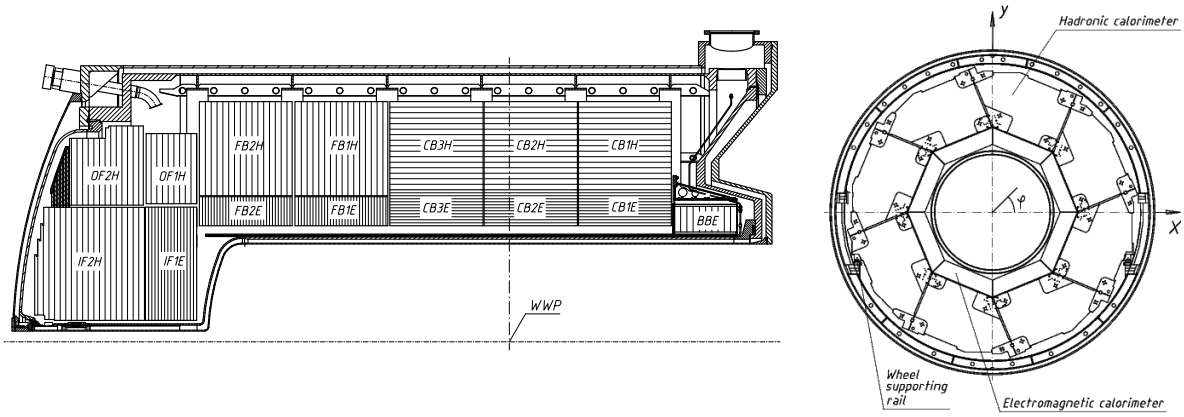

Figure 3.6: The layout of the Liquid Argon Calorimeter. *left)* the longitudinal view, *IF1E* to *BBE* are the electromagnetic wheels and *IF2H* to *CB1H* are the hadronic sections, WWP marks the interaction point. *right)* the transverse view of LAr.

The electrons are collected producing a signal proportional to the collected charge, and thus to the initial energy deposit. Since the ionization process is of statistical nature, the absolute energy resolution is $\sigma(E) \sim \sqrt{E}$.

All the electromagnetic sections consist of 2.4 mm lead absorber plates whose orientation it that particles are incident on the calorimeter with angles not smaller than 45°. Absorber plates correspond to 20 – 30 radiation lengths X_0, depending on the polar angle θ. Its resolution for the electron and photons is

$$\frac{\sigma(E)}{E} = \frac{11\%}{\sqrt{E\ [\mathrm{GeV}]}} \oplus 1\%$$

Hadronic sections consist of 19 mm stainless steel absorbers corresponding in total to 5 – 8 hadronic interaction lengths λ.

$$\frac{\sigma(E)}{E} = \frac{50\%}{\sqrt{E\ [\mathrm{GeV}]}} \oplus 2\%$$

Each calorimeter cell provides a calibrated charge. The reconstruction program converts charges from the showers into the energies separately in both, the electromagnetic and the hadronic part. The raw energy is then corrected for the effects of dead material[16], hadronic noise and the internal properties of the calorimeter, all derived using Monte Carlo simulations. Besides these, the charge output for hadrons is about 30% smaller than for electrons, resulting into additional correction to the signal obtained on

[16]the beam pipe, the central tracker, the inner cryostat wall ...

the electromagnetic scale.

The reconstruction program then forms the clusters from the near-by groups of cells. The cells containing energy depositions from an electromagnetic shower initiated by a photon or electron are merged into one cluster. Due to their large spatial fluctuations, hadronic showers are in general split into several neighbouring clusters.

3.2.3 The Backward Detectors — SpaCal & the BDC

The Spaghetti calorimeter, SpaCal, covers the backward region of the range

$$154 < \theta < 178^\circ$$

with full azimuthal coverage. It contains an electromagnetic and a hadronic part made of lead as absorber material and scintillating fibres (parallel to the beam axis) as active material. Incident electrons and photons create an electromagnetic shower in the lead which causes the fibres to scintillate. The light is then detected in photomultiplier tubes.

The calorimeter (see Fig. 3.7) consists of the inner electromagnetic section of the 28 radiation lengths with the energy resolution

$$\frac{\sigma(E)}{E} = \frac{7.1\%}{\sqrt{E\ [\mathrm{GeV}]}} \oplus 1\%$$

and the outer hadronic section corresponding to 2 interaction lengths and having the energy resolution

$$\frac{\sigma(E)}{E} = \frac{13\%}{\sqrt{E\ [\mathrm{GeV}]}} \oplus 4\%$$

The transverse size of cells in the electromagnetic SpaCal is 40×40 mm^2, the smallest mechanical unit has an intersection of 80×40 mm^2. 8 of these mechanical units are bound together into a supermodule with a size of 160×160 mm^2. These modules are stacked together forming the electromagnetic part of SpaCal. The hadronic part is formed out of modules with a size of 120×120 mm^2. Additionally, SpaCal itself is divided into the inner part within a radius of ≈ 30 cm and the outer part, above this radius.

BDC denotes the *Backward Drift Chamber* settled between the central tracking system and the SpaCal and consists of four double layers of 32 drift cells. Each of the layers is divided into 8 octants in the ϕ plane. It provides a precise measurement of passing charged particles, reconstructing their position with a resolution $\sigma(r) = 0.4$ mm and $\sigma(\phi) = 0.8$ mm.

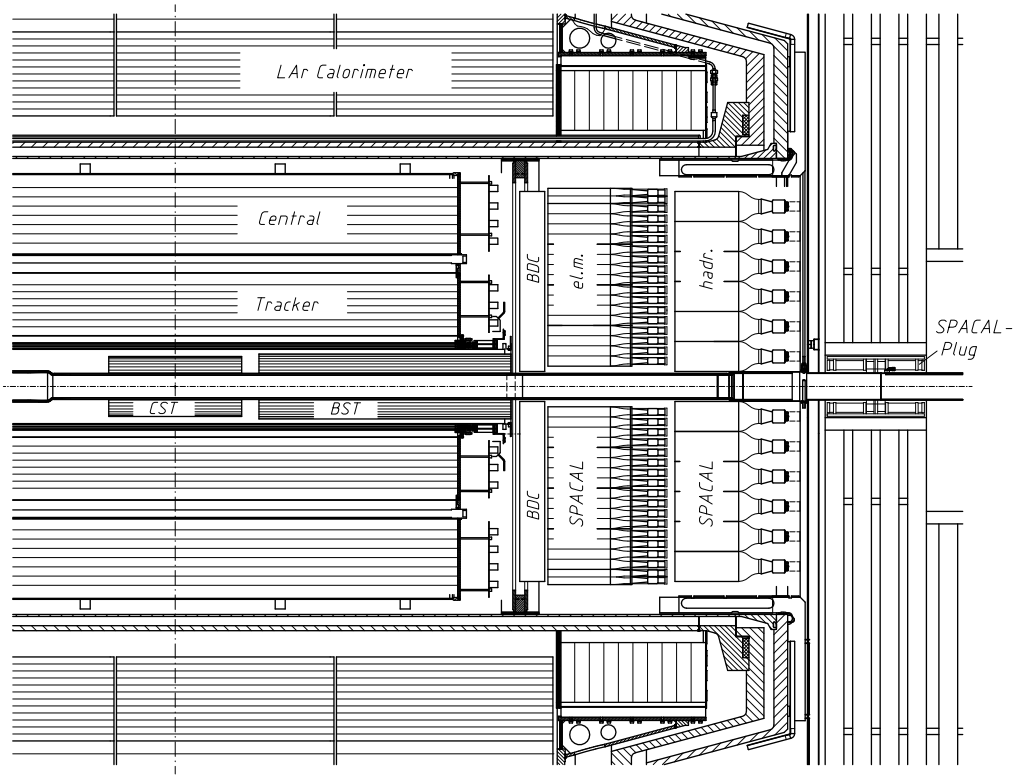

Figure 3.7: The SpaCal position in the backward region of the H1 detector.

3.2.4 The Luminosity System

The luminosity is a crucial quantity needed for any cross–section measurement. For the precise measurement of luminosity, processes with well known cross–section are used. In case of HERA, the bremsstrahlung[17] $ep \longrightarrow e\gamma p$ is used, calculable[18] in QED, where the photon and electron are scattered at very low angles. The main contribution to the background is the bremsstrahlung from the residual gas in the beam pipe, $eA \longrightarrow eA\gamma$, expected to be at 10% of the $ep \longrightarrow e\gamma p$ rate at the design luminosity and can be subtracted using data of the electron pilot bunches. Therefore, the luminosity is calculated as

$$L = \frac{R_{tot} - (I_{tot}/I_0)R_0}{\sigma_{vis}}$$

where R_{tot} is the total rate of the bremsstrahlung events, R_0 is the rate in electron pilot bunches, I_{tot} and I_0 are the corresponding beam currents and σ_{vis} is the visible part of the $ep \longrightarrow e\gamma p$ cross–section including the acceptance and trigger efficiency.

One of the main contributions to the systematic error in the luminosity measurement comes from the dependance of the system acceptance on the electron beam angle variation in the interaction region. This tilt is typically of the order of 100 μrad and is controlled by the position of the beam profile in the photon detector with the precision of 10 μrad. This correction for σ_{vis} is taken into account online. Electrons and photons are detected by two very backward electromagnetic calorimeters far in the HERA tunnel: the electron tagger ET and the photon detector PD, with their response shown in Fig. 3.8.

The Electron Tagger

The ET is located at z = –33.4 m from the interaction point. It is a Čerenkov counter with high radiation resistance assembled of thallium chloride / thallium bromide crystal cells. Each cell is read out by a photomultiplier over an optical contact. A total of 7×7 such crystals are mounted together on an area of 154×154 mm^2 having the angular acceptance of 1 *mrad*. Scattered electrons escaping through the beam pipe are deflected by focusing magnets and leave the beam tube at z = –27.3 m through an exit window and hit the tagger. This device tags the electrons scattered into the low angles $\theta_{e'} < 5$ *mrad* with respect to the beam tube and energy of $5.5 < \mathrm{E_{e'}} < 22$ GeV. This restricts the momentum transfer square Q^2 and the inelasticity y as

$$Q^2 \;<\; 0.01 \text{ GeV}^2$$
$$0.2 \;\leq\; y \;\leq\; 0.8.$$

[17] the bremsstrahlung was first approximated by H. Bethe and W. Heitler and is often called as the Bethe–Heitler process

[18] with an accuracy of 0.5%

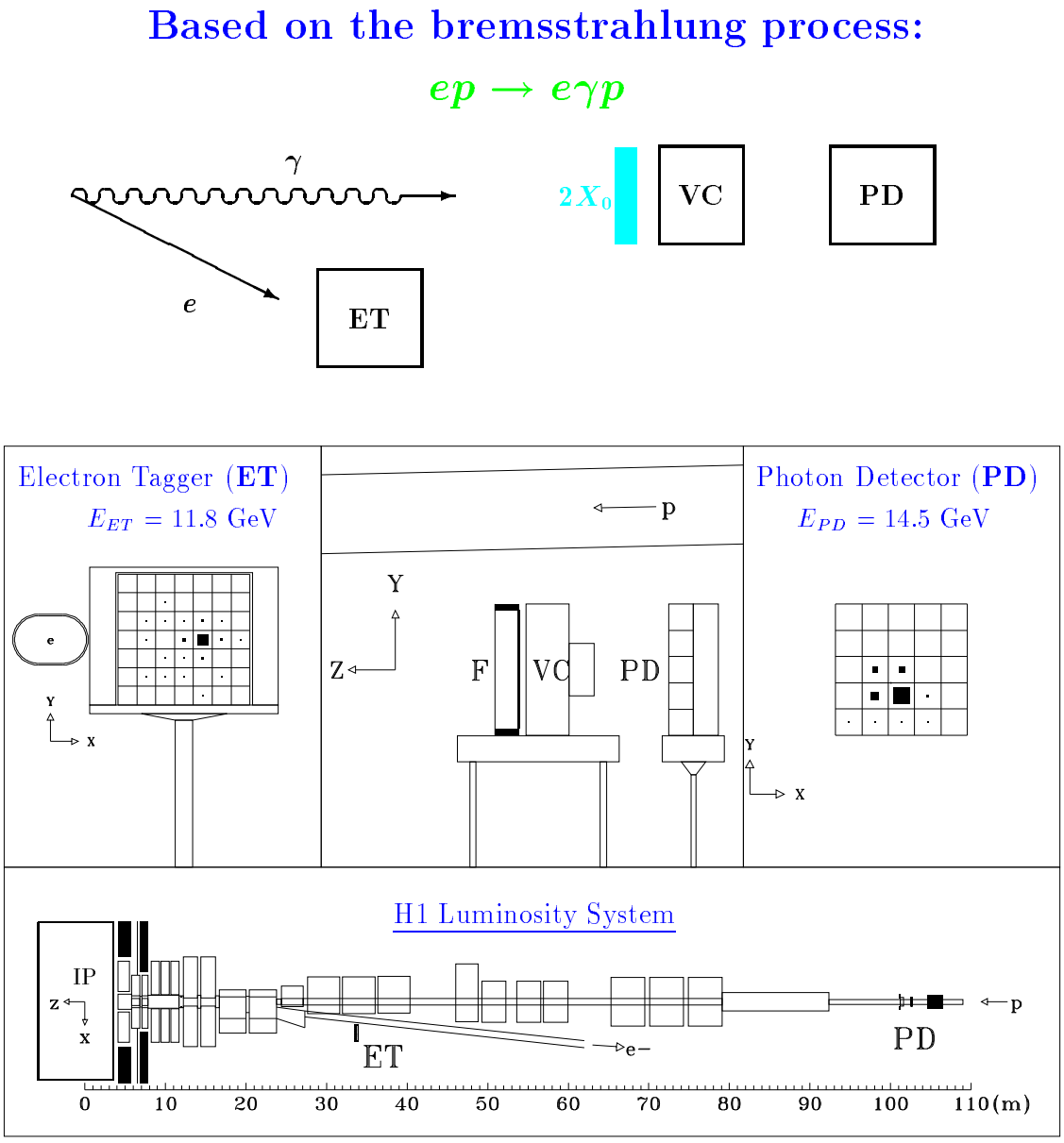

Figure 3.8: The bremsstrahlung shown above and the H1 Luminosity System response below, with the schematic view of both detectors relative to the H1 central detector.

The Electron Tagger is mounted on a movable platform and during the beam injection it is retraced to protect itself from the radiation damage.

The Photon Detector

Emitted photons emerged from the *ep* process in the central part of H1 unseen at very low angles, reaching the PD housed at the $z = -102.9$ m through an exit window at $z = -92.3$ m, where the beam pipe bends upwards. The detector is protected from the synchrotron radiation by a lead–copper filter of two radiation lengths followed by a water Čerenkov counter of one radiation length. The detector consists of 5×5 cells covering a total area of 100×100 mm^2 with an average angular acceptance of 0.5 *mrad* depending on the run vertex position and the angular beam tilt. It is equipped by moving platform protecting the detector from the radiation damage.

Determining the Luminosity

As the scattered electron and the photon from the bremsstrahlung are detected, two different methods determining the luminosity exist:

- **Coincidence method:** Both, outgoing electron and photon are detected simultaneously.
- **Photon method:** Only the energy of the photon in the PD is needed.

Online luminosity is measured by the *coincidence method* with additional condition for the sum of the scattered electron and the photon energies $E_{e'}$, E_γ to be approximately equal to the incident electron energy E_e:

$$E_\gamma + E_{e'} \simeq E_e.$$

For the smaller systematic uncertainties, the *photon method* is used offline to determine the luminosity using the formula

$$L = \frac{N^{ep}_{BH}(E_\gamma > E_{min})}{\sigma_{BH}(E_\gamma > E_{min})}$$

where $N^{ep}_{BH}(E_\gamma > E_{min})$ is the number of events with an energy of the photon E_γ larger than a minimal energy E_{min} measured by the PD. $\sigma_{BH}(E_\gamma > E_{min})$ represents the cross–section for the production of photons in that kinematic range. N^{ep}_{BH} has to be corrected for the trigger efficiencies, acceptance of the photon detector and the pile up effect when more than one bremsstrahlung per bunch crossing happens. The resulting uncertainty of the measurement is within 1.5%.

3.2.5 The Forward Proton Spectrometer

Since 1995 the H1 experiment at HERA is operating a Forward Proton Spectrometer (FPS). Scattered protons are detected in stations at 81 and 90 m behind the interaction point, extended with stations at 80 and 63 m starting to operate in 1997. In all stations the protons are detected with scintillating fiber hodoscopes. Each station consists of a moveable vacuum section, a so called *Roman Pot*[19], in which the detector elements are mounted. The detector can be brought a few milimeters close to the proton beam. During injection and acceleration the Roman Pots are retracted.

In about one quarter of the neutral and charged current deep inelastic interactions the protons remnants fragment into final states containing an energetic forward going proton. These leading protons escape through the beam pipe and are not detected in the central HERA detectors With the FPS forward scattered protons at angles in the order of *mrad* are detectable. These protons are recorded and their energy is measured.

3.2.6 The Time–of–Flight System

To distinguish between the useful events and the background particles, a ToF system is implemented to measure the time of passing particles. It consists of a set of scintillators mounted perpendicularly to the beam pipe: FToF at $z = +7$ m, PToF at $z = +5.3$ m, VLQToF at $z = -3.2$ m and the veto walls at $z = -6.5$ m and $z = -8.1$ m. Also, the SpaCal is used for timing, provided by the co–called SToF counters. All these devices (see Fig. 3.9) measure the time of flight with a respect to the bunch crossing time set by HERA and provide some of the trigger elements for the trigger system.

The complete time window is 96 ns wide, according to the time crossing interval t_{cross}. This window is split into the *background time window* BG, *interaction time window* IA and *global time window* GL derived from the HERA clock to define three trigger elements `ToF_BG`, `ToF_IA` and `ToF_GL`. The GL is the same for all the parts and covers the period of the 96 ns cycle. The BG and IA are specific for each part of ToF according to its position in the H1 detector. Anyway, the background window covers the time from HERA clock start (0 ns) and lasts for 25 ns. Here opens the interaction window and close at 39 ns [21]. Every of the ToF parts has to check the different attributes according to its position (see Fig. 3.10).

[19]These moveable vacuum sections were first used at the Intersecting Storage Rings (ISR) at CERN by a collaboration, in which a group from the Institutio Superiore di Sanità in Rome played an important role

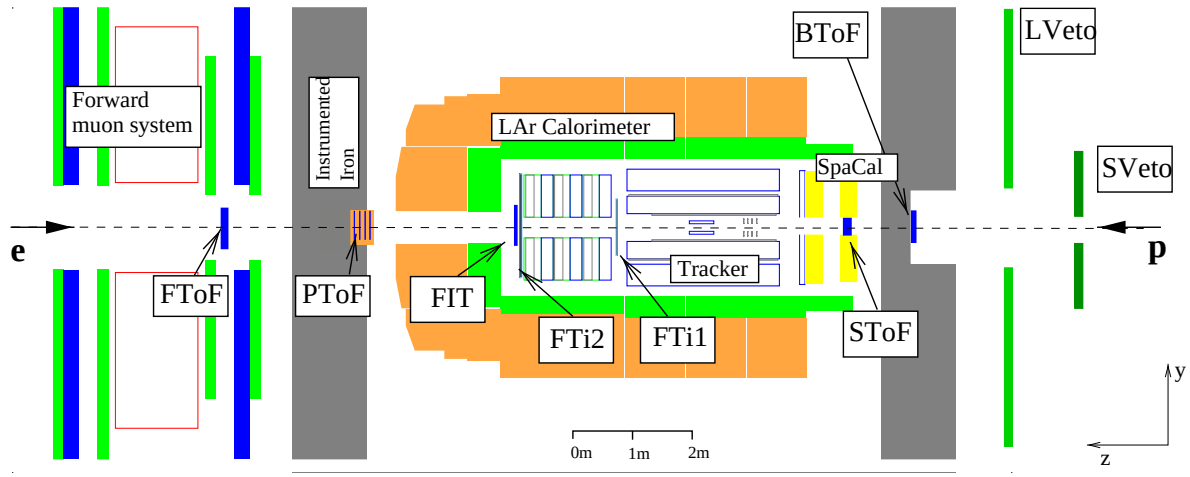

Figure 3.9: The H1 Time–of–Flight system, including all the devices installed after the HERA–II upgrade, when additional ToF systems was installed, namely the FTi1 in between the central and the forward tracker, operating together with the FTi2, a scintillator system between the forward tracker and the inner forward section of the LAr calorimeter.

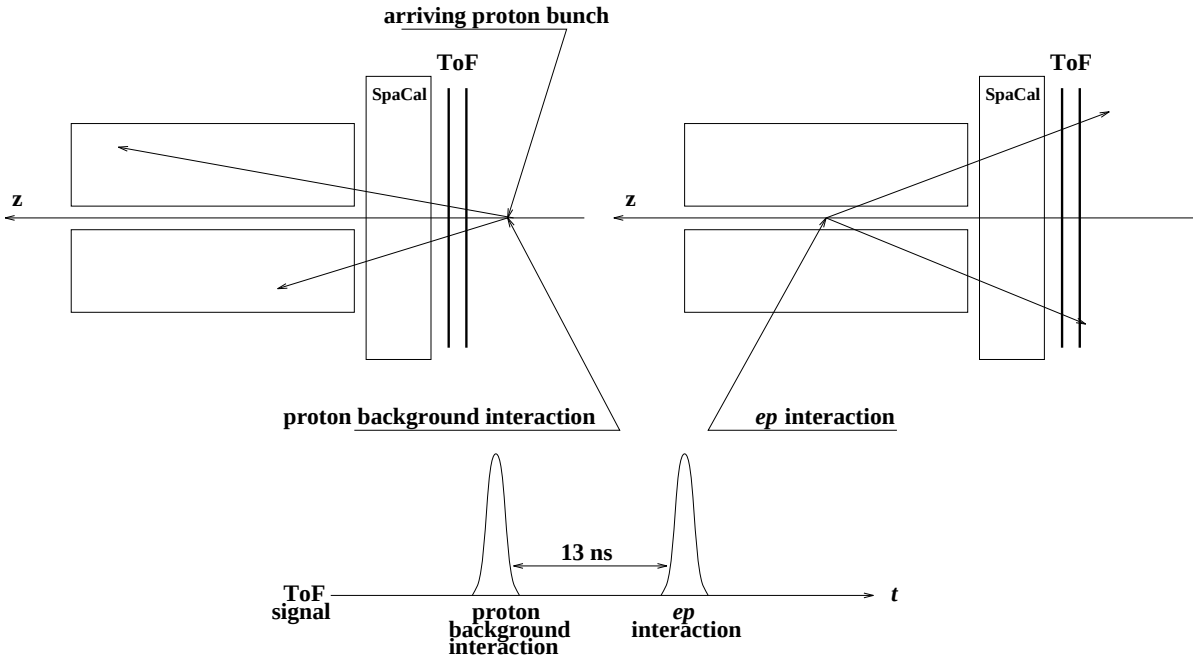

Figure 3.10: The schematic view of the time window division. Most of the non-*ep* background can be separated using the time of main *ep* reaction.

FToF

The Forward ToF installed between the forward muon system, consists of two scintillator layers with two multipliers and is used to monitor the substructure of the proton beam.

PToF

8 scintillators are mounted inside the Plug calorimeter in the forward direction.

- **BG:** Interval of the time when the electron from the beam passes the Plug calorimeter. The time window opens by the HERA clock and lasts until the interaction window. Background raises mainly due to the synchrotron radiation.
- **IA:** Particles from the nominal *ep* interaction reach the Plug.
- **GL:** Covers the full 96 ns cycle.

VLQToF

The backward ToF, VLQToF consists of two circle scintillator tiles with an outer radius of 250 mm and the inner one of 65 mm.

- **BG:** Interval of the time in witch VLQToF detects the proton beam induced background events, like the halo muons[20] or cosmic rays, all *before* the *ep* interaction.
- **IA:** Particles originating from the nominal *ep* interaction reach the VLQToF.
- **GL:** Starts after IA and lasts until the end of the interaction time window.

3.2.7 The Trigger System

Background events make the huge amount of unwanted events[21] and the trigger task is to separate this, physically non-interesting data from the ones of physics interest. Even at the rate of 10^7 bunch crossings per second, the trigger rate is of the order of 10^4 Hz. Since it is technically impossible so far to read the whole detector information per bunch crossing, the multilevel trigger system has been developed to gradually lower the rate of data needed to be kept.

Presently, the L1, L2, L4 and L5 levels are fully operational (L3 is not yet operating) as seen in Fig. 3.11.

[20] produced after proton hits the wall of the beam pipe or a gas atom

[21] concerning the designed luminosity $\mathcal{L} = 1.5 \times 10^{31}$ cm^{-2}s^{-1}, the background rate is about 1000 times higher than the rate of deep inelastic scattering reactions

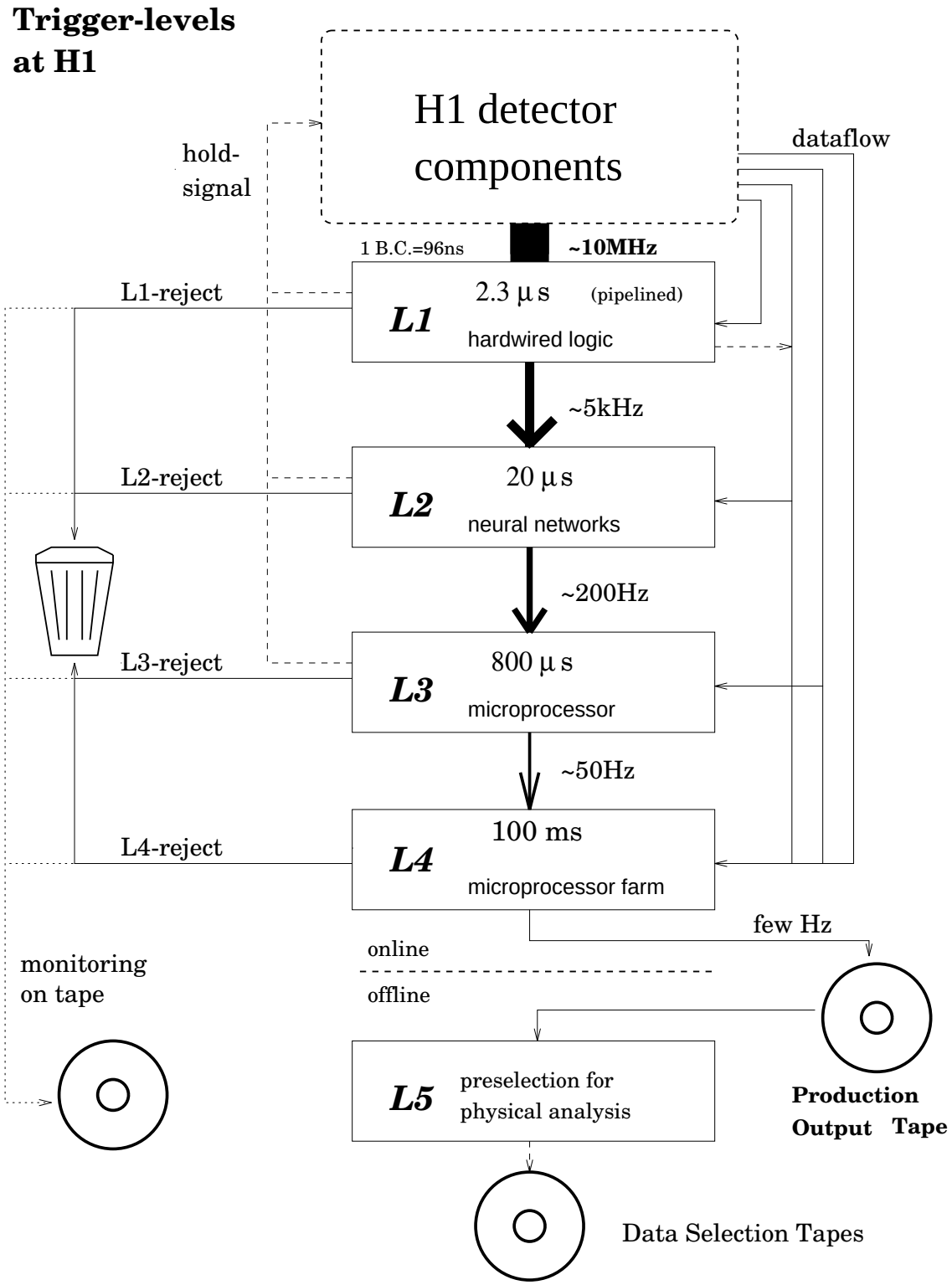

Figure 3.11: The L1 - L5 H1 trigger levels together with their output rates.

- **Level 1**
  The L1 trigger is a fully hardwired trigger logic and thus dead–time free in the sence that no good event is rejected. The logic is built on the 256 trigger elements monitoring the whole H1 detector. From these elements, 128 subtriggers $s0 - s127$ are constructed via the logical conjunctions. The L1 provides a fast decision within 2.3 μs. Each event is marked by a 128 bit pattern. Each such bit represents a logical status of one of the subtriggers; if this subtrigger fires,[22] a corresponding bit is set to *1* — a logical *true*. If at least one of these subtriggers fired, the data are passed to L2 trigger systems. Besides that, frequent *raw* subtriggers can be *downscaled*, such that only every n^{th} event satisfying appropriate conditions is marked as the *actual* subtrigger, allowing more rare events to be kept.

- **Level 2**
  The L2 trigger consists of two subsystems — a *topological trigger* and *neural networks*. Both of them use the combinations of signals from the various detectors. The topological trigger works with the pattern recognition in the detectors and is programmable using the `assembler` instructions. The data for trained neural networks are used as input for fast processors with these neurals implemented. The decision time of the L2 trigger is 20 μs — in this time the detector is unable to take events. After positive L2, the data taking stops and the event information is readout completely for the L4, resulting in a dead–time of 1.5 ms.

- **Level 3**
  Not operating, preset to *1*.

- **Level 4**
  Both, L4 and L5 are the software triggers — here starts the reconstruction from the electronics into physics information. L4 consists of a farm of processors with a processing time of 100 ms per event. The farm code is organized in such a way, that a decision is reached as soon as possible. The general scheme of the filter algorithm is the following [3]:

  1. ACCEPT monitor triggers: accept events with at least one monitor trigger as a final subtrigger FST[23]
  2. REJECT beam–gas/beam–wall events: mainly by cuts on the z coordinate of the event vertex
  3. RESET trigger noise: reset the FST bits if the trigger verification using the corresponding reconstructed quantities failed — the event is then rejected if there is no FST bit left that survives the verification.

[22] the corresponding parts of a detector succeeded in all subtrigger conditions
[23] *a **F**inal **S**ub**T**rigger* is an actual L1 subtrigger validated by at least one of associated L2 machines

4. ACCEPT hard scale physics: accept event if at least one hard scale defined by Lorentz invariant quantities is presented above some cuts.
5. ACCEPT exclusive final states: based on special cuts or sophisticated finders.
6. DOWNSCALE soft physics: events are downscaled with respect to Q^2 (the downscaling factor becomes larger as Q^2 decreases).

Once the decision is reached, the remaining part of the code is not executed, in order to speed up the flow and the accepted event is written on the tape. Anyway, 1% of the rejected events (step 2 and 3) is still written on the L4–reject tapes – these events are expected to be pure background by definition and are not supposed to be considered in any analysis. This fraction is used only to cross–check that no good events were rejected.

- **Level 5**
  Events are fully reconstructed here and classified according to the different types of underlying physics, e.g. diffraction is put to *class 13*. The detailed linking of charged particle track segments and energy clusters from different subdetectors is made and the fully reconstructed physics subtriggers are subjected to further cuts, rejecting background events that came through all the previous levels 1 – 4.

Chapter 4

Event Reconstruction, Selection and Monte Carlo Simulation

The aim of this analysis is to measure the cross–section of diffractive photon scattering at high t. One of the main ingredients for this measurement is the number of the events being observed during a certain period. Since among these events also many others were produced and detected at the H1 detector, the process of selection candidates of diffractive photoproduction of photon at high t is described by the chain of cuts applied to all observed events in a certain period.

4.1 The Detector Correction Treatment

In order to understand what really is a detector output and what information can be obtained from it to analyze, it is important to interpret the detector properties in form of uncertainties (i.e. the detector resolution) in reproducing the values of the particle quantities.

In the following, the explanation between the physical and the detector level of values and the importance of introducing the simulated physical events of various processes is given.

4.1.1 Migration

A picture describing the understanding of the high energy ep scattering and the state from which it could be detected, is shown in Fig. 4.1. In the framework of the parton model, in case of a DIS event partons are produced (including possible gluon radiation called parton shower), carrying the colour quantum numbers. These partons stay intact until the strong force, taking place in the distance longer than 1 fm, combines them

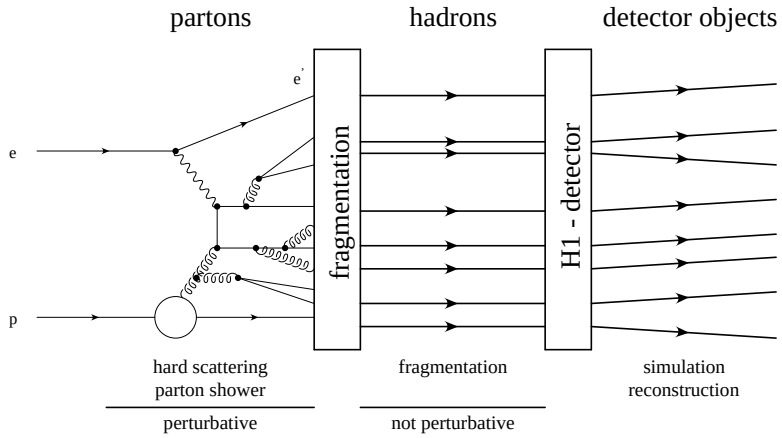

Figure 4.1: The physical process of *ep* reaction is shown, displaying the evolution from partons to final particles and their detection by detectors with non–zero resolutions, leading to the shifted values given as an output (represented here as shifted lines).

into hadrons. After this hadronization (or fragmentation) process, the stable hadrons together with other final particles are detected leaving tracks and energy signals while in the detector acceptance.

Due to the statistical properties of the quantum physics, the cross–section has to be extracted by the statistical means too. A large number of particle collisions resulting from the similar initial conditions is observed. That means that for every variable a *spectrum* is obtained. Due to the detector uncertainties, the values obtained by detector differ more or less from their original values. For this reason, two stages of the particle information can be recognized:

- **Physical Level**,
  the level of true values of variables describing the corresponding particle, which are not deformed by the detector uncertainties;

- **Detector Level**,
  the level of deformed variables as an output information of the detectors; this level is the only one to be confront with during the analysis of the non–simulated data.

The absolute deviation between these levels is called *migration* (see Fig. 4.2). Here the detector spectrum X^{det} of a variable X is shown. This variable defines the phase space of the measurement by the cut represented by a vertical dashed line. The same cut is applied at both, the detector level and the physical level as seen. The filled area indicates the events inside the phase space region at the physical level (X^{phy}). The dashed

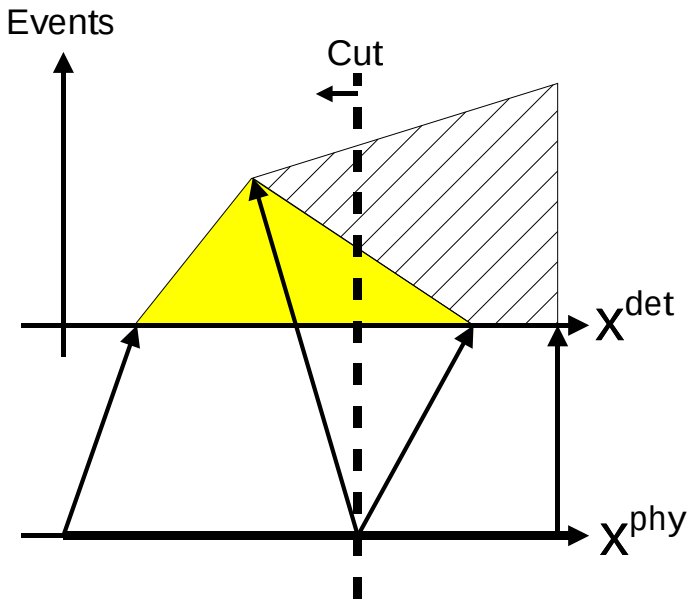

Figure 4.2: The migration effect: the smearing of values from physical level (X^{phy}) to the detector level (X^{det}).

area indicates events outside this region at the physical level. Some of the events inside the physical level are lost because of migrations (filled area to the right of the cut line) and some of the events migrates into the detector sample from outside the physical level (dashed area at the left side of the cut).

To obtain the physical values of all variables we need to understand the detector properties and find the difference of these two levels.

4.1.2 Detector Simulation

Migrations can be studied using the events simulated by the *Monte Carlo* method[1], passed through the fully simulated detector response. This simulation provides a detector response for a given quantity.

Firstly, the event generator provides a list of particles, each having its certain quantum numbers and a momentum 4–vector. To obtain the detector response to such an event, the interaction between particles and the detector parts must be evaluated. For

[1] a Monte Carlo method uses a random number in the computational chain to provide the values of particle quantities

the H1 detector, the simulation program H1SIM based on GEANT exists. Each of the particles is treated individually making its way through the detector. The probability of reaction with the detector material is calculated using tabulated cross–sections. Some of the reactions can result into the secondary particles, which are treated the same way and traced through the detector. The final detector response is obtained in the form of electronic signals. These signals are subjected into the same analysis chain as the real data. After this process is done, the Monte Carlo simulated events can be compared to real data.

4.1.3 Process Simulation

HERWIG

The HERWIG 6.1 Monte Carlo event generator[2] was used to correct the data for the detector acceptance, migration effects and to make model comparisons. Within HERWIG the diffractive photon scattering at high t sub–process has been implemented by the authors of [20]. The theoretical calculations of this process has been done to the leading logarithmic approximation (LLA) of BFKL including contributions from both real and virtual incoming photons [16, 17].

The photon–quark cross–section $\sigma_{\gamma q}$ differential in t and amplitude A are linked through the relation

$$\frac{\mathrm{d}\sigma_{\gamma q}}{\mathrm{d}t} \approx \frac{|A_{++}|^2}{16\pi s_{\gamma q}^2} \ , \tag{4.1}$$

ignoring a small contribution that flips the helicity of the incoming photon (A_{+-}). The $s_{\gamma q}$ stands for the photon–quark center–of–mass energy. The photon–proton cross–section is obtained after multiplying by the parton distribution functions,

$$\frac{\mathrm{d}\sigma_{\gamma p}}{\mathrm{d}x\mathrm{d}t} = \left[\frac{81}{16} g(x,\mu) + \Sigma(x,\mu)\right] \frac{\mathrm{d}\sigma_{\gamma q}}{\mathrm{d}t} \ , \tag{4.2}$$

where $\Sigma(x,\mu) = \sum_q [q(x,\mu) + \overline{q}(x,\mu)]$ and the factorization scale is $\mu = p_T^\gamma$. This result is implemented into HERWIG event generator to aid the experimental measurement of the process. In the BFKL approach, at LLA, the strong coupling constant α_s is a fixed parameter leading into two independent free parameters in the calculation,

- the value of α_s in the pre–factor of the cross–section
- and the value of α_s in the energy dependence (pomeron intercept) $1 + \omega_0$, where

$$\omega_0 = \frac{3\alpha_s}{\pi} 4\ln 2 \ . \tag{4.3}$$

[2] general purpose generator for ***H**adron **E**mission **R**eactions **W**ith **I**nterfering **G**luons* [25]; based on matrix elements, parton showers and including a cluster model for hadronization.

These two values have been chosen by [1] to be equal and are referred to as $\overline{\alpha_s}$. The generated luminosity of the Monte Carlo events is 212 pb^{-1}.

To estimate the background events, generators like the PHOJET and the DIFFVM were used.

PHOJET

The PHOJET event generator [23] is used to generate a multiparticle production in high energy hadron–hadron, photon–hadron and photon–photon interactions. The generator includes the photon flux simulation for photon–hadron and photon–photon processes in lepton–lepton, lepton–hadron, and heavy ion–heavy ion collisions. The event generator is formulated as a two–component model (soft and hard component) in order to combine the soft processes with the predictive power of perturbative QCD. Hard scattering processes are simulated using lowest–order perturbative QCD. Initial state and final state parton showers are generated in leading–log approximation.

DIFFVM

The MC program DIFFVM [24] was designed to simulate the process of diffractive vector meson production $ep \longrightarrow eVY$, where V is the produced vector meson. The predictions of this generator are based on the *Vector Meson Dominance Model* (VDM) and the Regge theory. The program generates the vectors of the final state particles including the decay product of the produced vector meson and detailed simulation of the diffractive dissociation of the proton.

4.2 Reconstruction of Kinematic Variables

As the kinematic quantities can not be measured directly, their reconstruction must be made. Different reconstruction methods give more precise results for the different kinematic regions. The kinematics of the event can be determined from measurements on the electron only, on the final hadronic state only or a mixture of these. The preferred method depends on the current kinematic region. (see Fig. 4.3).

- **Electron method**
  The only inputs for this reconstruction method are the energies of the electron beam E_e and the scattered electron $E_{e'}$ together with the scattering angle $\theta_{e'}$ measured with respect to the proton beam direction. The kinematic variables are given by

$$y_e = 1 - \frac{E_{e'}}{E_e} sin^2 \frac{\theta_{e'}}{2} \; ; \tag{4.4}$$

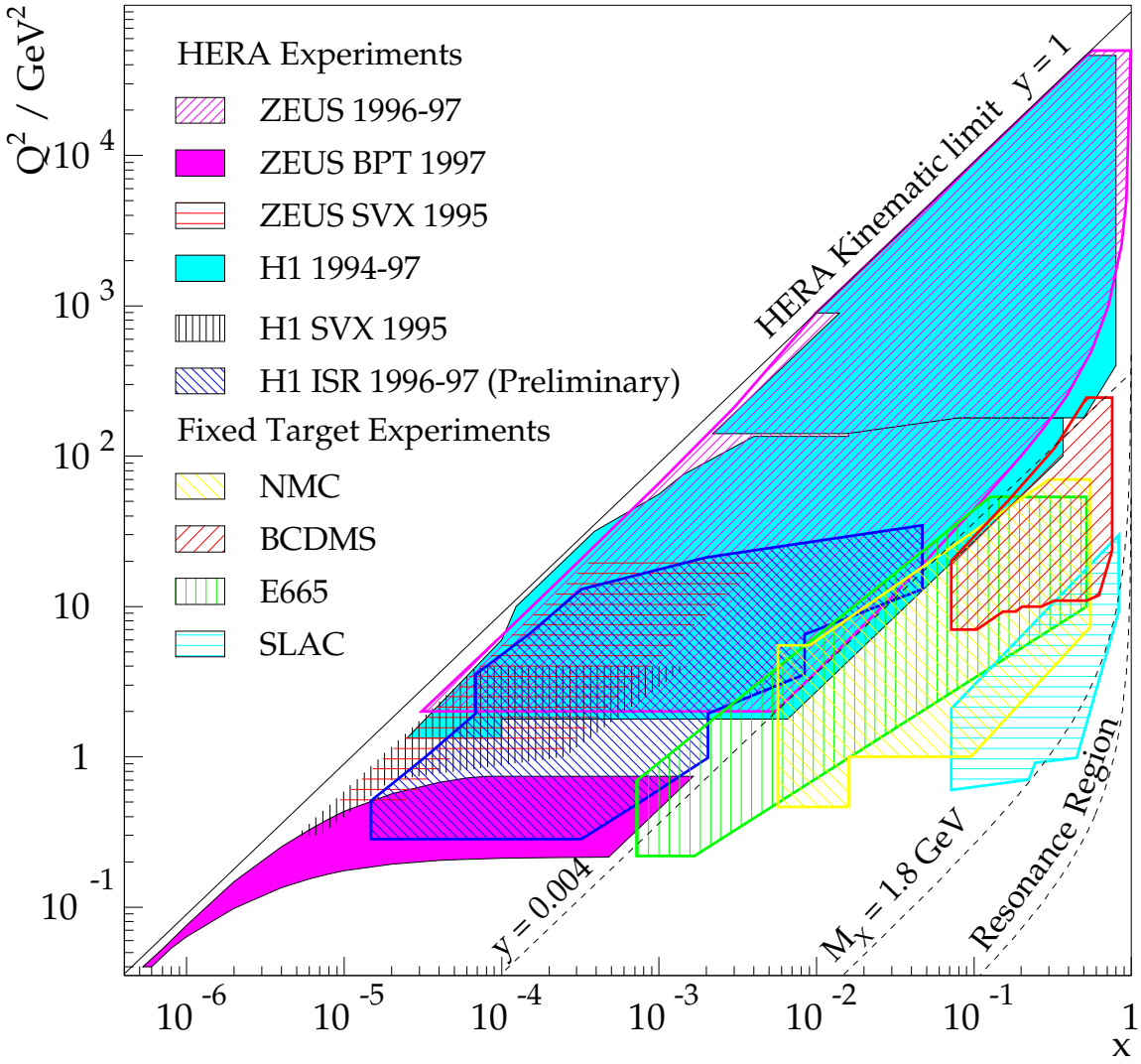

Figure 4.3: Coverage of the (x, Q^2) plane by the DIS experiments.

$$Q_e^2 = 4E_e E_{e'} cos^2 \frac{\theta_{e'}}{2} \; ; \tag{4.5}$$

$$W_e^2 = y_e s - Q_e^2 \; ; \tag{4.6}$$

$$x_e = \frac{Q_e^2}{s y_e} \; . \tag{4.7}$$

At high inelasticity y, electron method gives a good resolution, but it degrades with y decreasing.

- **Hadron method**
  Known as the *Jacquet–Blondel* method, it uses the hadronic energy and the three–momentum components of final state hadrons and is therefore completely independent from the electron method.

- **Double Angle method**
  The kinematic variables are determined using the angles of the final state electron and the hadronic final state (the X system) without introducing any energies of the final particles.

Among the above methods, the *Mixed method* and the Σ *Method* were developed to maximize the applicable kinematic region. The description of these two methods and comparison with those mentioned above can be found in [18].

In the present analysis, to reconstruct the kinematic variables, the electron method was used. Also, the diffractive kinematic variables described in section 2.2.2 are to be reconstructed. In photoproduction, the photon emerged from the electron line has a low virtuality $Q^2 < 0.01$ GeV^2 and can be in many cases neglected. Also the proton rest mass is relatively small ($M_p^2 \ll W^2$) and therefore neglected. Hence, the equation (2.30) become simplified as

$$x_{I\!P} = \frac{M_X^2 - t}{W^2} \; . \tag{4.8}$$

Keeping the same assumption of low Q^2, the W^2 can be approximated by

$$W^2 = 4E_\gamma^{inc} E_p \; , \tag{4.9}$$

where the E_γ^{inc} stands for the energy of the incident photon and E_p is the energy of the incoming proton beam. The momentum transfer t at the proton vertex is considered to be

$$t = (q - p_X)^2 \simeq M_X^2 - 2q \cdot p_X = M_X^2 - 2E_\gamma^{inc} \sum_{j \in X} (E_j + p_{j_z}) \; , \tag{4.10}$$

if assuming incident photon to have only z component of its momentum non–zero. The E_j is the energy of the particle j from the X system and the p_{j_z} is its z component of three–momentum $\mathbf{p}_\mathrm{j}$. Since the final X system consists from nothing but the single real photon, sum in above equation changes to

$$\sum_{j \in X} (E_j + p_{j_z}) = E_\gamma + p_{\gamma_z} \ . \tag{4.11}$$

Further, the $M_X = m_\gamma = 0$ and the diffractive variable $x_{I\!P}$ is then reconstructed as

$$x_{I\!P} \simeq \frac{E_\gamma + p_{\gamma_z}}{2E_p} \ . \tag{4.12}$$

Turning to the $y_{I\!P}$, its reconstruction is based on the same consideration as was for the $x_{I\!P}$. According to equation (2.31) and considering $t = (p - p_Y)^2$, the energy transfer $y_{I\!P}$ is reconstructed as

$$y_{I\!P} = \frac{\sum_{j \in Y} (E_j - p_{j_z})}{2E_\gamma^{inc}} \ , \tag{4.13}$$

where the E_j and p_{j_z} are the energy and the z component of three–momentum $\mathbf{p}_\mathrm{j}$ of the particle j of the proton dissociation system Y.

4.3 Topology of the Event

The final state of the diffractive photoproduction of high t photons consists of the final high p_T photon, scattered electron and the proton dissociation system Y. An example of such an event detected by the system of H1 subdetectors is depicted in Fig. 4.4.

- **Electron**
  In photoproduction regime the only way to measure the scattered electron is to detect it in an Electron Tagger. The Electron Tagger at 33 m is used in this analysis. This restricts as desired the $Q^2 < 0.01$ GeV^2, but also the $175 < W < 247$ GeV.

- **Photon**
  In such a W range and at large t ($|t| > 4$ GeV^2), the photon will be scattered in the direction of the SpaCal calorimeter.

- **Proton dissociation system**
  The hadronic final state particles of the dissociated proton are spread over the low polar angles θ in the forward direction and detected either by the LAr calorimeter or the Plug or leave the H1 detector unseen.

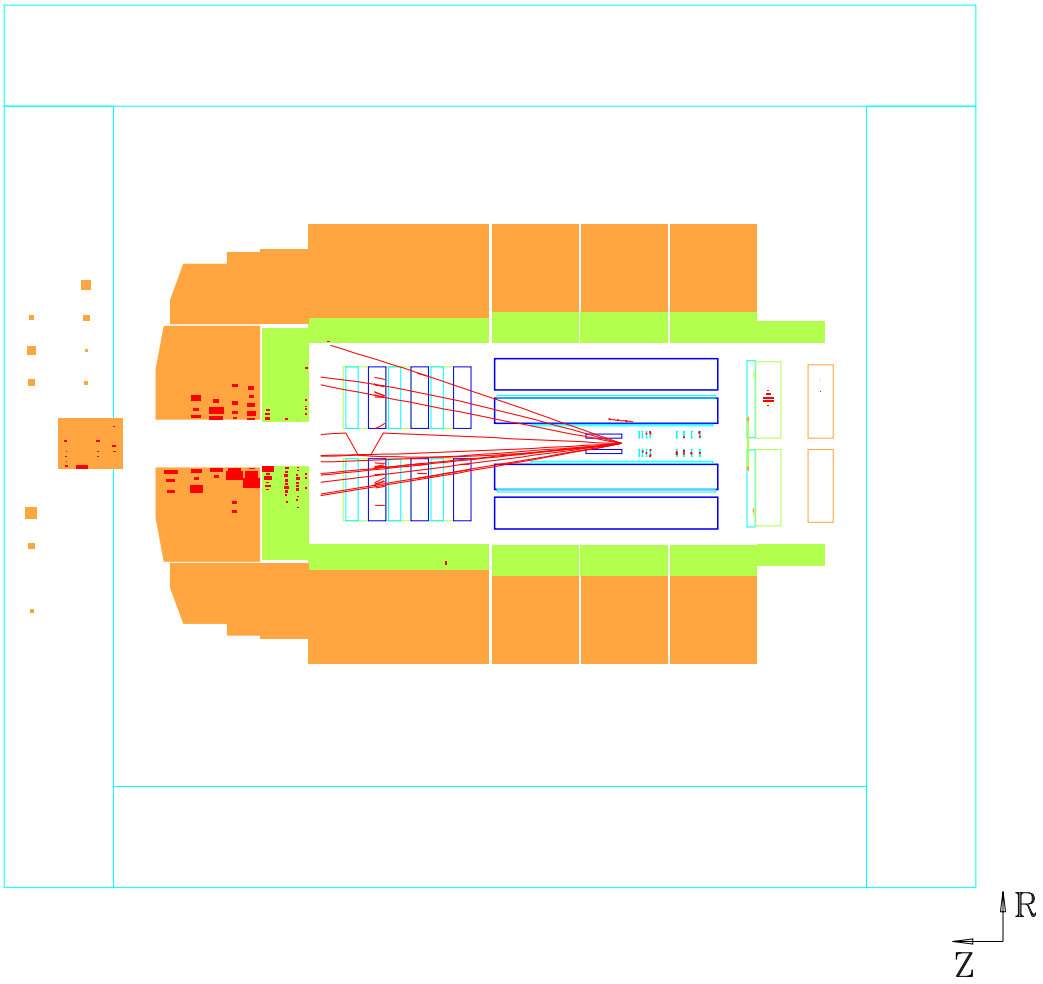

Figure 4.4: The display of the main detector for a data event candidate of diffractive photoproduction of photon with high transverse momentum p_T.

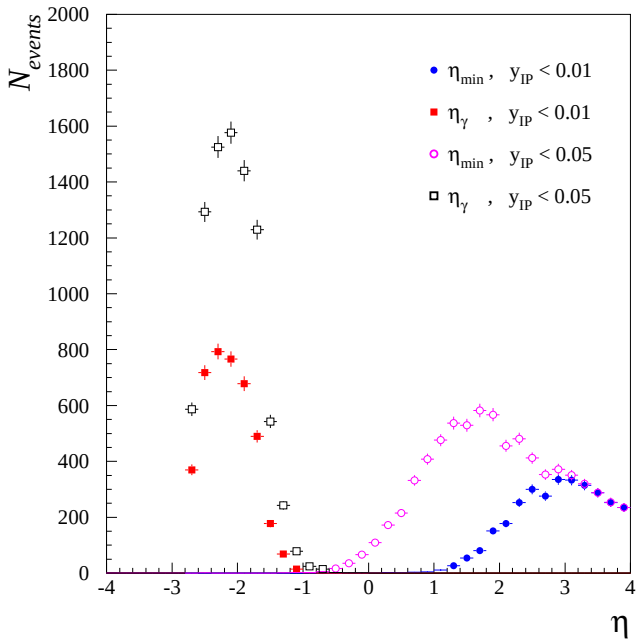

Figure 4.5: The rapidities of the final photon and the backward edge of the proton dissociation system Y for two different $y_{I\!P}$ cuts. (taken from [20])

4.4 Diffractive Selection

The diffractive event is characterized by the large rapidity gap $\Delta\eta$ (see section 2.2.2) and is bound with the $y_{I\!P}$ variable as [20]

$$y_{I\!P} \approx \frac{(p_T^{\gamma})^2}{xW^2} \approx \mathrm{e}^{-\Delta\eta} \ , \tag{4.14}$$

where $(p_T^{\gamma})^2 = p_{\gamma_x}^2 + p_{\gamma_y}^2$ is the transverse momentum of the final photon. The $y_{I\!P}$ cut is set [1] to

$$y_{I\!P} < 0.018 \ , \tag{4.15}$$

ensuring the low mass M_Y of the proton remnants and, therefore, a large rapidity gap between the photon and the Y system. The effect of varying the $y_{I\!P}$ cut on the size of rapidity gap is shown in Fig. 4.5. As can be seen, the allowed rapidity gaps between the final photon and the most backward hadronic final state of the system Y are smaller with increasing the $y_{I\!P}$. The rapidity gap was chosen to be greater than two units,

$$\Delta\eta > 2 \ . \tag{4.16}$$

4.5 Event Selection

4.5.1 Scattered Electron Selection

According to equation (2.4), the inelasticity y can be in photoproduction rewritten as

$$y = \frac{E_\gamma^{inc}}{E_e} \ , \tag{4.17}$$

where E_γ^{inc} is the energy of the mediated boson – the photon and E_e is the energy of the electron beam. As $E_\gamma^{inc} = E_e - E_{e'}$, at low scattering angles $\theta_{e'}$ of the electron the elasticity can be computed according to equation (4.4) using only the initial and final energies of the electron

$$y = 1 - \frac{E_{e'}}{E_e} \ . \tag{4.18}$$

The photon–proton centre–of–mass energy W is reconstructed as

$$W^2 = ys \ . \tag{4.19}$$

Electron Tagger

The detection of the scattered electron near the boundaries of the electron tagger raise a probability that part of the electron shower is not contained within the area of tagger. This would produce false energy estimation, thus for this reason, the general cut on the local x coordinate in the electron tagger is applied

$$|x_{tag}| < 6.5 \text{ cm} \ , \tag{4.20}$$

rejecting events having the energy deposit at more than 1.5 cm of the horizontal edges of the detector.

For the smaller energies of the electron, background raises mainly due to the electron beam–gas interactions [21], while at large energies the tagger acceptance becomes too small (see Fig. 4.6). Thus, the cut on the inelasticity y is applied holding it between

$$0.3 < y < 0.6 \ , \tag{4.21}$$

restricting the photon–proton centre–of–mass energy W to $175 < W < 247$ GeV.

Photon Detector

However, the cut to electron tagger alone doesn't exclude fake from the bremsstrahlug event $ep \longrightarrow e\gamma p$, since the electron from bremsstrahlung is also tagged by the ET

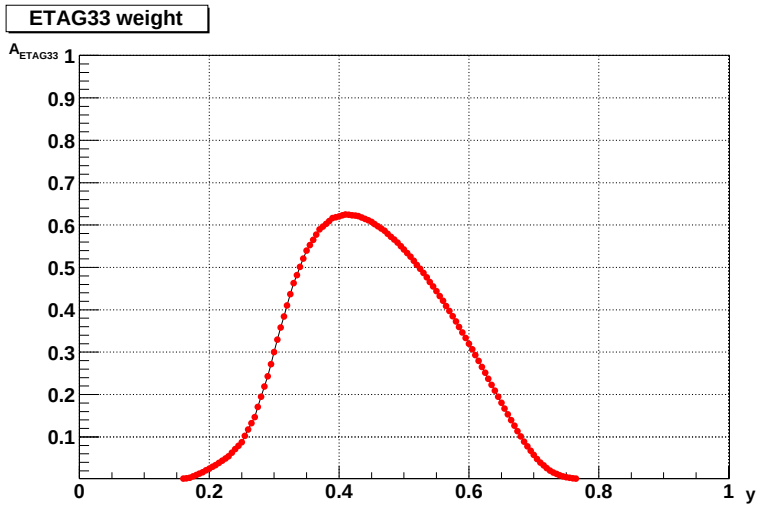

Figure 4.6: The run–dependent acceptance of the 33 m electron tagger A_{ETAG33} shown here as an average of the values of 1999/2000 run period and as a function of inelasticity y.

(see section 3.2.4). Therefore, the cut to photon detector is made, requiring no energy deposit E_{PD} above the energy of 2 GeV,

$$E_{PD} < 2 \text{ GeV} . \tag{4.22}$$

This ensures no bremsstrahlung events to be taken.

4.5.2 Final State Photon Selection

The final state photon has to have a high transverse momentum p_T^γ corresponding to high momentum transfer squared $|t|$ ensuring the presence of hard scale and allowing the results of perturbative QCD in the theoretical calculations of the final cross–section. The p_T^γ cut is then

$$p_T^\gamma > 2 \text{ GeV} , \tag{4.23}$$

setting the condition for momentum transfer t to $|t| > 4$ GeV according to equation (2.32), neglecting the four momentum transfer Q^2 of the incident photon.

Such a high transverse momentum allows photon to be detected by the SpaCal and not passing away through the beam pipe. Thus some selection must be made to isolate the photon and to ensure that no other particles are present within the event in the SpaCal.

The Electromagnetic SpaCal

The photon is detected within the electromagnetic part of the SpaCal and identified using a SpaCal *electron finder*. Based on the event topology, the only electromagnetic particle expected to be detected in the main H1 detector is the final high-p_T photon. This implies the fundamental cut on the number of electromagnetic particle candidates registered by the H1 main subdetectors[3] to 1,

$$N_{em}^{H1} = 1 \ . \tag{4.24}$$

This requirement relays on the electromagnetic shape of the cluster in the H1OO code (the transverse radius $R_{clus} < 4$ cm, energy $E_{clus} > 4$ GeV). A condition for a small cluster radius separates well the electromagnetic shower from that of the hadronic origin, since the hadronic showers have generally a larger transverse spread, resulting into larger cluster radii.

For the cluster to be fully contained within the SpaCal, the angular cut on the photon candidate must be made, restricting it to polar angles of

$$153 < \theta_\gamma < 176^\circ \ . \tag{4.25}$$

The energy of the photon is also forced under cut,

$$E_\gamma > 8 \text{ GeV} \ . \tag{4.26}$$

No additional energy deposits above threshold are tolerated, since the photon is to be the alone particle read by the SpaCal. The total energy in the SpaCal except that of the photon is only allowed to be less than 2 GeV

$$E_{spacal}^{tot} < 2 \text{ GeV} \tag{4.27}$$

and the energy of the most energetic cluster E_{clus}^{max} apart from the photon should reach no more than the value of the noise threshold,

$$E_{clus}^{max} < 0.2 \text{ GeV} \ . \tag{4.28}$$

The SpaCal cell efficiencies vary due to dead or inefficient cells, trigger channels or varying high voltage conditions. Therefore, these inefficient regions are to be rejected. The regions of the SpaCal with low efficiencies are determined from the 1999 period [22] and are these:

- $x \in$ (–12.5, –8.5) cm $\wedge$ $y \in$ (–4.5, 4.5) cm;

[3] this excludes the electron tagger

- $x \in$ (–12.5, –8.5) cm $\wedge$ $y \in$ (–8.5, 4.0) cm;
- $x \in$ (–53.0, –40.0) cm $\wedge$ $y \in$ (–24.5, –20.0) cm;
- $x \in$ (–57.0, –44.0) cm $\wedge$ $y \in$ (–29.0, –24.0) cm;
- $x \in$ (–8.5, –4.0) cm $\wedge$ $y \in$ (–12.5, –8.0) cm;
- $x \in$ (8.0, 12.5) cm $\wedge$ $y \in$ (–4.5, 4.5) cm;
- $x \in$ (–8.5, –4.0) cm $\wedge$ $y \in$ (–8.5, 4.0) cm.

These fiducial cuts are applied for both the real H1 data and the Monte Carlo generated events over the full periods to maintain the same conditions.

The Hadronic SpaCal

This part of the SpaCal should show no activity for the lack of the hadronic final state particles in backward direction (the cut on $\Delta\eta$). Thus the hadronic part of the SpaCal beyond the photon cluster within a radius of 17.5 cm should not present any activity above the energy noise threshold, ensuring that the photon cluster is electromagnetic in origin and not a penetrating hadronic shower. The corresponding cut is then

$$E^{\gamma}_{had} < 0.5 \text{ GeV} . \tag{4.29}$$

CJC and BST

Further, to ensure that the detected electromagnetic particle is photon and not a charged particle, the results from the trackers as the CJC and the BST are considered. Tracks from the event vertex as well as those not associated with event vertex are extrapolated to the area of the SpaCal cluster.

The electromagnetic cluster has to have *no tracks* assigned to it, within the distance of 12 cm. When the particle is so close to beam pipe that no more in CJC angular acceptance, the BST is required to show *no validation* of a possible tracks.

4.6 Further Background Estimate

The z Vertex Distribution

The event sample could be contamined with the beam induced background. This is due to the fact that together with the electron and proton beam, also some part of the background events pass the ToF device during the opened interaction window.

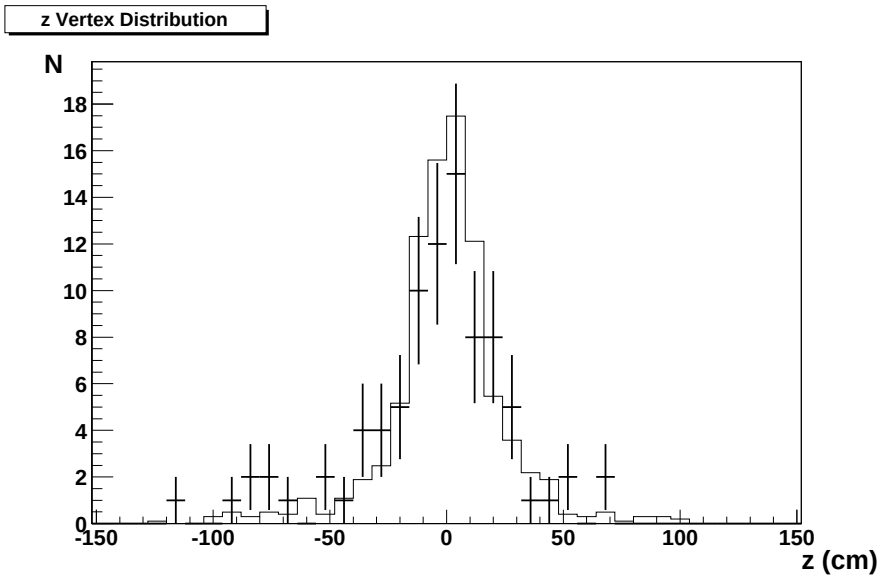

Figure 4.7: The z vertex distribution of the full event sample. All the cuts displayed in Tab. 4.3 are applied. The data (crosses) are compared to HERWIG data sample. The HERWIG prediction is normalized to the data. The distribution is well described except for the outer edges.

However, since the primary vertex position is reconstructed from the tracks of the final state particles, some difficulties arise concerning the photoproduction. As the X system is substituted by the photon alone, having no track left in the trackers and the scattered electron passes the central H1 unseen tagged by electron tagger, only the final Y system is left for the primary vertex to be reconstructed by. Furthermore, as the proton remnants could spread over very small angles θ with respect to the beam (the z axis), they may be not detected neither by the trackers (FTD, CTD) nor by the forward calorimeters.

The Fig. 4.7 shows the z vertex distribution of the data sample compared to MC events. The distribution is well compared within the region of ± 35 cm around the zero value ($z = 0$ cm), however, the far z edges show some visible difference between the data sample and the sample predicted by the HERWIG generator. As the beam–gas reactions are expected to have a flat distribution along the z axis, thus a fraction of such background is expected to be in the final data sample. For this the correction is made.

The number of sample events outside the 35 cm z range is

$$N_{H1}^{|VTX|>35} = 16$$

for the data and

$$N_{MC}^{|VTX|>35} = 10.22$$

for normalized HERWIG events. Assuming all the beam–gas background has the vertex reconstructed, the number of background in the full event sample N_{bg}^{GAS} is

$$N_{bg}^{GAS} = \left(N_{H1}^{|VTX|>35} - N_{MC}^{|VTX|>35} \right) \cdot l_z \ , \tag{4.30}$$

where l_z is the correction factor for the distribution along z axis. The final number of background reads

$$N_{bg}^{GAS} = 7.01 \pm 4.0(\text{stat.}) \ . \tag{4.31}$$

This contribution to the cross–section is considered as 6% systematic error.

Conservation laws

To recognize the ep interaction out of cosmic muons, halo muons or any background overlapping the signal events, the total $E-p_z$ of an event is taken into account. Assuming that initial proton and electron have their four momenta

$$(E_p, 0, 0, E_p) \ , \qquad (E_e, 0, 0, -E_e) \ ,$$

respectively, the total $\sum(E - p_z)$ of the particles before and after collision must be conserved:

$$\sum_{final} (E - p_z) = \sum_{initial} (E - p_z) \ . \tag{4.32}$$

The $E - p_z$ of the proton is zero, so the initial $E - p_z$ is that of beam electron, which is $\sum_{initial}(E - p_z) = 2E_e$.

For the final state, we have a number of the hadronic final state particles, the photon and the scattered electron, thus finally,

$$2E_e = \sum_{initial} (E - p_z) = \sum_{final} (E - p_z) = \sum_{j \in \text{HFS},\gamma} (E_j - p_{j_z}) + 2E_{e'} \ , \tag{4.33}$$

since the final electron is scattered under polar angle $\theta_{e'} \approx 180°$, therefore $p_{e'_z} \simeq -E_{e'}$.

Having the $E_e = 27.6$ GeV, the initial sum evaluates to 55.2 GeV and, by considering the detector resolutions, the appropriate cut is applied

$$45 < \sum_{final} (E - p_z) < 65 \text{ GeV} \ . \tag{4.34}$$

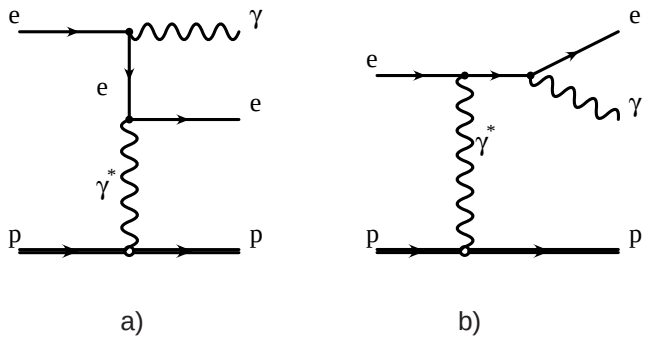

Figure 4.8: The bremsstrahlung processes; the photon is radiated by the electron line *(a)* before or *(b)* after the electron reaction with the proton line.

Apriori, other processes can give the same observed final state ($e\gamma p$) as the diffractive photoproduction of high t photon. This would lead to the unwanted background contributions to the final cross–section, thus the estimation of these processes must be made in order to subtract them from the measurement.

4.6.1 The Bremsstrahlung

One of such a processes is the bremsstrahlung having the same final state particles, that is the electromagnetic contribution to the reaction $ep \longrightarrow e\gamma p$, where the final state photon is radiated by the electron line either in the initial or final state (see Fig. 4.8).

The kinematics of the bremsstrahlung process is different from that of the diffractive photoproduction of high t photon. From the momentum conservation law, the transverse momentum p_T^γ of the final photon must balance the transverse momentum $p_T^{e'}$ of the electron. In this analysis, the scattered electron is tagged by the electron tagger and therefore $p_T^{e'} \sim 0$. This implies the p_T^γ to be almost zero too and photon is expected to be detected by the photon detector. This process has a high cross–section and is used for the luminosity measurement, however in this analysis the scattered final state photon is detected in the SpaCal due to its high transverse momentum, therefore, together with the scattered electron in the electron tagger, any contribution from the bremsstrahlung is expected to be negligible.

4.6.2 Diffractive ω^0 Production

Another process that could fake the final state of high-p_T photoproduction is the diffractive vector meson production of the ω^0 meson. The ω^0 meson is considered for being the lightest of the vector mesons which decays (directly or indirectly) to electromagnetic particles.

For the main channel $\omega^0 \longrightarrow \pi^+\pi^-\pi^0$ (89.1%) with subsequent decay of the neutral π meson into a photon pair $\pi^0 \longrightarrow \gamma\gamma$, this process could fake the final high-p_T photon in SpaCal if both of the photons from the π^0 decay occupy the same cluster or if only one photon is detected. The less probable channel $\omega^0 \longrightarrow \pi^0\gamma$ (8.7%) with subsequent decay of $\pi^0 \longrightarrow \gamma\gamma$ gives even three photons in the final state.

For the ω^0 decay photons registered in the SpaCal having a high transverse momentum, the hard scale must be present in the process.

However, the events generated by the DIFFVM event generator showed that this background is negligible [1] compared to the luminosity considered.

4.6.3 DIS Overlap

Another situation that could happen is the overlapping of two different events resulting together into the same final particles and topology as the high-p_T photon has. Considering two events

- a DIS with the scattered electron in the SpaCal and
- the bremsstrahlung having the electron tagged by the 33 m electron tagger,

the topology may be, theoretically, mimicked. However, concerning the bremsstrahlung, the photon energy detected in the photon detector would make the fail to pass the cut (4.22). On the top of this, two fully reconstructed overlapping events would cause the $\sum(E - p_z) = 110.4$ GeV.

Further, by the abilities of the H1 detector, the DIS final electron would leave its track registered in one of the trackers and therefore could not pass the cut for high-p_T photon, which is to have no track assigned to it.

As a conclusion, the DIS + bremsstrahlung can not mimic the diffractive photoproduction at high t in a sensible way under the present cuts.

4.6.4 Inclusive Diffraction

The background contribution of the inclusive elastic diffractive processes $\gamma p \longrightarrow Xp$ was studied by [1] using the PHOJET event generator to simulate these processes. The possibility is that an electromagnetic cluster in the SpaCal from the X system may fake the high-p_T photon while all other hadronic activity falls below the noise cut in the SpaCal or is not detected. However, for a luminosity of 11 pb^{-1} none of the events is expected to pass the full analysis cuts.

However, no to rely only on the simulated estimate this background was investigated further [1]. The cuts were loosened and an estimate was made. The interest is on the number of tracks of the X system detected by the CTD. By comparing the number of vertex and nonvertex fitted tracks of the PHOJET sample to the H1 data sample with the full selection considered in previous sections, the cut on the number of central vertex fitted tracks N_C^{VF} and central nonvertex fitted tracks N_C^{nVF} was estimated to suppress this background, without rejecting good diffractive high-p_T photon events,

$$N_C^{VF} < 10 \; ; \tag{4.35}$$

$$N_C^{nVF} < 10 \; . \tag{4.36}$$

4.7 Run Selection and Subtrigger Selection

Selection of the events used in this analysis is based on the requirements of the subdetector status, the run quality and the trigger conditions.

4.7.1 Detector Status

The detector status of all subdetectors whose readout is used in this analysis must be ON (HV status) and operational, with absence of any alarms (Slow Control). The main and necessary components of H1 detectors according to the topology of the diffractive photoproduction of high t photon are the CJC1, CJC2, the LAr calorimeter, the SpaCal calorimeter, BST, LUMI system and ToF and Veto walls.

4.7.2 Run Selection

The running period considered within this thesis includes the years 1999 and 2000, taking into account periods listed in Tab. 4.1. The 2000 e$^+$ shifted vertex period is not considered thus the corresponding run range count runs

$$231721 - 279215.$$

year	*type*	*filelist*
1999	e^-	`$H1DIST/eventlists/list.2.5.8.dst3.99eminus.rfio.d00-05.root`
1999	e^+ minimum bias	`$H1DIST/eventlists/list.2.5.8.dst3.99minbias.rfio.d00-04.root`
1999	e^+ no minimum bias	`$H1DIST/eventlists/list.2.5.8.dst3.99eplus.rfio.d00-06.root`
2000	e^+ nominal vertex	`$H1DIST/eventlists/list.2.5.8.dst3.00nom.rfio.d00-16.root`

Table 4.1: The run periods considered, together with the lepton beam type and the filelists of stored data (given here for the internal H1 use).

Out of these, only those runs are accepted, which are flagged as 'good' or at least 'medium' implying all major components to be operational (CJC, SpaCal, LAr, Luminosity system). The runs marked as 'poor' are not considered within this thesis.

Also, the run must have an integrated luminosity of over 0.2 nb^{-1} as the smallness of these runs reflects data acquisition problems in most of the cases.

4.7.3 Subtrigger Selection

As previously stated, the final state photon is detected by the electromagnetic part of the SpaCal and the corresponding subtrigger triggers on this photon. Besides, the scattered electron detected by the electron tagger can also be used in the trigger. The level one trigger elements (see section 3.2.7) used in this analysis are the *inclusive electron trigger* IET of the SpaCal, the *electron tagger trigger* ET, the *photon detector trigger* PD and the *ToF and veto wall trigger*. These were combined with further L2 and L4 conditions. The two subtriggers are:

- **S0**
  The S0 subtrigger is the trigger for low Q^2 physics and uses the L1 trigger element `SPCLe_IET>2` to trigger on an electromagnetic particle with energy above 6 GeV in the outer SpaCal, with combination of the ToF elements to ensure a good timing signals.

  The logical definition of S0 is

  L1: `SPCLe_IET>2` $\wedge$ `ToF&VETO`

  where `ToF&VETO` stands for the ToF and veto walls trigger elements. The efficiency of the IET part of S0 is displayed in Fig. 4.9 as a function of the cluster energy. Due to different energy thresholds of the IET triggers during the 1999 minimum bias run period and the rest of periods considered within this analysis, the efficiencies differ.

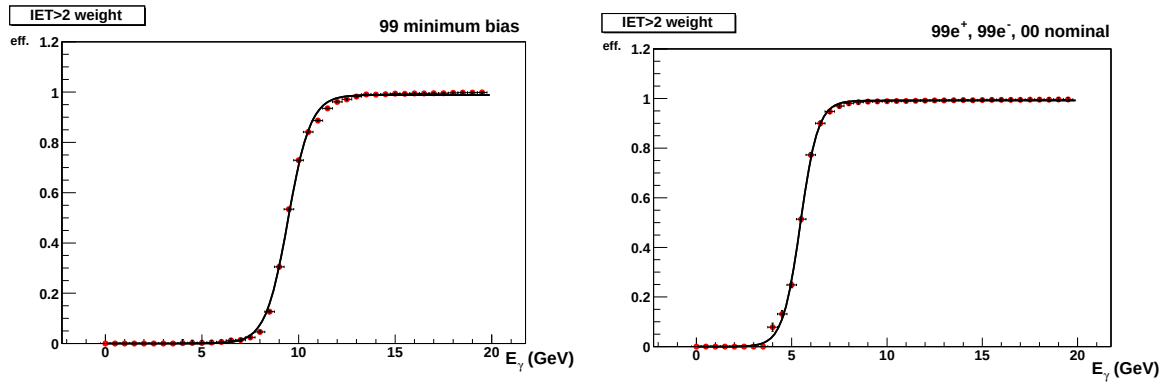

Figure 4.9: The IET above threshold 2 efficiency used in the S0 subtrigger during the periods of *left)* 1999 minimum bias and *right)* 1999 e^-, 1999 no min. bias, 2000 nom. vertex with the fit (the solid curve).

run period	*trigger element*	*energy threshold*	*SpaCal region*
1999 e^+ minimum bias	`SPCLe_IET_Cen_2`	5 GeV	inner
	`SPCLe_IET>1`	5 GeV	outer
	`SPCLe_IET>2`	10 GeV	outer
standard running	`SPCLe_IET_Cen_2`	2 GeV	inner
	`SPCLe_IET>1`	2 GeV	outer
	`SPCLe_IET>2`	6 GeV	outer

Table 4.2: SpaCal IET trigger element definitions for the different run periods of the years 1999 and 2000; only those used in this analysis are displayed.

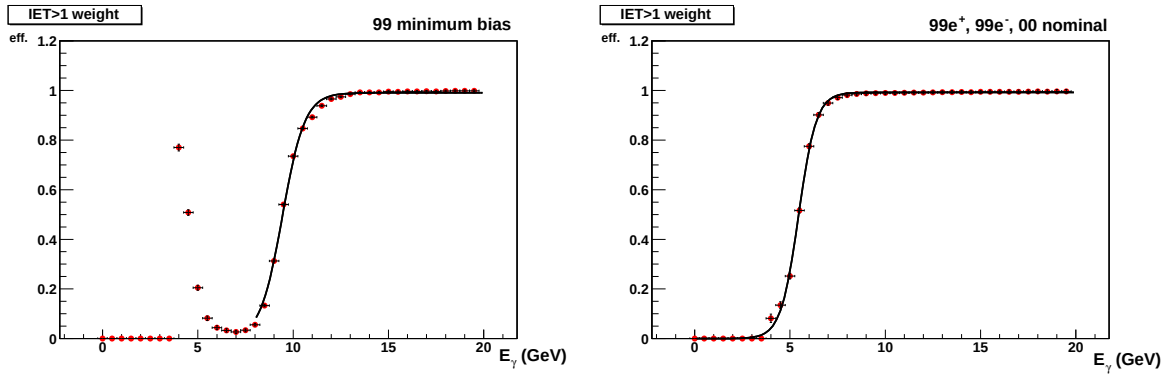

Figure 4.10: The IET above threshold 1 efficiency used in the S50 subtrigger during the periods of *left)* 1999 minimum bias, *right)* other periods. The curve represents the fit.

- **S50**
  The S50 subtrigger uses the L1 trigger element `SPCLe_IET>1` – the electromagnetic cluster in the outer SpaCal with energy greater than 2 GeV or an electromagnetic cluster in the central region of the SpaCal above the threshold level 2, `SPCLe_IET_Cen_2`. Also, the requirement is put for the 33 m electron tagger to have an energy deposit above the threshold `LU_ET` in coincidence with no signal above the threshold in the photon tagger `LU_PD_low` to reject bremsstrahlung events. Among the timing signals from ToF, this subtrigger has the L2 element `SPCL_R30`, a requirement that the particle was detected in the outer SpaCal (above ~ 30 cm from the z axis).

  The logical definition of S50 is

  L1: $(\texttt{SPCLe\_IET>1} \vee \texttt{SPCLe\_IET\_Cen\_2}) \wedge \texttt{LU\_ET} \wedge \rceil\texttt{LU\_PD\_low} \wedge \texttt{ToF\&VETO}$

  L2: `SPCL_R30`

  The efficiency of the S50 IET elements are shown in Fig. 4.10 taking into account different periods.

The ToF and veto walls trigger element efficiencies are assumed to be 100%.

Generally, the S50 subtrigger have a lower prescale than S0. In some runs the prescale of one or both of them is too high, meaning that lots of good event candidates are rejected. Therefore, the condition for the run to be accepted is that the prescales $\mathcal{P}$

of both the S0 and the S50 subtriggers are to be lower or equal to 10,

$$\mathcal{P}_{S0} \leq 10 \quad \wedge \quad \mathcal{P}_{S50} \leq 10 \ .$$

The corresponding cut on the S0 and S50 subtrigger was then applied to two sets of events based on the L2 effect of the S50 subtrigger:

- for events with the final photon being detected within the outer region of electromagnetic SpaCal, the condition was required to have fired the subtrigger of a lower prescale,
- while for events with photon in the inner region of SpaCal, the requirement was loosened to only have S0 fired.

This dependence of the SpaCal regions is due to the subtrigger definitions, mainly due to S50, which operates only in outer SpaCal (L2 element `SPCL_R30`).

Tab. 4.2 shows the energy thresholds for all the periods used. The fit of the efficiencies is of the form

$$\epsilon(E) = \frac{p_0}{e^{p_1 - \frac{E}{p_2}} + 1} \ , \tag{4.37}$$

where p_0, p_1, p_2 are free parameters. Since the IET>1 and IET>2 energy thresholds seem to be at the same values, the bug is expected in the calculation algorithm that will be further analyzed in the near future. However, as a temporary, the efficiencies of the S0 and S50 subtriggers for the period considered were set to be $\approx 100\%$ efficient by [1], but will have to be checked in the future.

4.8 The Selection Cut Summary

The full selection criteria for selection of diffractive photoproduction of high-p_T photons used in this thesis are presented in Tab. 4.3

4.9 The Sample Distributions

The final sample distributions are shown here, after all cuts applied. The sample is compared to the HERWIG data normalized to the number of events in the weighted control sample. The Fig. 4.11 shows the photon distributions - its energy, transverse momentum and angles θ and ϕ. All of them are described reasonably, however the slope of p_T^γ distribution is very sensitive to the simulation parameters as the α_s [1]. Both samples show at least a steeply falling distribution.

cut type	*variable*	*cut*	*note*
preselection	$\mathcal{P}_{S0},\ \mathcal{P}_{S50}$	≤ 10	
	S0	1	γ in inner SpaCal
	S0 $\vee$ S50	1	γ in outer SpaCal
	RUN LUMI	> 0.2 nb^{-1}	
diffraction	$y_{I\!P}$	< 0.018	
	$\Delta\eta$	> 2	
high-p_T photopr.	N_{em}^{H1}	1	except ET
— electron	$\lvert x_{tag}\rvert$	< 6.5 cm	
	y	$\in (0.3, 0.6)$	
— photon	p_T^γ	> 2 GeV	hard scale
	E_γ	> 8 GeV	
	θ_γ	$\in (153, 176)$ °	
	CJC, BST	0	no tracks
further background	E_{PD}	< 2 GeV	bremsstrahlung
	E_{spacal}^{tot}	< 2 GeV	single particle
	E_{clus}^{max}	< 0.2 GeV	single particle
	E_{had}^γ	< 0.5 GeV	no hadrons
	$\sum_{final}(E - p_z)$	$\in (45, 65)$ GeV	
	N_C^{VF}	< 10	inclusive diffr.
	N_C^{nVF}	< 10	inclusive diffr.

Table 4.3: The selection cuts presented within this analysis to select the diffractive photoproduction at high t.

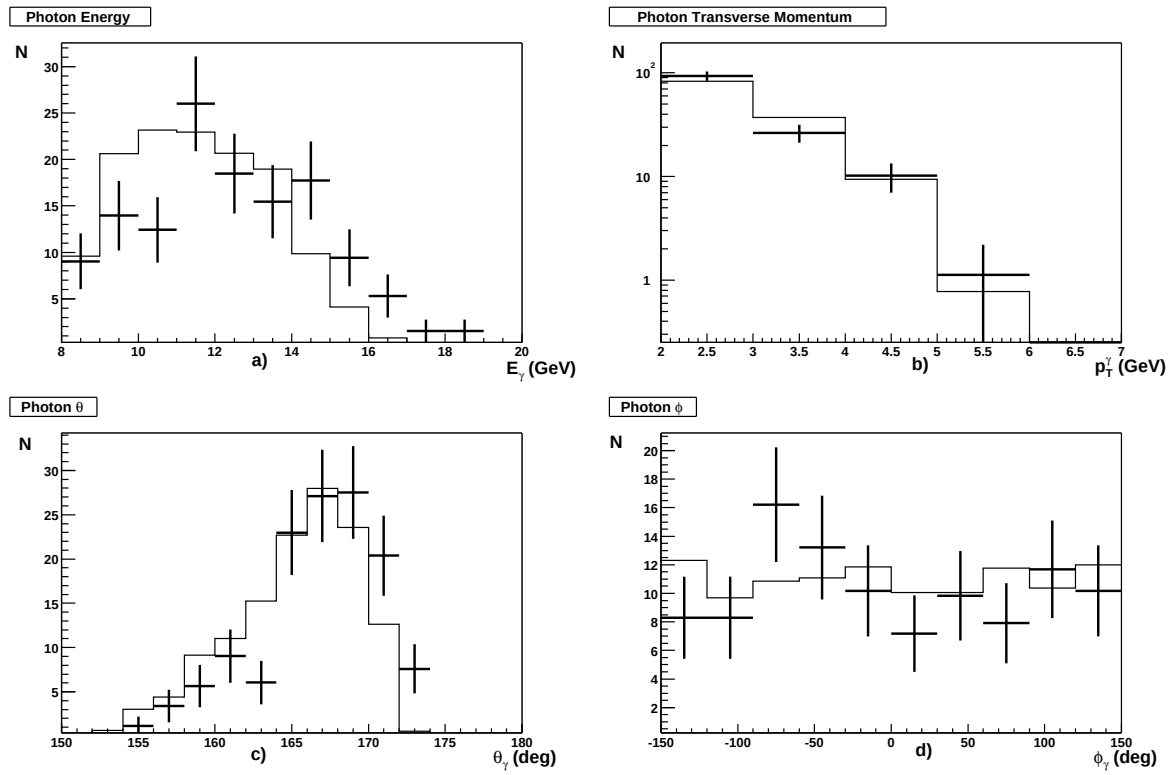

Figure 4.11: The full event sample distributions, *a)* energy of the final photon in the SpaCal, *b)* the transverse momentum of the photon, *c)* the polar θ distribution and *d)* the azimuthal ϕ of the photon. The data (crosses) are compared to the HERWIG prediction (solid lines).

Concerning the photon energy (Fig. 4.11a), a reasonable description of the data by the MC is observed. The θ_γ distribution description can probably be improved when beam tilt and beam shift effects w.r.t. SpaCal and SpaCal alignment will be included. Turning to the ϕ_γ distribution, the fluctuations seen on Fig. 4.11d are mainly due to low statistics of the full event sample.

In the Fig. 4.12, the distributions of the inelasticity y, the $E - p_z$ of the main H1 detector, the backward edge of the hadronic final state of the proton dissociation system is shown, together with the $y_{I\!P}$ and $x_{I\!P}$ variables. The θ_Y^{max} distribution shows a more significant peak at low values compared to HERWIG prediction, which comes out of a fact that the proton dissociating system spreads over too small angles around the z axis and is not registered by the LAr or Plug calorimeter. For the same reason the reconstructed $y_{I\!P}$ is zero, which is shown in Fig. 4.12d. However, the flat distribution is seen for both the Monte Carlo events and the event sample. The inelasticity and the $E-p_z$ are little shifted compared to MC prediction. This could result from an alignment or a calibration problem.

In the Fig. 4.13 the rapidities of the final high-p_T photon and the edge of the HFS system of the dissociated proton are depicted. The data are well described, showing the peak of the photon pseudorapidity at $\eta_\gamma \approx -2.3$. The $\Delta\eta$ is also well modelled showing the clear peak at approximately 3.5. As can be seen, the rapidity gaps of 6 units are not uncommon. However, this is due to cut on the $y_{I\!P}$ restricting the $\Delta\eta$ as

$$y_{I\!P} \approx \mathrm{e}^{-\Delta\eta} \ . \tag{4.38}$$

As an conclusion to the comparison between the HERWIG generated events and the H1 event sample can be said that the the photon diffraction off proton at large t is well described.

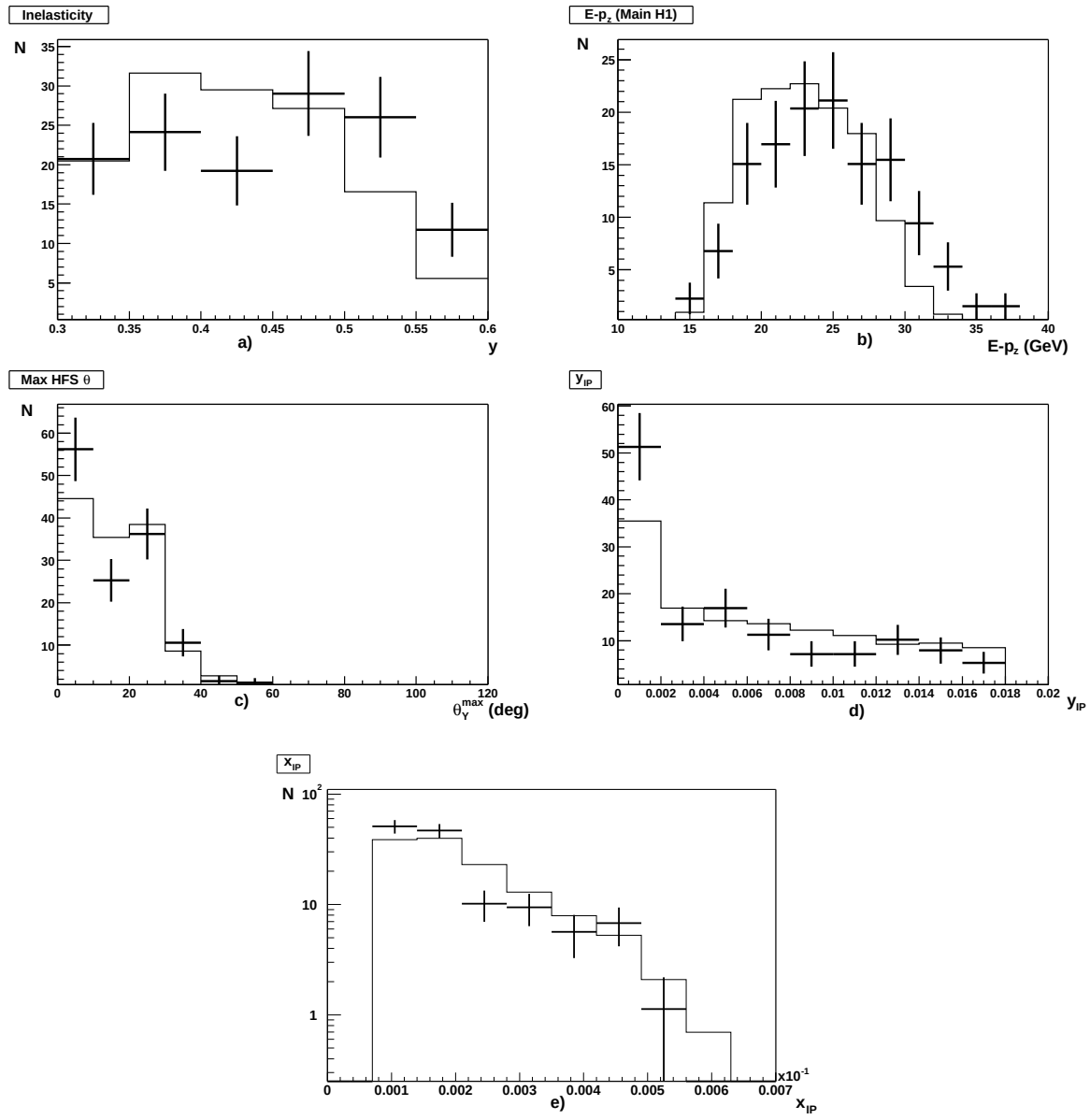

Figure 4.12: The full event sample distributions, *a)* the inelasticity y, *b)* the $E - p_z$ of the main H1 detector, *c)* the maximum polar angle of the HFS particles of the proton dissociation, *d)* the $y_{I\!P}$ variable and *e)* the $x_{I\!P}$ variable. The data (crosses) are compared to the HERWIG prediction (solid lines).

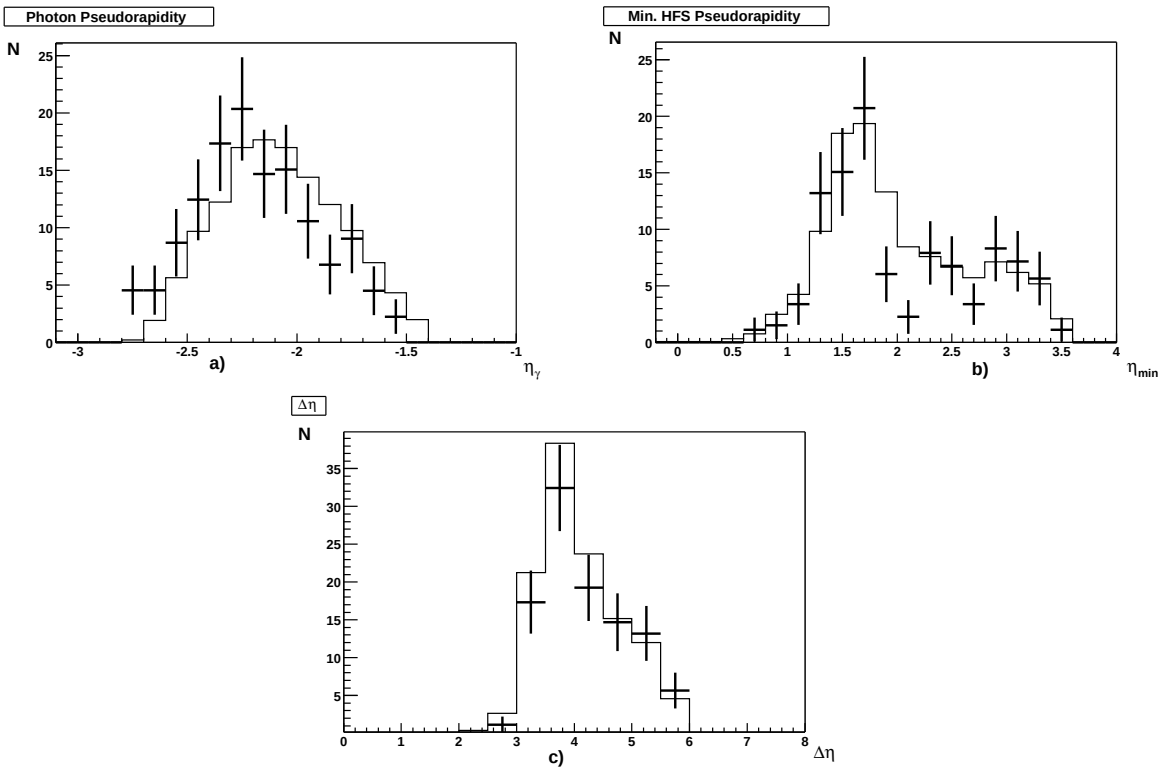

Figure 4.13: The full event sample distributions, *a)* the pseudorapidity of photon, *b)* the minimal HFS pseudorapidity and *c)* the rapidity gap between the final photon and the proton dissociation system. The data (crosses) are compared to the HERWIG prediction (solid lines).

Chapter 5

Cross–Section measurement

In this chapter, the all the necessary ingredients to the cross–section are discussed and the results are presented.

5.1 Cross–Section Determination

The differential electron–proton cross–section is obtained by the formula

$$\frac{\mathrm{d}\sigma^{ep}_{bin}}{\mathrm{d}x_{I\!P}} = \frac{N_{bin} - N^{back}_{bin}}{A_{bin} \cdot \epsilon \cdot \Delta x_{I\!P} \cdot \mathcal{L}} , \tag{5.1}$$

$$\frac{\mathrm{d}\sigma^{ep}_{bin}}{\mathrm{d}t} = \frac{N_{bin} - N^{back}_{bin}}{A_{bin} \cdot \epsilon \cdot \Delta t \cdot \mathcal{L}} , \tag{5.2}$$

where

- $\frac{\mathrm{d}\sigma^{ep}_{bin}}{\mathrm{d}x_{I\!P}}$, $\frac{\mathrm{d}\sigma^{ep}_{bin}}{\mathrm{d}t}$ are the differential cross–sections for a certain bin in $x_{I\!P}$ and t, respectively;
- N_{bin} is the number of sample events in the particular bin;
- N^{back}_{bin} is the number of background events in the bin;
- A_{bin} is the acceptance for a particular variable;
- ϵ is the efficiency factor of the event selection;
- $\Delta x_{I\!P}$, Δt are the actual bin sizes;
- $\mathcal{L}$ is the integrated luminosity of the event sample taken into account in this analysis, that is 36.9 pb^{-1}.

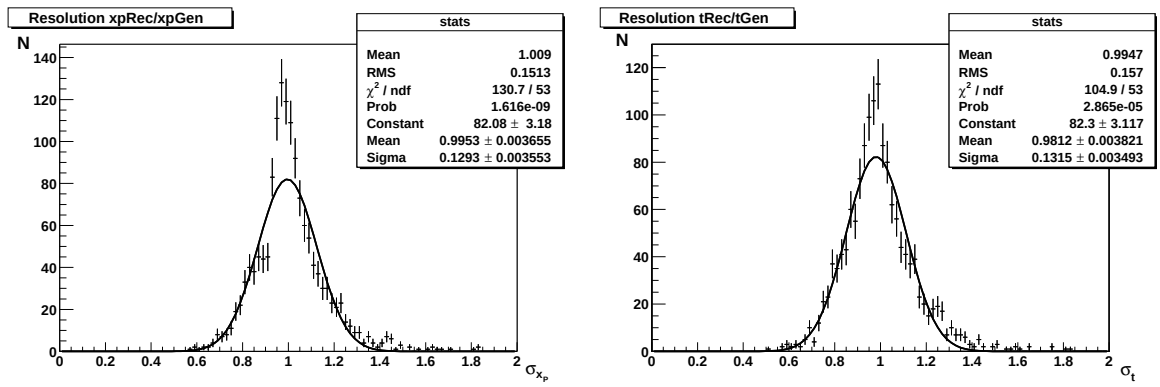

Figure 5.1: Resolutions of variables *left)* $x_{I\!P}$, *right)* t.

The photon–proton cross–section $\sigma^{\gamma p}_{bin}$ can be then computed from σ^{ep}_{bin} by considering the flux of photons at the electron–photon vertex for each bin in the cross–section as

$$\sigma^{\gamma p}_{bin} = \frac{\sigma^{ep}_{bin}}{f_{bin}} \tag{5.3}$$

(see section 5.7).

In the following, the acceptance, purity, stability and the photon flux factor are estimated, leading to a cross–section measurement.

5.2 Resolution

The resolution was estimated for the two variables $x_{I\!P}$ and t, in which the cross–section is differential.

The resolution σ_v of any variable v is defined as the ratio of its reconstructed value v_{rec} and the real value at the generator level v_{gen}. It thus operates on the Monte Carlo events which are passed by the program of H1 simulation and shows the detector property as an uncertainty of description of the variable v. It is defined as

$$\sigma_v = \frac{v_{rec}}{v_{gen}} \ . \tag{5.4}$$

The resolution distribution of the $x_{I\!P}$ and the momentum transfer t is depicted in Fig. 5.1. The values are computed to be

$$\sigma_{xpom} = 15.1\% \ , \qquad \sigma_t = 15.7\% \ .$$

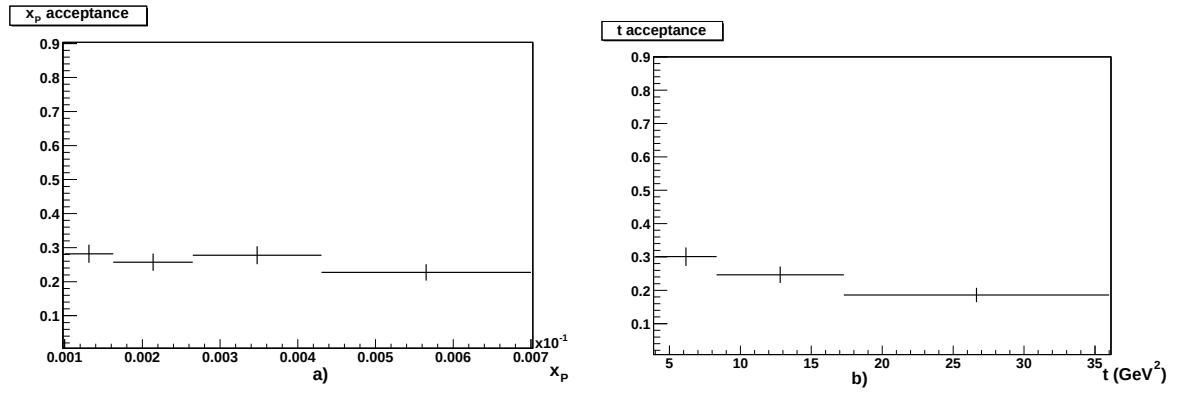

Figure 5.2: Acceptances of the variables *a)* $x_{I\!P}$, *b)* t used in the cross–section measurement.

The binning of the final cross–section depends on these resolutions as each bin must be larger than the resolution of appropriate variable to reduce the migration effects over the bins.

5.3 Acceptance Correction

The acceptance A_v of any variable v is defined as the ratio of the number of the reconstructed events N_{rec} in a certain bin of the variable v and the number of the generated events N_{gen} in the same bin. Thus the formula reads

$$A_v = \frac{N_{rec}}{N_{gen}} \ , \tag{5.5}$$

where the reconstructed events are those passed all the selection criteria described in chapter 4 and the generated events are those of the kinematic domain $\mathcal{D}(x_{I\!P}, t, y_{I\!P}, W)$ which is

$$\begin{aligned} 0.1 \ < \ x_{I\!P} \ &< \ 0.7 \ \times 10^{-3} \ , \\ |t| \ &> \ 4 \ \text{GeV}^2 \ , \\ y_{I\!P} \ &< \ 0.018 \ , \\ 175 \ < \ W \ &< \ 247 \ \text{GeV} \ . \end{aligned}$$

The A_v takes into account the limited geometrical acceptance of the detector induced by the cuts and the migration effects due to the limited resolution of the detector. Both the acceptances of the variables $x_{I\!P}$ and t were estimated and are shown in Fig. 5.2. The average acceptance of both variables $x_{I\!P}$ and t is above 20%.

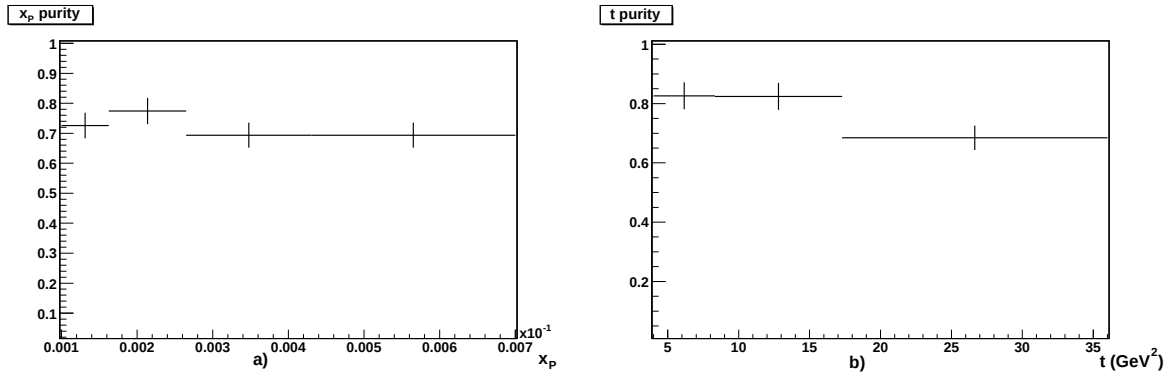

Figure 5.3: Purities of the variables *a)* $x_{I\!P}$ and *b)* t for the bins used in the measurement.

5.4 Purity and Stability

Purity P and stability S is introduced to control the quality of the measurement. The purity of any variable v is defined by

$$P_v = \frac{N_{rec\&gen}}{N_{rec}} \ , \tag{5.6}$$

where $N_{rec\&gen}$ denotes the number of events of which the variable v was generated and reconstructed in the same bin and the N_{rec} is the number of events reconstructed in the same bin. For the ideal detector of a resolution 0%, it would reconstruct all variable values in the same bin as they were generated, leading to a purity of 1. However, all of the real subdetectors have a non–zero resolution and therefore a smearing of the values leading to the migrations over the bins implying the appropriate purity of any variable v to be less then one. Anyway, the higher the purity the fewer migrations occur on the variable spectrum.

The purities of the variables $x_{I\!P}$ and t are depicted in Fig. 5.3 showing that average purity is above 70%.

The stability S of any variable v is defined as

$$S_v = \frac{N_{rec\&gen}}{N_{gen}} \ . \tag{5.7}$$

Again, for the ideal detector where no migrations occur, the stability $S_v = 1$. As for the real status of any detector, the migration of the values leads to decreasing the $N_{rec\&gen}$ resulting into stability value smaller than 1.

The stability of the $x_{I\!P}$ and t are shown it Fig. 5.4.

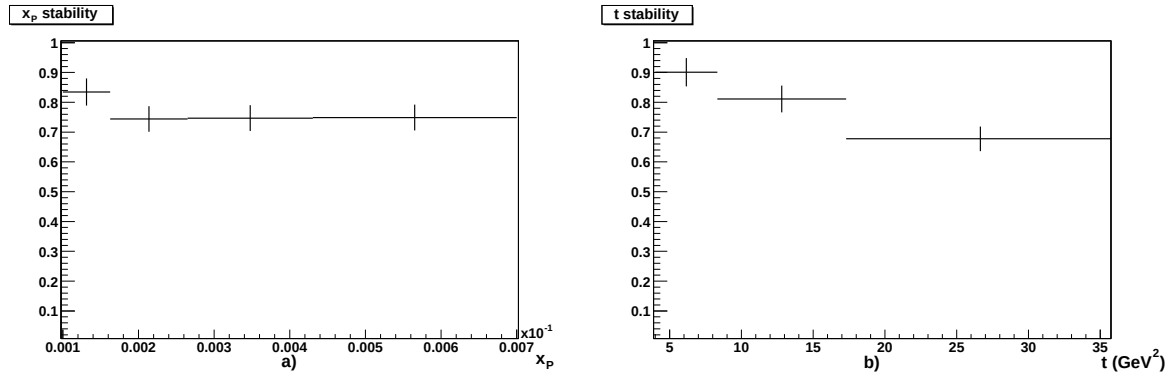

Figure 5.4: Stabilities of the *a)* $x_{I\!P}$ and *b)* t.

5.5 Trigger Efficiency

As previously stated in section 4.7.3, the subtrigger efficiencies were measured for both the S0 and S50 via the efficiencies of the L1 trigger elements. However, due to problems with the energy thresholds of different levels, the efficiency used for the cross–section measurement was taken from the work [1] where both the efficiency of S0 and S50 were estimated to be 100% efficient during the run period considered.

5.6 Systematic Errors

The errors taken into account in the measurement of the cross–section are divided into two groups, the statistical errors and the systematic errors. The systematic error raise due to uncertainties in the quantities measured by the detector components:

- luminosity measurement — ±1.5%;
- photon energy in EM SpaCal — ±1%;
- photon angle of an electromagnetic cluster in SpaCal — ±1 mrad;
- LAr hadronic energy scale — ±4%;
- ET33 energy — ±1.5%;
- total four vector of the noise subtracted from calorimeters is varied by ±30%.

Together with the uncertainties of the detector, the inputs to the Monte Carlo generator should be taken into account. The systematic errors considered were the $x_{I\!P}$ slope, the t slope and the M_Y slope, [1].

The background from the inclusive diffraction and the background from the beam–gas events was also considered as the contribution to the systematic error.

For the present state, due to the lack of time, the systematic errors were estimated from the work of [1] and normalized to the cross–section with the contribution from the beam–gas events (±6%) added.

5.7 Photon Flux Factor

For the transition from the electron–proton cross–section σ_{ep} to the photon–proton cross–section $\sigma_{\gamma p}$, the flux of the photons from the electron line is needed:

$$\frac{\mathrm{d}^2\sigma_{ep}(s)}{\mathrm{d}Q^2\mathrm{d}y} = \sigma_{\gamma p}(ys)F(y,Q^2) \ , \tag{5.8}$$

where $F(y,Q^2)$ is the photon flux factor.

For both $x_{I\!P}$ and t no dependence on y is seen over ranges measured and the constant flux factor is applied to all bins [1],

$$f = \int F(y,Q^2)\ \mathrm{d}y\mathrm{d}Q^2 = 9.66 \times 10^{-3} \ . \tag{5.9}$$

5.8 The Cross–Section differential in $x_{I\!P}$

The γp cross–section was computed differentialy in $x_{I\!P}$ and is depicted in Fig. 5.5. The comparison has been made to the HERWIG prediction and to the cross–section measured by the H1 Collaboration.

Fig. 5.6 shows the $\mathrm{d}\sigma_{\gamma p}/\mathrm{d}x_{I\!P}$ compared to the fit motivated by the prediction [20] that differential cross–section varies as

$$\frac{\mathrm{d}\sigma_{\gamma p}}{\mathrm{d}x_{I\!P}} \approx \frac{1}{W^2}\left(\frac{1}{x_{I\!P}}\right)^{2\omega_0+2} \ , \tag{5.10}$$

where $\omega_0 = \frac{3\overline{\alpha_s}}{\pi}4\ln 2$. From this, the pomeron intercept $\alpha(0) = 1+\omega_0$ and $\overline{\alpha_s}$ can be achieved.

Based on this prediction, the fit function then reads

$$f(x_{I\!P}) = \frac{1}{\overline{W}^2}\left(\frac{1}{x_{I\!P}}\right)^{n} \ , \tag{5.11}$$

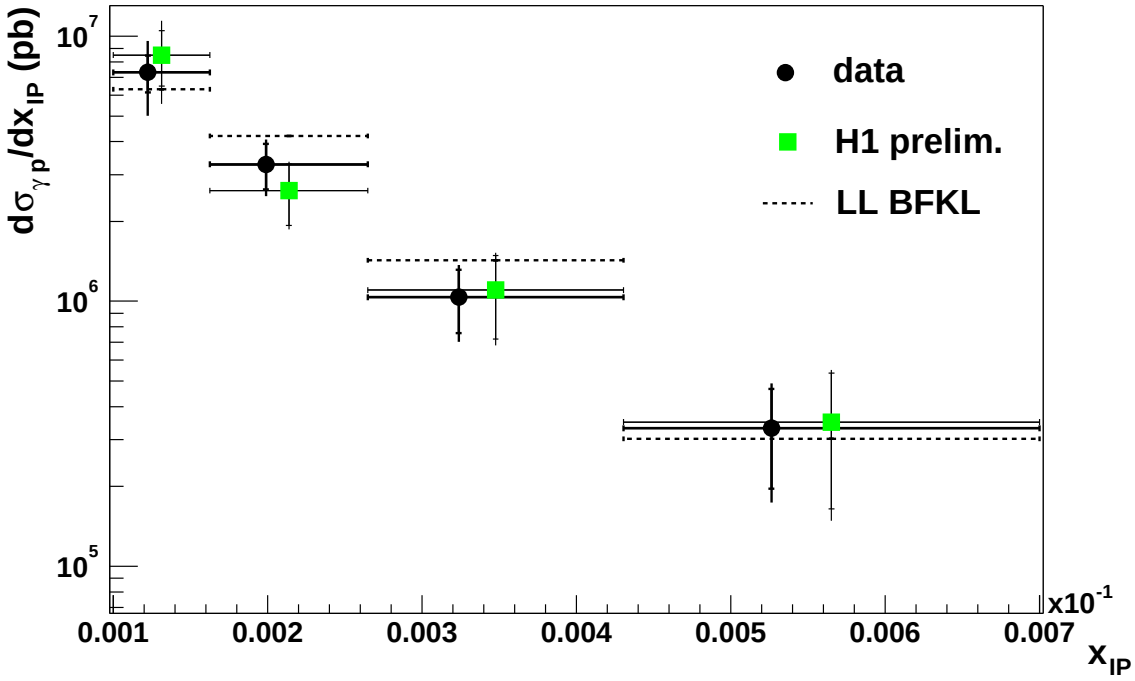

Figure 5.5: The γp cross–section (circles) differential in $x_{I\!P}$ for the kinematic domain $y_{I\!P} < 0.018,\ 0.0001 < x_{I\!P} < 0.0007,\ 175 < W < 247$ GeV, $|t| > 4$ GeV^2. The inner error bars show the statistical errors while the outer error bars show the systematical and the statistical errors added in quadrature. The cross–section is compared to the HERWIG prediction and to the preliminary results of H1 Collaboration [2] (squares). The HERWIG prediction is normalized to the cross–section (allowed by the normalization uncertainty of the LLA BFKL calculation).

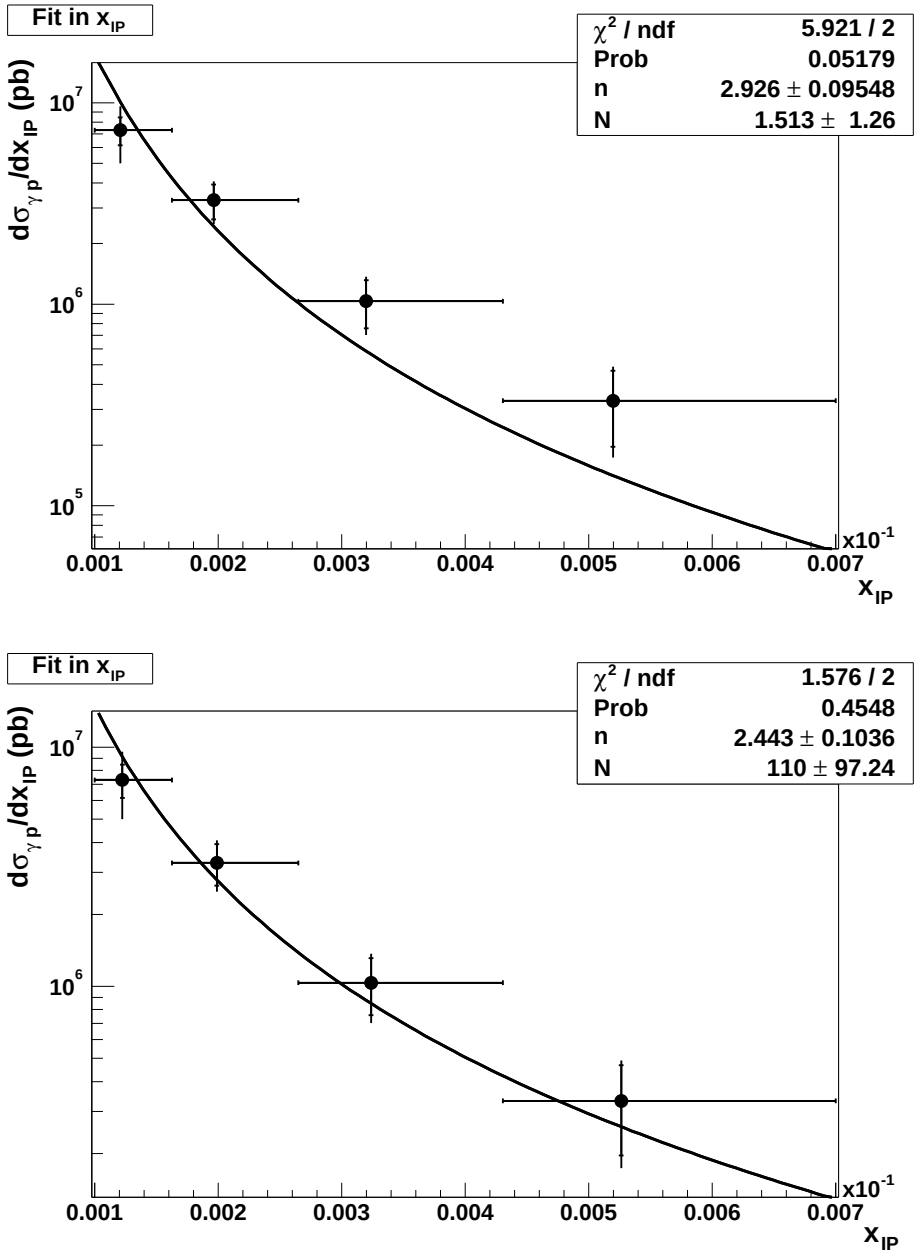

Figure 5.6: The fit of the γp cross–section differential in $x_{I\!P}$ by the form $(1/\overline{W}^2)(1/x_{I\!P})^n$ with normalization N. Two fits are shown, with the different initial parameters. The inner error bars show the statistical errors while the outer error bars show the systematical and the statistical errors added in quadrature.

$x_{I\!P}$ range ($\times 10^{-3}$)	N	$\frac{d\sigma_{\gamma p}}{dx_{I\!P}}$ (nb)	stat. error (nb)	syst. error (nb)	total error (nb)
0.10 – 0.16	40	7.3×10^3	1.1×10^3	2.0×10^3	2.3×10^3
0.16 – 0.26	26	3.3×10^3	0.6×10^3	0.5×10^3	0.8×10^3
0.26 – 0.43	14	1.0×10^3	0.3×10^3	0.2×10^3	0.3×10^3
0.43 – 0.70	6	3.3×10^2	1.4×10^2	0.8×10^2	1.6×10^2

Table 5.1: The bin–by–bin values of γp cross–section differential in $x_{I\!P}$ including errors and number of events in each bin.

where the mean value is taken from the event sample and is $\overline{W} = 208.8$ GeV. The center–of–bin correction was applied, taking into account the distribution in different bins of $x_{I\!P}$.

Two different fits are shown, with a different initial parameters. As can be seen, the fit procedure converges for two solutions. One close to the expected value of $\alpha_s = 0.176 \pm 0.018$ with a large $\chi^2/NDF = 5.9/2$ and another at $\alpha_s = 0.084 \pm 0.020$ with a better $\chi^2/NDF = 1.6/2$. Both fits give very large uncertainties on the normalization parameter. The error on the slope parameter n is amazingly smaller in the case of the largest χ^2/NDF. This means that the curve of this solution is further away from the data points but gives a more stable solution. Therefore the result of $\alpha_s = 0.176 \pm 0.018$ will be kept as the preferred solution. The other solution is considerd as an unstable local minimum. The fit corresponds to a pomeron intercept

$$\alpha(0) = 1.46 \pm 0.05$$

and the $\overline{\alpha_s} = 0.176 \pm 0.018$. The values of the γp cross–section for each bin of $x_{I\!P}$ are shown in Tab. 5.1.

5.9 The Cross–Section differential in t

The cross–section differential in the squared four momentum transfer t was measured. The cross–section is depicted in Fig. 5.7, together with the center–of–bin correction and compared to the HERWIG prediction and to the measurement done by the H1 collaboration [2]. The values of the γp cross–section for each bin of t are shown in Tab. 5.2.

The fit for the $d\sigma_{\gamma p}/dt$ cross–section is shown in Fig. 5.8. The fit was chosen of the form of $|t|^{-n}$ with the normalization A and holds the value of $n = 1.98 \pm 0.29$ with the $\chi^2/NDF = 0.531/1$. The corresponding values of the cross–section and errors are

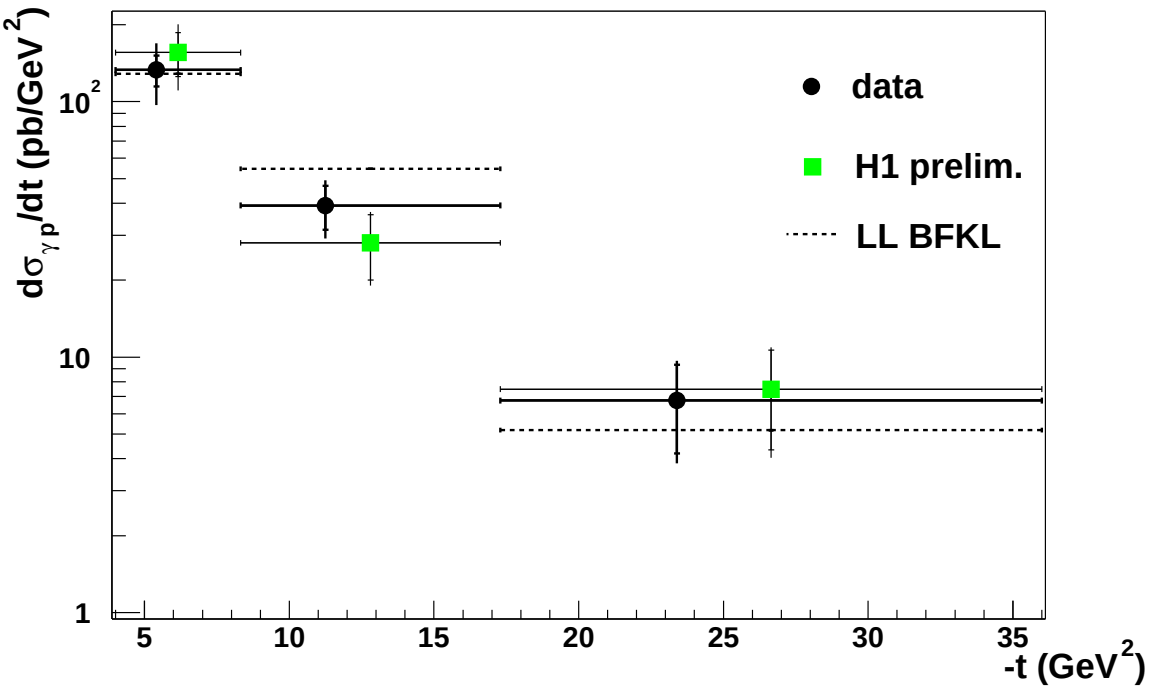

Figure 5.7: The γp cross–section (circles) differential in the momentum transfer t for the kinematic domain $y_{I\!P} < 0.018,\ 0.0001 < x_{I\!P} < 0.0007,\ 175 < W < 247$ GeV, $|t| > 4$ GeV^2. The inner error bars show the statistical errors while the outer error bars show the systematical and the statistical errors added in quadrature. The cross–section is compared to the HERWIG prediction and to the results from H1 Collaboration [2] (squares). The HERWIG prediction is normalized to the cross–section.

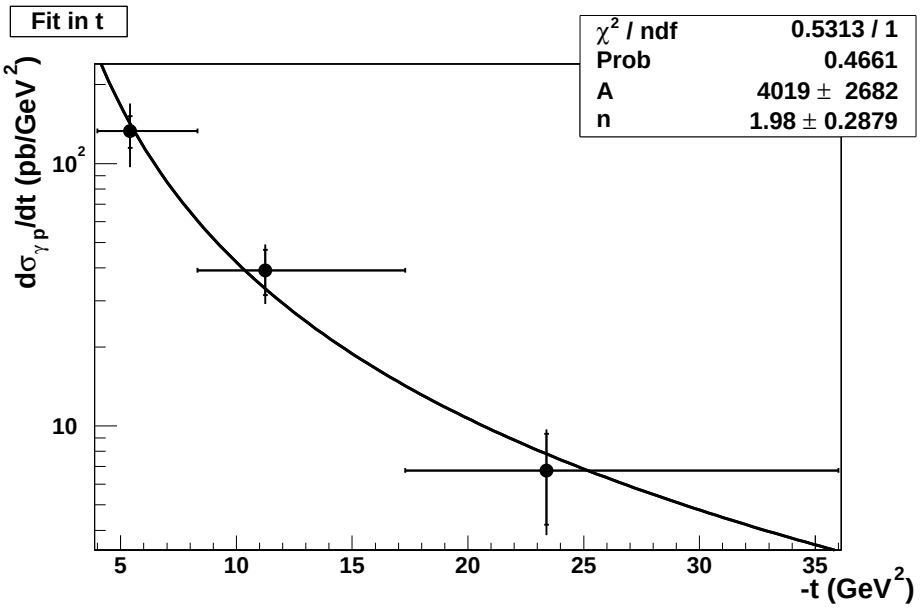

Figure 5.8: The fit of the γp cross–section differential in t by the fit of the form $|t|^{-n}$ with normalization A. The inner error bars show the statistical errors while the outer error bars show the systematical and the statistical errors added in quadrature.

$\|t\|$ range (GeV^2)	N	$\frac{\mathrm{d}\sigma_{\gamma p}}{\mathrm{d}t}$ ($\mathrm{pb/GeV}^2$)	stat. error ($\mathrm{pb/GeV}^2$)	syst. error ($\mathrm{pb/GeV}^2$)	total error ($\mathrm{pb/GeV}^2$)
4.00 – 8.32	53	133	18	31	36
8.32 – 17.30	26	39	7.7	6.4	10
17.30 – 36.00	7	6.7	2.5	1.4	2.9

Table 5.2: The bin–by–bin values of γp cross–section differential in t including errors and number of events in each bin.

shown in Tab. 5.2.

5.10 Discussion

The steep rise of the cross–section differential in $x_{I\!P}$ with $1/x_{I\!P}$ was observed, which is an indication of the presence of a hard process. The fixed $\overline{\alpha_s}$ of the BFKL prediction was set to $\overline{\alpha_s} = 0.17$. The similar value is observed in the fit of the result ($\overline{\alpha_s} = 0.176 \pm 0.018$) which can be compared directly to the preliminary result of the H1 Collaboration, which was measured to be $\overline{\alpha_s} = 0.187 \pm 0.004$. The measured value of the pomeron intercept $\alpha(0) = 1.46 \pm 0.05$ is compatible with $\alpha(0) = 1.50 \pm 0.01$ obtained by the [2]. It can be compared to the value of $\alpha(0) = 1.167 \pm 0.048(\mathrm{stat.}) \pm 0.024(\mathrm{syst.})$, measured by H1 in the diffractive photoproduction of J/ψ mesons at large t [26], however the energy dependence of the cross–section of the considered process is the steepest energy dependence measured in diffraction at HERA. This leads to the large pomeron intercept $\alpha(0)$, as measured in this thesis.

Comparing the recent H1 preliminary results, the cross–section differential in $x_{I\!P}$ measured within this thesis shows little better agreement with the theory predicted by the leading log approximation of the BFKL prediction. However, no major difference to the H1 preliminary result is observed, and both results are compatible within the errors.

The cross–section differential in the four momentum transfer t is well described by the fit of the form $A|t|^{-n}$ with $n = 1.98 \pm 0.29$ and in agreement with the LLA BFKL prediction. However, the value of $n = 3.78 \pm 0.17(\mathrm{stat.}) \pm 0.06(\mathrm{syst.})$ measured by H1 in the diffractive photoproduction of J/ψ mesons at large t [26] refers to the steeper slope in t. Considering the H1 preliminary results, the cross–section of this work is significantly in better agreement with the theory.

The main differences between the present work and the H1 preliminary results are

the different treatment of the trigger selection including the correction for the prescale factor and L2 effect simulation that is expected to be more efficient in the present work; the different cuts on the detector HV status (few were missing in [2]); run selection was applied for the BST unvalidation (not applied in [2]); bin center corrections in the cross–section fit procedures (not included in [2]); Electron Tagger acceptance was treated in a different way (more precise in [2]), not done here due to lack of time.

As far as this work is not yet closed, further analysis in the near future can show another improvements of the already achieved results. The main steps to be analyzed is the backward silicon tracker treatment that would improve the photon identification through its track unvalidation. The requirement on the absence of energy deposit in the LAr above the noise threshold, between the photon and the Y system, also the SpaCal alignment and calibration can lead to the better results as the changes in its alignment can misinterpret the quantities measured by the SpaCal. After the correction for the efficiencies of the `IET` elements and considering the LAr noise, beam tilt and the beam shift, the results will be further improved. Computing a systematic errors of the cross–section, together with the deeper analysis of the photon flux factor may result into more precise measurement in the future.

On the theoretical side, the contributions to the cross–section from the higher orders of the BFKL calculations may be important as well. For the present state, the independent measurement of the diffractive photoproduction at high t shows predicted steep rise with the energy and a good agreement with the theory.

Chapter 6

Summary

The diffractive process $\gamma p \longrightarrow \gamma Y$ where the final photon carries a large transverse momentum and is separated by the rapidity gap from the proton dissociative system Y was observed by the H1 detector at HERA. The process is particularly well suited to provide a precise measurement and to be compared to the QCD perturbative predictions in the BFKL high energy limit using the hard scale of the four momentum transfer $-t \gg \Lambda^2_{QCD}$.

The cross–section is presented differentially in the variables $x_{I\!P}$ and the square of the four momentum transfer t at the proton vertex and compared to the LLA BFKL calculation as implemented in the HERWIG event generator and the H1 preliminary results presented on summer 2003 at the HEP conference [2]. A reasonable description with the H1 result and the theory is found and the steep rise of the energy with the $x_{I\!P}$ is confirmed.

A fit of the form $(1/\overline{W}^2)(1/x_{I\!P})^n$ on the cross–section differential in $x_{I\!P}$ holds the pomeron intercept $\alpha(0) = 1.46 \pm 0.05$ corresponding to the value of $\overline{\alpha_s} = 0.176 \pm 0.018$ that is with comparison to the measurement of high t diffractive J/ψ meson a little higher, corresponding to the steepest energy slope measured in diffraction at HERA. The fit of the form $A|t|^{-n}$ performed on the cross–section differential in t yields $n = 1.98 \pm 0.29$ resulting into shallower t cross–section than seen for the high t diffractive J/ψ production.

The measurement should be further analyzed considering more detail treatment of relevant parts of H1 detector, taking into account the beam tilt and the beam shift, or further analyzing the photon flux factor.

Bibliography

[1] M. Beckingham: *Diffractive photoproduction at high p_T photons at HERA*, Ph. D. Thesis, University of Manchester (2003).

[2] H1 Collaboration: *Diffractive photoproduction of high-p_t photons at HERA*, International Europhysics Conference on High Energy Physics, EPS03, Aachen (2003).

[3] S. Egli, E. Elsen, V. Lemaitre, K. Müller, H. Rick, H.-C. Schultz-Coulon: *Calculating Event Weights in Case of Downscaling on Trigger Levels 1-4*, `H1-04/97-517` (1997).

[4] D. Bruncko: *Štúdium leptón–nukleónových zrážok*, second edition, SAV Košice (2001).

[5] D. H. Perkins: *Introduction to High Energy Physics*, third edition, Addison–Wesley (1987).

[6] D. Wallny: *A measurement of the Gluon Distribution in the Proton and of the Strong Coupling Constant α_s from Inclusive Deep-Inelastic Scattering*, Ph. D. Thesis, University of Zurich, `DESY-THESIS-2001-058` (2001).

[7] S. Schätzel: *Measurements of Dijet Cross Sections in Diffractive Photoproduction and Deep-Inelastic Scattering at HERA*, Ph. D. Thesis, University of Heidelberg (2004).

[8] S. Schenk: *Energy Flow in Hard Diffractive Deep-Inelastic Scattering and Photoproduction with a Leading Proton*, Diploma thesis, University of Heidelberg (2003).

[9] R. Stamen: *Measurement of Deeply Virtual Compton Scattering at HERA*, Ph. D. Thesis, University of Dortmund, Free University of Brussels (2001).

[10] F.-P. Schilling: *Diffractive Jet Production in Deep-Inelastic e^+p Collisions at HERA*, Ph. D. Thesis, University of Heidelberg (2001).

[11] B. R. Martin, G. Shaw: *Particle Physics*, John Wiley & Sons (1992).

[12] V. Lendermann: *Measurement of the QED Compton Scattering Cross Section with the H1 Detector at HERA*, Ph. D. Thesis, University of Dortmund (2001).

[13] K. Sedlák: *Measurement of Dijet Production at Low Q^2 at HERA*, Ph. D. Thesis, Charles University in Prague (2004).

[14] C. A. G. Canal, R. Sassot: *Deep Inelastic Scattering, Diffraction and all that*, arXiv:hep-ph/9912233 (1999).

[15] J. Bartels, J. R. Forshaw, H. Lotter, M. Wüsthoff: *Diffractive Production of Vector Mesons at Large t*, MC-TH-95/23, ANL-HEP-PR-95-89, DESY-95-253, arXiv:hep-ph/9601201 (1995).

[16] D. Yu. Ivanov, M. Wüsthoff: *Hard diffractive Photon–Proton Scattering at large t*, DTP/98/56, arXiv:hep-ph/9808455 (1998).

[17] N. G. Evanson, J. R. Forshaw: *Diffractive photon production in γp and $\gamma\gamma$ interactions*, CERN-TH/99-51, MC-TH-99/02, arXiv:hep-ph/9902481 (1999).

[18] U. Bassler, G. Bernardi: *On the Kinematic Reconstruction of Deep Inelastic Scattering at HERA: the Σ Method*, DESY 94-231, arXiv:hep-ex/9412004 (1994).

[19] T. C. Nicholls: *A Measurement of the Diffractive Proton Structure Function at HERA*, Ph. D. Thesis, University of Birmingham (1997).

[20] B. E. Cox, J. R. Forshaw: *Diffractive production of high-p_t photons at HERA*, CERN-TH/99-394, MAN/HEP/99/6, MC-TH99/18, arXiv:hep-ph/9912486 (1999).

[21] P. Newman: *A Study of the Dynamics of Diffractive Photoproduction at HERA*, Ph. D. Thesis, University of Birmingham (1996).

[22] C. A. Johnson: *A Measurement of the Diffractive Proton Structure Function $F_2^{D(3)}$ at Low Q^2 at the H1 Experiment at HERA*, Ph. D. Thesis, University of Birmingham (2002).

[23] F. W. Bopp, R. Engel, J. Ranft: *Rapidity Gaps and the* PHOJET *Monte Carlo*, Si 98-25, BA-98-17, arXiv:hep-ph/9803437 (1998).

[24] B. List, A. Mastroberardino: DIFFVM – *A Monte Carlo Generator for Diffractive Processes in ep Scattering*, DESY-PROC-1999-02, pg:396-404, Hamburg (1998).

[25] G. Marchesini, B. R. Webber, G. Abbiendi, I. G. Knowles, M.H. Seymour, L. Stanco: *HERWIG 6.1 Release Note*, Computer Phys. Commun. 67 (1992) 465.

[26] A. Aktas et al. [H1 Collaboration], *Diffractive photoproduction of J/ψ mesons with large momentum transfer at HERA*, Phys. Lett. B **568** (2003) 517.

I wish to thank to all the kind people I've met during my short stay in ULB.

First of all, I thank to Laurent Favart – for every of that many discussions we had, for leading my way, telling me what to do and (more often) what not to do, sharing his knowledge and introducing me to the shadows of the experimental physics,

I thank to Benoit Roland who was always there, smiling and reproducing his deep knowledge of ROOT and H1OO instruction manual,

I thank to Pierre Marage and Daniel Bertrand for allowing me to study at ULB,

I thank to Pascal, Lionel, Seb, Carol, Fred and Chantal, all so kind people.

Thank you Tekla for your patience.

Tomáš